

ANTICANCER ACTIVITY OF MANSONONE G DERIVATIVES AGAINST HUMAN NON-
SMALL CELL LUNG CANCER: COMPUTATIONAL AND MECHANISTIC STUDY



A Dissertation Submitted in Partial Fulfillment of the Requirements
for the Degree of Doctor of Philosophy in Biochemistry and Molecular Biology

Department of Biochemistry

Faculty of Science

Chulalongkorn University

Academic Year 2018

Copyright of Chulalongkorn University

ฤทธิ์ด้านมะเร็งของอนุพันธ์แมนโซโนนิจต่อเซลล์มะเร็งปอดชนิดไม่ใช่เซลล์เล็กของมนุษย์:
การศึกษาทางคอมพิวเตอร์และกลไกการออกฤทธิ์



วิทยานิพนธ์นี้เป็นส่วนหนึ่งของการศึกษาตามหลักสูตรปริญญาวิทยาศาสตรดุษฎีบัณฑิต
สาขาวิชาชีวเคมีและชีววิทยาโมเลกุล ภาควิชาชีวเคมี
คณะวิทยาศาสตร์ จุฬาลงกรณ์มหาวิทยาลัย
ปีการศึกษา 2561
ลิขสิทธิ์ของจุฬาลงกรณ์มหาวิทยาลัย

ภาณุพงศ์ มหาลาภบุตร : ฤทธิ์ต้านมะเร็งของอนุพันธ์แมนโซโนนจีต่อเซลล์มะเร็งปอดชนิด
ไม่ใช่เซลล์เล็กของมนุษย์: การศึกษาทางคอมพิวเตอร์และกลไกการออกฤทธิ์. (

ANTICANCER ACTIVITY OF MANSONONE G DERIVATIVES AGAINST HUMAN
NON-SMALL CELL LUNG CANCER: COMPUTATIONAL AND MECHANISTIC

STUDY) อ.ที่ปรึกษาหลัก : ผศ. ดร.ธัญญา รุ่งโรจน์มงคล, อ.ที่ปรึกษาร่วม : ผศ. ดร.ปิยนุช
วงศ์อนันต์

Epidermal growth factor receptor (EGFR) และ DNA topoisomerase II (Topo II) เป็น เอนไซม์เป้าหมายหลักสำหรับการรักษามะเร็งปอดชนิดไม่ใช่เซลล์เล็ก เนื่องจากเอนไซม์ทั้งสองมีความสำคัญ ในวิถีสัญญาณที่เกี่ยวข้องกับการเจริญของเซลล์มะเร็ง งานวิจัยนี้ได้ศึกษาฤทธิ์ต้านมะเร็งทั้งทางทฤษฎีและ การทดลองของสารแมนโซโนนจี (MG) และอนุพันธ์ ต่อดีถีสัญญาณที่ถูกควบคุมด้วยโปรตีน EGFR และ Topo II ในเซลล์มะเร็งปอดชนิดไม่ใช่เซลล์เล็กของมนุษย์ ทั้งชนิดที่ไม่มีการกลายพันธุ์ของ EGFR (A549) และชนิดที่มีการกลายพันธุ์ของ EGFR (H1975) ผลการคัดกรองค่าความเป็นพิษต่อเซลล์มะเร็งในหลอด ทดลองพบว่า สารบิวทอกซีแมนโซโนนจี (MG3) มีฤทธิ์ต้านมะเร็งต่อเซลล์มะเร็งปอดชนิดที่มีการกลาย พันธ์ (H1975, IC_{50} 4.21 μ M) ได้ดีกว่าชนิดที่ไม่มีการกลายพันธ์ (A549, IC_{50} 8.54 μ M) และสาร MG3 มี ความเป็นพิษที่น้อยต่อเซลล์ปกติ (IC_{50} 21.16 μ M) ผลการทำ western blot และ flow cytometry พบว่า สาร MG3 เหนี่ยวนำให้เซลล์มะเร็งปอดเกิดการตายแบบอะพอพโทซิสที่ถูกควบคุมด้วยเอนไซม์ caspase โดยผ่าน ทางการยับยั้ง (1) phosphorylation ของ STAT3 และ Akt และ (2) ผ่านการกระตุ้น phosphorylation ของ Erk ขณะที่ผลการคำนวณทางเคมีคอมพิวเตอร์ระหว่างสารแมนโซโนนกับ Topo II ATPase domain พบว่า สารอนุพันธ์เอสเทอร์แมนโซโนนจี 14 (MG14) มีความสามารถในการจับกับเอนไซม์ดังกล่าวสูงที่สุด นอกจากนี้สาร MG14 สามารถเหนี่ยวนำให้เกิด closed conformation ของ Topo II ที่กรดอะมิโนเรซิดิวส์ 147-151 นอกจากนี้การเกิดสารประกอบเชิงซ้อนอินคลูชันระหว่างสารแมนโซโนนกับปีตาไซโคลเดททรินซ์ (β CD) โดยเฉพาะอย่างยิ่งอนุพันธ์ชนิด 2,6-dimethyl- β CD สามารถเพิ่มค่าการละลายน้ำ ความเสถียร การ แยกของอีแนนซิโอเมอร์ และฤทธิ์ต้านมะเร็งของสารแมนโซโนน

สาขาวิชา ชีวเคมีและชีววิทยาโมเลกุล

ปีการศึกษา 2561

ลายมือชื่อผู้คิด

ลายมือชื่อ อ.ที่ปรึกษาหลัก

ลายมือชื่อ อ.ที่ปรึกษาร่วม

5772836223 : MAJOR BIOCHEMISTRY AND MOLECULAR BIOLOGY

KEYWORD: Lung cancer, Mansonone G, Apoptosis, Cyclodextrin

Panupong Mahalapbutr : ANTICANCER ACTIVITY OF MANSONONE G DERIVATIVES AGAINST HUMAN NON-SMALL CELL LUNG CANCER: COMPUTATIONAL AND MECHANISTIC STUDY. Advisor: Asst. Prof. Dr. THANYADA RUNGROTMONGKOL Co-advisor: Asst. Prof. Dr. PIYANUCH WONGANAN

Epidermal growth factor receptor (EGFR) and DNA topoisomerase II (Topo II) are the key molecular targets for non-small cell lung cancer (NSCLC) due to its major contribution to complex signaling cascades modulating the survival of cancer cells. In the present study, mansonone G (MG), a naturally occurring quinone-containing compound, and its semi-synthetic ether derivatives were subjected to theoretically and experimentally investigate the anticancer effects on EGFR/Topo II-mediated signaling pathways in NSCLC cell lines expressing wild-type EGFR (A549) and mutant EGFR (H1975). *In vitro* cytotoxicity screening results demonstrated that butoxy MG (MG3) was more susceptible to H1975 mutant cells (IC_{50} of 4.21 μM) than A549 wild-type cells (IC_{50} of 8.54 μM). Importantly, MG3 was low toxic against normal fibroblast cells (IC_{50} of 21.16 μM). Western blotting and flow cytometric analyses revealed that MG3 induced a caspase-dependent apoptosis mechanism through: (i) inhibition of p-STAT3 and p-Akt without affecting upstream p-EGFR and (ii) activation of p-Erk. According to the computational calculations on MGs/Topo II complexes, we found that, among all studied MGs, an ester derivative MG14 exhibited the highest binding affinity toward Topo II ATPase domain. In addition, the binding of MG14 against Topo II induced the residues 147-151 to locate closer to ligand, resulting in a closed conformation. Additionally, the encapsulation of mansonones(s) into the hydrophobic inner cavity of beta-cyclodextrins (β CDs), especially 2,6-dimethyl- β CD derivative, led to the enhancement of solubility, stability, enantioseparation, and anticancer activity of the uncomplexed mansonone(s).

Field of Study:	Biochemistry and Molecular Biology	Student's Signature
Academic Year:	2018	Advisor's Signature
		Co-advisor's Signature

ACKNOWLEDGEMENTS

Firstly, I would like to express my appreciation to my thesis advisor, Asst. Prof. Dr. Thanyada Rungrotmongkol, who always gives the constructive, useful, and motivated suggestions during my Ph.D. study. I would also like to greatly thank my co-advisor, Asst. Prof. Dr. Piyanuch Wonganan, Department of Pharmacology, Faculty of Medicine, Chulalongkorn University, for her mentorship and helpful commentary of this research, especially in the experimental investigations. Additionally, I would like to acknowledge Mr. Noppadol Sa-ard-lam, Department of Immunology, Faculty of Dentistry, Chulalongkorn University, for technical assistance on flow cytometric analysis.

Thanks to all comrades and members in Structural and Computational Biology research Unit, Department of Biochemistry at Chulalongkorn University as well as in Molecular Pharmacology Laboratory, Faculty of Medicine, Chulalongkorn University for their friendship and encouragement.

Finally, I would like to thank the Science Achievement Scholarship of Thailand for Ph.D. scholarship as well as the Thailand Research Fund (grant number RSA5980069) and the 90th Anniversary of Chulalongkorn University (CU) Fund (Ratchadaphiseksomphot Endowment Fund) for financial supports. In addition, the Center of Excellence in Computational Chemistry, Faculty of Science, Chulalongkorn University, is acknowledged for facilities and computing resources.

จุฬาลงกรณ์มหาวิทยาลัย
CHULALONGKORN UNIVERSITY

Panupong Mahalapbutr

TABLE OF CONTENTS

	Page
.....	iii
ABSTRACT (THAI).....	iii
.....	iv
ABSTRACT (ENGLISH)	iv
ACKNOWLEDGEMENTS.....	v
TABLE OF CONTENTS.....	vi
Table.....	xi
Fig.....	xii
LIST OF ABBREVIATIONS.....	1
CHAPTER I	3
INTRODUCTION.....	3
1.1 Research rationality	3
1.2 Background and significance of research problem.....	3
1.3 Objectives	8
1.4 Scope of research.....	8
1.5 Contribution of the study significance	8
CHAPTER II	9
ANTICANCER ACTIVITY AND ITS UNDERLYING MECHANISMS OF MANSONONE G DERIVATIVES AGAINST HUMAN NON-SMALL CELL LUNG CANCER CELL LINES	9
2.1 Abstract.....	10
2.2 Introduction	11

2.3 Results.....	13
2.3.1 <i>In vitro</i> cytotoxicity screening of MG derivatives against NSCLC cell lines.	13
2.3.2 Butoxy mansonone G exhibits a potent cytotoxicity against NSCLC cells ..	15
2.3.3 Butoxy mansonone G induces apoptosis in A549 and H1975 cell lines	17
2.3.4 Butoxy mansonone G inhibits STAT3 and Akt signaling pathways in NSCLC cell lines.....	19
2.3.5 Predictive binding affinity of butoxy mansonone G against STAT3 and Akt signaling proteins.....	21
2.3.6 Key binding residues	22
2.3.7 <i>In silico</i> study on conformational change of STAT3 and Akt upon butoxy mansonone G binding	24
2.4 Discussion.....	26
2.5 Materials and methods	30
2.6 Conclusions.....	34
CHAPTER III	35
SUSCEPTIBILITY OF MANSONONE G DERIVATIVES AGAINST HUMAN DNA TOPOISOMERASE II ALPHA ATPASE DOMAIN.....	35
3.1 Abstract.....	36
3.2 Introduction	36
3.3 Material and methods	39
3.3.1 Preparation of initial structures and molecular docking	39
3.3.2 Selective integrated tempering sampling (SITS) based docking.....	40
3.3.3 Molecular dynamics (MD) simulations.....	42
3.3.4 Free energy calculations based on MM/PBSA and MM/GBSA methods.....	42

4.3.2.7 Cytotoxicity of MG toward lung cancer cells	66
4.3.2.8 Statistical analysis	66
4.4 Results and discussion	67
4.4.1 System stability of simulated models	67
4.4.2 Ligand mobility inside β CD's hydrophobic cavity	68
4.4.3 β CDs conformations upon MG binding	69
4.4.4 Solvent accessibility toward inclusion complexes.....	71
4.4.5 Binding free energy of inclusion complexes.....	73
4.4.6 Phase solubility study and thermodynamic parameters.....	75
4.4.7 Inclusion complex characterization	77
4.4.7.1 Thermal behavior of MG and its inclusion complexes	77
4.4.7.2 Surface morphological changes upon complexation	78
4.4.8 Cytotoxicity of MG/ β CDs inclusion complexes toward lung cancer	80
4.5 Conclusions.....	82
CHAPTER V	83
ENHANCED STABILITY AND ENANTIOSEPARATION OF MANSONONE E AND H/BETA-CYCLODEXTRINS INCLUSION COMPLEXES	83
5.1 Abstract.....	84
5.2 Introduction	84
5.3 Computational details	86
5.4 Results and discussion	88
5.4.1 System stability.....	88
5.4.2 β CDs conformation.....	89

5.4.3 Transformation of <i>cis</i> - to <i>trans</i> -configuration of glucopyranose units	90
5.4.4 Ligand mobility in β CDs cavities	92
5.4.5 Water accessibility toward inclusion complexes	94
5.4.6 Binding free energy of inclusion complexes.....	97
5.5 Conclusions.....	100
CHAPTER VI	102
CONCLUSIONS.....	102
REFERENCES.....	104
APPENDIX	128
VITA	141

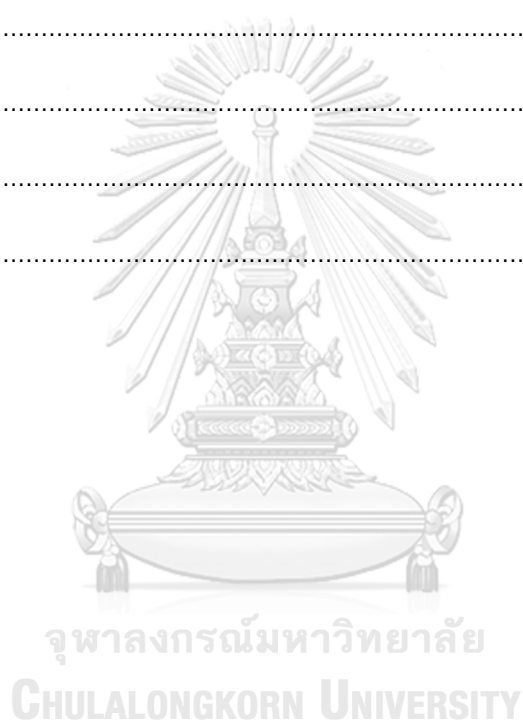


Table.

	Page
Table 1 In vitro cytotoxicity screening of all MG analogs against A549 and H1975 NSCLC cell lines. Cells were treated with indicated compounds at 10 μM and 100 μM for 48 h, and cell viability was determined using MTT assay. Data are expressed as mean \pm SEM of two independent experiments. MG derivatives exhibiting a percentage of cell viability at 10 μM ($\%CV_{10\ \mu\text{M}}$) <50 were defined as potent compounds.....	14
Table 2 The MM/GBSA ΔG_{bind} and its energy components (kcal/mol). The $\Delta G_{\text{bind, exp}}$ was calculated using the equation of $\Delta G_{\text{bind, exp}} = RT \ln IC_{50}$, where R is the gas constant (1.985×10^{-3} kcal/mol/K), T is the experimental temperature (K), and IC_{50} is the half maximal inhibitory concentration (μM).	22
Table 3 The averaged $\Delta G_{\text{bind, MM/GBSA}}$ and its energy components (kcal/mol) of MG/ β CDs inclusion complexes. Data are expressed as mean \pm SEM from three independent MD simulations. ΔE_{MM} , molecular mechanics energy; ΔG_{solv} , solvation free energy comprising polar ($\Delta G_{\text{solv, polar}}$) and non-polar ($\Delta G_{\text{solv, non-polar}}$) terms; ΔS , entropy. * $p \leq 0.05$, ** $p \leq 0.01$, and *** $p \leq 0.001$ vs. MG/ β CD.....	74
Table 4 Kc of MG/ β CDs inclusion complexes at different temperatures.	76
Table 5 Thermodynamic values for the inclusion complex formation of MG with β CDs derived from Van't Hoff plots (using R of $1.985 \text{ cal mol}^{-1} \text{ K}^{-1}$ and T of 303K) in comparison to the ΔG_{bind} obtained from MM/GBSA method.	77
Table 6 Integration number, n(r), up to the first minimum derived from Figure 7 around the focused oxygen atoms of mansonones.	97

Fig.

Page

Figure 1 Pie charts present the distribution of new cases and deaths for the 10 most common cancers for both sexes in 2018 [1]. 4

Figure 2 Signaling pathways involving cross talk(s) of EGFR and Topo II α [12]. 5

Figure 3 Two-dimensional (2D) chemical structures of MG and its semi-synthetic ether derivatives MG1-MG10 [24]. 6

Figure 4 Two-dimensional (2D) and three-dimensional (3D) structures of β CDs. 7

Figure 5 2D chemical structures of (A) MG and its semi-synthetic ether derivatives MG1-MG10 [24] and (B) the known STAT3 (cryptotanshinone (CST) and S3I201) and Akt (uprosertib and H8) inhibitors. Three-dimensional (3D) structures of (C) STAT3 and (D) Akt1 signaling proteins. The SH2 domain of STAT3 and the ATP-binding pocket of Akt are shown by blue surface and black circle, respectively. 13

Figure 6 Cell viability of NSCLC (A-C) and PCS201-010 (D-F) cell lines after treatment with MG3, MG4, and CDDP for 48 h. The IC₅₀ (μ M) and SI of three focused compounds against all studied cell lines are shown in (G) and (H), respectively. (I) The morphological changes of two NSCLC cell lines treated with MG3 at various concentrations for 48 h. 16

Figure 7 Flow cytometric analysis of Annexin V/PI stained cells after MG3 and CDDP treatments for 24 h on (A) A549 and (B) H1975 cells. Western blot analysis of apoptotic markers, caspase-3 and PARP, for (C) A549 and (D) H1975 cells. Inhibition of MG3-induced apoptosis by the pan caspase inhibitor Z-VAD(OMe)-FMK in (E) A549 and (F) H1975 cells. Data are expressed as mean \pm SEM (n = 3). *p \leq 0.05, **p \leq 0.01, and ***p \leq 0.001 vs. control. @p \leq 0.05, @@p \leq 0.01, and @@@p \leq 0.001 vs. MG3. #p \leq 0.05, ##p \leq 0.01, and ###p \leq 0.001 vs. CDDP. 18

Figure 8 MG3 dose-dependently inhibits the phosphorylation of STAT3 (Tyr705) and Akt (Ser473) in (A) A549 and (B) H1975 cells at 24 h. The expression of p-Erk (Thr202/Tyr204) is found to be increased upon MG3 and CDDP treatments. The phosphorylation of EGFR (Y1068) for both (C) A549 and (D) H1975 cells is not significantly affected by MG3 and CDDP treatments. (E) Proposed mechanisms of MG3 against two studied NSCLC cell lines, in which MG3 promotes cell apoptosis through the inhibition of p-Akt and p-STAT3 as well as through the activation of MAPK signaling pathway. Data are expressed as mean \pm SEM of three independent experiments. * $p \leq 0.05$, ** $p \leq 0.01$, and *** $p \leq 0.001$ vs. control. 20

Figure 9 ΔG_{bind} residue (kcal/mol) of (A) STAT3 and (B) Akt. The amino acids involved in ligand binding are shaded according to their ΔG_{bind} residue, in which the highest and lowest energies are ranged from red to magenta, respectively. 24

Figure 10 Porcupine plot of apo and holo forms of (A) STAT3 and (B) Akt across the PC1. The residues within 5 Å of ligand are presented in circle where the MG3 molecule is shown in vdW model. The PCA scree plot of quantitative characters for each protein is given below, in which the columns in black and grey represent the data for apo and holo forms, respectively. 25

Figure 11 (A) The 3D structure of DNA topoisomerase II α , in which the ATPase and the cleavage/religation domains are shaded by green and dark blue colors. The ATP-binding pocket, etoposide pocket, and central domain are represented by light green, orange, and blue circles, respectively. The close-up regions for (B) ATP-binding pocket, (C) etoposide pocket, and (D) central domain. 39

Figure 12 Chemical structures of (A) MG and its synthesized derivatives, which are ether derivatives (left panel) and ester derivatives (right panel), (B) 1,4-BQ, (C) salvicine, (D) etoposide, and (E) merbarone. 44

Figure 13 (A) CDOCKER and (B) SITS-based docking interaction energies (kcal/mol) of the etoposide, merbarone, salvicine, 1,4-BQ, and MG analogs binding at the three different domains of Topo II α 45

Figure 14 RMSD plot for complex (black), backbone (grey), and ligand (light grey) of the 10 simulated complexes.	46
Figure 15 Per-residue decomposition free energy ($\Delta G_{\text{bind, residue}}$) of the ATPase domain of Topo II α for the binding of the two reference compounds (salvicine and 1,4-BQ) and eight selected MG analogs.	49
Figure 16 The binding orientation of (A) salvicine, (B) 1,4-BQ, (C) MG4, (D) MG5, (E) MG6, (F) MG12, (G) MG13, (H) MG14, (I) MG15, and (J) MG17 inside ATP-binding pocket drawn from the last MD snapshot. The amino acids involved in ligand binding are shaded according to the per-residue decomposition free energy ($\Delta G_{\text{bind, residue}}$ (kcal/mol)) in Fig. 5, in which the highest and lowest energies are ranged from dark brown to magenta, respectively.	50
Figure 17 The percentage of H-bond occupation of the amino acid residues within ATP-binding pocket contributing to all ligands during the last 10 ns simulation.	52
Figure 18 (A) The two chains of Topo II α ATPase domain, in which chain A and chain B are shaded by green and red colors, respectively. (B) The amino acids within a 5-Å sphere around ligands used for SASA calculations where the results are plotted in (C).	53
Figure 19 (A) The molecular mechanical energy in gas phase in terms of electrostatic and vdW interactions (ΔE_{elec} and (ΔE_{vdW}) and (B) MM/PB(GB)SA binding free energy, while the asterisk symbol indicates the $\Delta G_{\text{bind, experiment}}$ of 1,4-BQ (-7.18 kcal/mol) calculated by the equation of $\Delta G_{\text{bind, experiment}} = RT \ln IC_{50}$, where R is the gas constant (8.31451 Jmol ⁻¹ K ⁻¹), T is the experimental temperature (310K), and IC ₅₀ is the half maximal inhibitory concentration for ATPase activity (8.58 ± 0.8 μM) [136].	55
Figure 20 (A) The timeline secondary structures of MG14 system, (B) 3D representation of MG14-Topo II α complex shaded by secondary structure color using VMD program where the ATP-binding pocket is shown in black box. B1 and B2 represents the ATP-binding pocket of chain A and chain B, respectively. The secondary structure plot is represented by six colors for turn (T: cyan), extended configuration (E: yellow), isolated	

bridge (B: olive green), alpha helix (H: pink), 3-10 helix (G: dark blue), and pi-helix (I: red).	57
Figure 21 (A) Porcupine plot of MG14/Topo II α complex showing the significant motion, especially turn region (residues 145-151) across the first PC in the holo form (left panel) and apo form (right panel), in which head of the arrow indicates the direction of motion, while its length indicates the amplitude of motion. (B) The 2D projection of MD trajectories on the first two PCs. (C) PCA scree plot of quantitative characters.....	58
Figure 22 (A) 2D structure of MG. (B) 2D- and 3D structures of β CD, where the functional substitutions used in this study are shown below.....	63
Figure 23 RMSD plot of all investigated inclusion complexes for the three independent MD simulations.	67
Figure 24 (A) The distance between C_m (A/Q-ring) of MG and C_m of β CD of all studied inclusion complexes for the three MD independent simulations. (B) The binding orientation of MG inside β CD (blue), DM β CD (green), and 2HP β CD (violet) cavities drawn from the last MD snapshot.	69
Figure 25 (A) The distance parameters (dO_{3-2} and dO_{4-4}) used for PES calculations (left) as well as the obtained results (right). (B) The representative native contact PDB structures shown in line mode (top) and the number of contacts between MG and glucose units of β CDs (bottom). Data are expressed as mean \pm SEM of three independent MD simulations.	71
Figure 26 (A) SASA of MG/ β CD, MG/DM β CD, and MG/DHP β CD for three different MD runs. (B) The averaged SASA in the last 20-ns MD simulations for each inclusion complex. Data are expressed as mean \pm SEM (n=3). * $p \leq 0.05$, ** $p \leq 0.01$, and *** $p \leq 0.001$	73
Figure 27 Phase solubility diagram of MG with all studied β CDs in water at 30, 37, and 45 $^{\circ}$ C.	76

Figure 28 DSC thermogram of MG, β CD, DM β CD, and the freeze-dried inclusion complexes MG/ β CD and MG/DM β CD.	78
Figure 29 SEM images of (A) MG, (B) β CD, (C) DM β CD, (D) MG/ β CD, and (E) MG/DM β CD at 300 times magnification.....	79
Figure 30 (A) Cell viability of MG, MG/ β CD, and MG/DM β CD against A549 human lung cell line. (B) The IC ₅₀ of all investigated compounds. (C) Cell viability of the free form of β CD and DM β CD. Data are expressed as mean \pm SEM of three independent experiments. *p \leq 0.05, **p \leq 0.01, and ***p \leq 0.001 vs. MG.	81
Figure 31 Chemical structures of (A) ME, (B) MH; A, B, and C represent aromatic, quinone, and oxane rings, respectively; C3-position presents the chiral center. (C) Survey of the β CD derivatives used in this study and the 3D structure of β CD.....	86
Figure 32 RMSD plots for all atoms of the two stereoisomers of ME and MH inclusion complexes.	89
Figure 33 The potential energy surface (PES) spanned by the distance between the adjacent glycosidic oxygens, O4 _(n) - O4 _(n+1) and the distance between the secondary hydroxyl groups on the wider rim, O3 _(n) - O2 _(n+1) of β CDs in complex with ME and MH..	90
Figure 34 (A) The structural parameter of angle θ [C6 _(n) - C2 _(n+1) - C6 _(n+1)], (B) The examples of flipped conformations of 2,6-DM β CD with different numbers of flipped glucopyranose units.	92
Figure 35 The averaged percentage of flip conformations of β CDs in ligand bound form using the structural parameter of angle θ [C6 _(n) - C2 _(n+1) - C6 _(n+1)]. Note that the standard deviation (SD) was calculated from three independent simulations.	92
Figure 36 Distance between the center of gravity (Cg) of each ring of ligand and CD (d [Cg _{ringA/B/C} - Cg _{CD}]). Light grey box represents the height of torus of β CD without the functional modification.	94

Figure 37 Radial distribution function (RDF) of water oxygen atoms around the focused oxygen atoms of mansonone molecules in different β CDs.	96
Figure 38 (A) Molecular mechanics energy components in gas phase and (B) the MM-PBSA binding free energy (ΔG_{bind}) for all simulated systems.	99
Figure 39 Binding orientations of (S)-ME inside all β CDs taken from the last MD snapshot.	100



LIST OF ABBREVIATIONS

AMBER	=	Assisted model building with energy refinement
ANOVA	=	Analysis of variance
ATCC	=	American Type Culture Collection
CASPASE	=	Cysteine aspartic specific protease
CG	=	Conjugated gradient
CO ₂	=	Carbon dioxide
DMEM	=	Dulbeco's Modified Eagle Medium
DMSO	=	Dimethyl sulfoxide
ERK	=	Extracellular signal-regulated kinase
FITC	=	Fluorescein isothiocyanate
GAFF	=	General AMBER force field
GAPDH	=	Glyceraldehyde-3-phosphate dehydrogenase
GBSA	=	Generalized Born surface area
H	=	Hour
HEPES	=	4-(2-hydroxyethyl-1-piperazineethanesulfonic acid)
HF	=	Hatree-Fock
IC ₅₀	=	Half maximal inhibitory concentration
MAPK	=	Mitogen-activated protein kinase
MD	=	Molecular dynamics
MM	=	Molecular mechanics

MTT	=	3-(4, 5-dimethylthiazol-2-yl)-2, 5-diphenyltetrazolium bromide
PARP	=	Poly (ADP-ribose) polymerase
PBS	=	Phosphate buffer saline
PBSA	=	Poisson-Boltzmann surface area
PDB	=	Protein Data Bank
PI	=	Propidium iodide
PME	=	Particle mesh Ewald
RESP	=	Restrained electrostatic potential
RMSD	=	Root mean square displacement
RPM	=	Round per minutes
SASA	=	Solvent accessible surface area
SD	=	Steepest descents
vdW	=	van der Waals
X-ray	=	Crystallographic spectroscopy

CHAPTER I

INTRODUCTION

1.1 Research rationality

Targeting epidermal growth factor receptor (EGFR)/DNA topoisomerase II α (Topo II α)-mediated signaling pathways has been proved as a potential strategy for lung cancer treatment. Even though the use of chemotherapeutic and targeted drugs has shown to significantly prolong the progression free survival of lung cancer patients, the acquired drug resistances inevitably develop after 1-year treatment. In this study, the combination of experimental techniques and molecular modeling was applied to investigate the anticancer activity and its underlying mechanisms of mansonone G (MG) derivatives toward lung cancer cells. Moreover, the beta-cyclodextrin (β CD) inclusion complexation was used to increase the solubility, stability, and anticancer potential of MG compound.

1.2 Background and significance of research problem

Lung cancer is the first leading cause of cancer-related death globally for both men and women (Fig. 1) [1]. In Thailand, lung cancer is ranked in top five diagnosed cancers, showing 63.1% of mortality, 59.2% of incidence, and 54.3% of five-year limited duration prevalence [2]. More than 85% of all diagnosed lung cancer cases are currently classified as non-small cell lung cancer (NSCLC), for which the 5-year survival rate is only 17.8% [3].

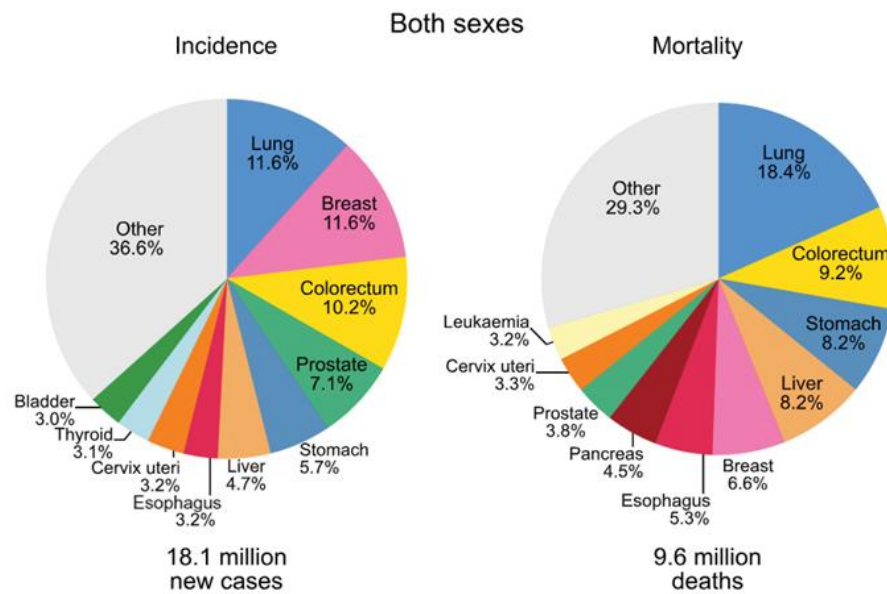


Figure 1 Pie charts present the distribution of new cases and deaths for the 10 most common cancers for both sexes in 2018 [1].

Overexpression of EGFR and Topo II α enzymes has been characterized as oncogenic drivers for NSCLC development [4-8]. Therefore, these two proteins are considered as some of the attractive targets for NSCLC treatment. The activation of EGFR leads to the stimulation of a vast array of downstream signaling cascades responsible for cell growth and proliferation [4, 9], including (i) mitogen-activated protein kinase (MAPK), (ii) phosphoinositide 3-kinase (PI3K)/protein kinase B (Akt), (iii) signal transducer and activator of transcription (STAT), and (iv) the expression of human Topo II α (Fig. 2), which is a nuclear enzyme that plays a key role in a number of growth-related processes such as replication, transcription, recombination, and mitosis [10, 11].

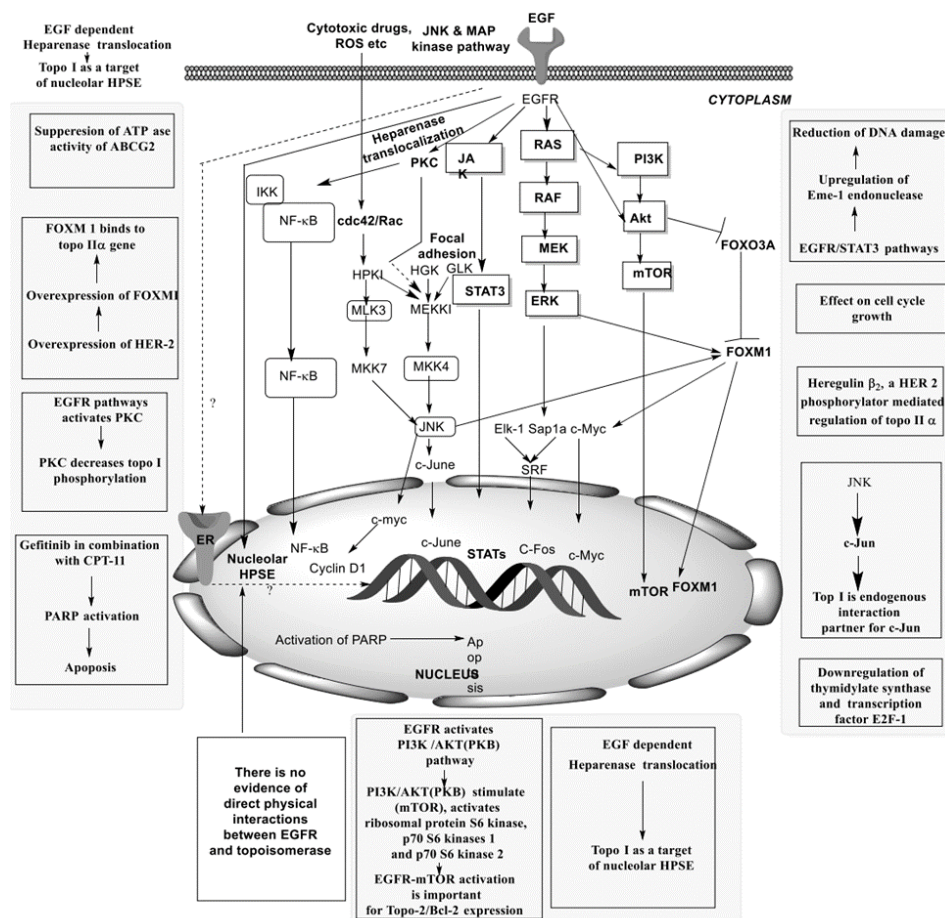


Figure 2 Signaling pathways involving cross talk(s) of EGFR and Topo II α [12].

Cisplatin (CDDP) is an alkylating agent that covalently interacts with guanine bases of DNA molecules to form intra- and inter strand crosslinks, leading to apoptotic induction. Although CDDP has been the first-line chemotherapeutic drug for patients with advanced (stage IIIb/IV) NSCLC [13-16], its efficacy is often limited by acquired drug resistances [17-20] as well as several side effects [21]. First generation tyrosine kinase inhibitors (TKIs), e.g., erlotinib and gefitinib, are approved for exon 19 deletion and exon 21 L858 substitution mutation of EGFR. However, the acquired drug resistance against TKIs caused by secondary point mutation T790M in exon 20 of EGFR was developed inevitably after a median response duration of 9 to 13 months [22, 23]. The replacement of threonine to methionine causes the steric hindrance inside ATP-binding pocket and alters the conformation of TK domain, resulting in increasing its affinity for ATP substrate and consequently preventing the binding of TKIs. Given that

NSCLC cells rapidly acquire resistance to both CDDP and TKIs; thus, there is an urgent need to search for a novel compound that can potentially overcome such problems by (i) targeting the alternative intracellular survival signaling pathways in NSCLC and (ii) remaining effective in both NSCLC cells expressing wild-type and T790M-positive EGFRs.

MG is the main bioactive constituent isolated from the heartwood of *Mansonia gagei* [24]. Many lines of evidence have shown that MG exerts the potent antiproliferative effects on various types of solid tumors such as ovarian (A278, IC₅₀ of 10.2 μM), colorectal (HCT116, IC₅₀ of 63.4 μM), cervical (HeLa, IC₅₀ of 18.8 μM), liver (Huh-7, IC₅₀ of 25.9 μM and HepG2, IC₅₀ of 36.3 μM), and breast (MCF-7, IC₅₀ of 23.0 μM) cancer cell lines [25-27]. Recently, structural modifications of MG (Fig. 3) have been reported to potentially possess antibacterial activity as well as to suppress adipocyte differentiation and lipid accumulation greater than natural MG [24, 28]. However, the anticancer effects of MG and its synthesized derivatives on NSCLC cells, especially the mechanisms of inhibition of MGs against EGFR-mediated signaling pathways and Topo IIα enzyme have never been reported.

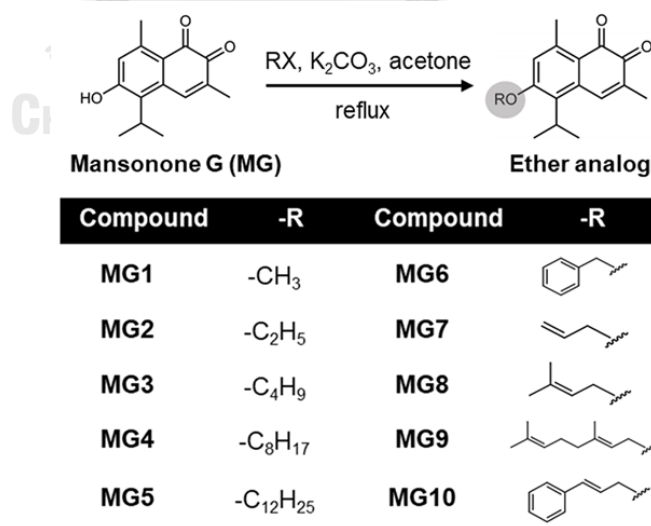


Figure 3 Two-dimensional (2D) chemical structures of MG and its semi-synthetic ether derivatives MG1-MG10 [24].

Even though MG serves as a promising anticancer agent, its poor water solubility (0.007 mM at 30°C) leads to a limited usage for pharmaceutical and medicinal purposes. β CD (Fig. 4) is a cyclic oligosaccharide consisting of seven D-(+)-glucopyranose units linked by α -(1,4) glycosidic linkage. Geometrically, the outer surface of β CD is hydrophilic whilst the inner cavity is rather hydrophobic; thus, β CD can encapsulate various lipophilic guest molecules into its hydrophobic inner cavity, resulting in an enhancement of solubility, stability, dissolution rate, and bioavailability [29-31]. Moreover, β CD can be used as a chiral selector for racemic mixtures in both the pharmaceutical and chemical industries [32-35]. The practical applications of β CD, however, are still limited by its low water solubility (18.5 mg/mL at 25 °C) and nephrotoxicity [36]. β CD derivatives such as 2,6-dimethyl- β CD (2,6-DM β CD), randomly methylated- β CD (RM β CD), and hydroxypropyl- β CD (HP β CD) exhibit a greater water solubility and lower toxicity [31, 36] than those of the parent β CD. Several studies have shown that the water solubility, stability, and biological activities of poorly soluble compounds are significantly increased by complexation with β CD derivatives [37-41].

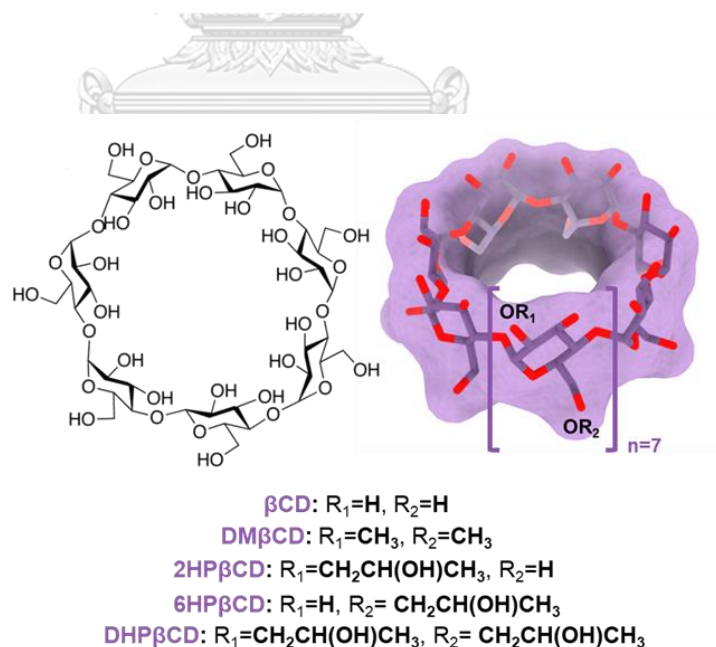


Figure 4 Two-dimensional (2D) and three-dimensional (3D) structures of β CDs.

1.3 Objectives

To search for the most cytotoxic MG analog with low toxicity against human NSCLC cell lines expressing wild-type EGFR (A549) and mutant EGFR (H1975)

To experimentally and theoretically elucidate the molecular mechanisms underlying anticancer activity of the most cytotoxic MG derivative on human NSCLC cell lines

To investigate the water solubility, stability, and anticancer activity of MG/ β CD(s) inclusion complexes

To study the effect of enantioselectivity of β CDs on mansonone(s) binding

1.4 Scope of research

1. Anticancer activity and its underlying mechanisms of MG derivatives against human NSCLC cell lines
2. Susceptibility of MG derivatives against human Topo II α ATPase domain
3. Enhanced solubility, stability, and anticancer activity of MG/ β CDs inclusion complexes
4. Enhanced stability and enantioseparation of mansonone E and H/ β CDs inclusion complexes

1.5 Contribution of the study significance

The results from this study shed light on the anticancer activity and its underlying mechanisms of the MG derivatives, especially MG3 and MG14, which may be useful to develop these compounds as novel anticancer agents. In addition, the information on mansonone(s)/ β CD(s) inclusion complexes can be used for further pharmaceutical and medicinal applications.

CHAPTER II

ANTICANCER ACTIVITY AND ITS UNDERLYING MECHANISMS OF MANSONONE G
DERIVATIVES AGAINST HUMAN NON-SMALL CELL LUNG CANCER CELL LINES

Butoxy mansonone G inhibits STAT3 and Akt signaling pathways in non-small cell lung
cancers: Combined experimental and theoretical investigations

Panupong Mahalapbutr^a, Piyanuch Wonganan^{b,*}, Warinthorn Chavasiri^c and Thanyada
Rungrotmongkol^{a,d,*}

^aStructural and Computational Biology Research Unit, Department of Biochemistry, Faculty of
Science, Chulalongkorn University, Bangkok 10330, Thailand

^bDepartment of Pharmacology, Faculty of Medicine, Chulalongkorn University, 1873 Rama IV Road,
Pathumwan, Bangkok 10330, Thailand

^cCenter of Excellence in Natural Products Chemistry, Department of Chemistry, Faculty of Science,
Chulalongkorn University, Bangkok 10330, Thailand

^dPh.D. Program in Bioinformatics and Computational Biology, Faculty of Science, Chulalongkorn
University, Bangkok 10330, Thailand

*Correspondence: piyanuch.w@chula.ac.th; Fax: +66 2 256-4481 (P.W.); Tel: +66 2 256-4481
(P.W.); thanyada.r@chula.ac.th; Fax: +66 2 218-5418 (T.R.); Tel: +66 2 218-5426 (T.R.)

This article has been published in *Cancers* (2019)

2.1 Abstract

Epidermal growth factor receptor (EGFR) is the key molecular target for non-small cell lung cancer (NSCLC) due to its major contribution to complex signaling cascades modulating the survival of cancer cells. Targeting EGFR-mediated signaling pathways has been proved as a potential strategy for NSCLC treatment. In the present study, mansonone G (MG), a naturally occurring quinone-containing compound, and its semi-synthetic ether derivatives were subjected to investigate the anticancer effects on human NSCLC cell lines expressing wild-type EGFR (A549) and mutant EGFR (H1975). *In vitro* cytotoxicity screening results demonstrated that butoxy MG (MG3) exhibits the potent cytotoxic effect on both A549 (IC₅₀ of 8.54 μM) and H1975 (IC₅₀ of 4.21 μM) NSCLC cell lines with low toxicity against PCS201-010 normal fibroblast cells (IC₅₀ of 21.16 μM). Western blotting and flow cytometric analyses revealed that MG3 induces a caspase-dependent apoptosis mechanism through: (i) inhibition of p-STAT3 and p-Akt without affecting upstream p-EGFR and (ii) activation of p-Erk. The 500-ns molecular dynamics simulations and the molecular mechanics combined with generalized Born surface area (MM/GBSA)-based binding free energy calculations suggested that MG3 could possibly interact with STAT3 SH2 domain and ATP-binding pocket of Akt. According to principal component analysis, the binding of MG3 toward STAT3 and Akt dramatically altered the conformation of proteins, especially the residues in the active site, stabilizing MG3 mainly through van der Waals interactions.

2.2 Introduction

Lung cancer is the first leading cause of cancer-related mortality worldwide [42-44]. Approximately 85% of diagnosed lung cancer cases are classified as non-small cell lung cancer (NSCLC), for which the 5-year survival rate is only 17.8% [3]. The genetic alterations of epidermal growth factor receptor (EGFR) such as overexpression, exon 19 deletion, and exon 21 L858R substitution have been characterized as oncogenic drivers for NSCLC development [6-8]. EGFR (also known as HER1 or ErbB1), a receptor tyrosine kinase, is commonly overexpressed in several types of cancer, including lung carcinoma [4]. The activation of EGFR-mediated signaling pathways is triggered by the binding of growth factors, including EGF and transforming growth factor alpha (TGF α), to the extracellular portion of EGFR, which subsequently induces receptor dimerization and cross-phosphorylation of specific tyrosine residues located on the cytoplasmic tyrosine kinase (TK) domain. These structural modifications result in stimulating a vast array of downstream signaling cascades, e.g., mitogen-activated protein kinase (MAPK), phosphoinositide 3-kinase (PI3K)/Akt, and signal transducer and activator of transcription (STAT) pathways, leading to cell growth, proliferation, migration, and apoptosis evasion [4, 9].

Cisplatin (CDDP), a platinum-based chemotherapeutic drug, has been commonly used to treat a wide range of solid malignancies, including lung cancer [16, 45]. CDDP is the standard regimen in the first-line chemotherapy for patients with advanced stage NSCLC [13-16], especially patients carrying wild-type EGFR [46, 47]. After cellular uptake, CDDP becomes a positively charged aquo complex that can interact with deoxyribonucleic acid (DNA) to form intra- and inter-strand cross-links, resulting in apoptosis induction [16, 48]. However, the efficacy of CDDP-based chemotherapy is limited by numerous severe side effects [21], as well as acquired drug resistance [17-20].

The first-generation tyrosine kinase inhibitors (TKIs, e.g., erlotinib and gefitinib) have shown to significantly prolong the progression-free survival of NSCLC patients harboring EGFR mutations, primarily exon 19 deletion and exon 21 L858R substitution

mutations [49, 50]. TKIs compete with adenosine triphosphate (ATP) at the ATP-binding site of the receptor, inhibiting EGFR-mediated signal transduction [51]. However, acquired resistance caused by the secondary mutation T790M develops inevitably after a median response duration of 9 to 13 months [52-54]. The replacement of threonine (T) to methionine (M) causes a steric hindrance inside ATP-binding pocket and alters the conformation of TK domain, resulting in increasing its affinity for ATP substrate while decreasing the binding affinity for TKIs [54, 55]. Given that NSCLC cells rapidly acquire resistance to both CDDP and TKIs; thus, there is an urgent need to search for a novel compound that can potentially overcome such problems by targeting alternative intracellular survival signaling pathways in NSCLC.

Mansonone G (MG, Fig. 5A), a 1,2-naphthoquinone-containing compound, is the major product isolated from the heartwood extract of *Mansonia gagei* Drumm. from the Sterculiaceae family [24]. MG demonstrates various biological activities, including antitumor [27], antibacterial [56], antiestrogenic [57], anticholinesterase [58], and antifungal activities [56]. Recently, semi-synthetic ether derivatives of MG (Figure 1A) have been shown to exhibit higher antibacterial activity against *Staphylococcus aureus* [24] and inhibit adipocyte differentiation and lipid accumulation [28] more than the MG parent compound. Although several pharmacological effects of MGs have been reported, the anticancer activity of MG and its derivatives against human NSCLC remains largely unknown. Therefore, in the present study, we aimed to search for the most potent cytotoxic MG analog against human NSCLC cell lines expressing wild-type EGFR (A549) and L858R/T790M EGFR (H1975). Moreover, the mechanisms underlying cell death were experimentally and theoretically investigated.

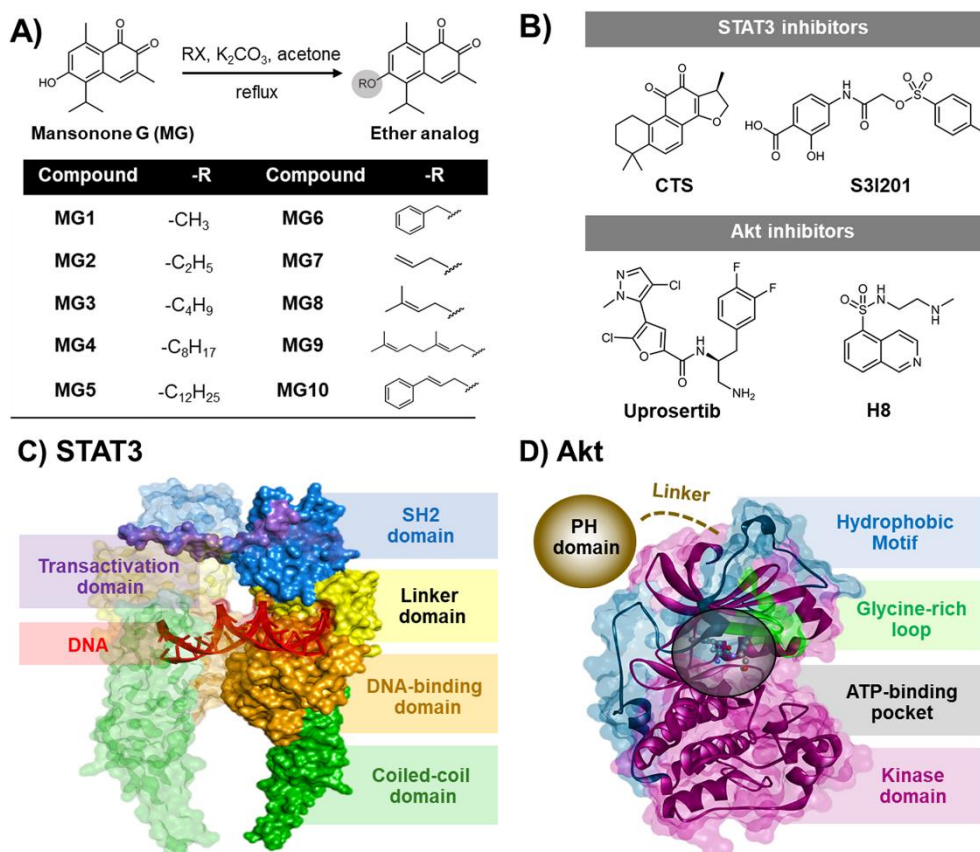


Figure 5 2D chemical structures of (A) MG and its semi-synthetic ether derivatives MG1-MG10 [24] and (B) the known STAT3 (cryptotanshinone (CST) and S31201) and Akt (uprosertib and H8) inhibitors. Three-dimensional (3D) structures of (C) STAT3 and (D) Akt1 signaling proteins. The SH2 domain of STAT3 and the ATP-binding pocket of Akt are shown by blue surface and black circle, respectively.

2.3 Results

2.3.1 *In vitro* cytotoxicity screening of MG derivatives against NSCLC cell lines

Initially, we screened for the most potent cytotoxic MG analogs against NSCLC cell lines expressing wild-type EGFR (A549) and L858R/T790M EGFR (H1975) using the 3-(4,5-dimethylthiazol-2-yl)-2,5-diphenyltetrazolium bromide (MTT) assay. MG derivatives displaying a percentage of cell viability at 10 μM ($\%CV_{10 \mu\text{M}}$) <50 were defined as potent compounds.

As shown in Table 1, MG4 exhibited the most potent cytotoxicity against A549 cells ($\%CV_{10 \mu\text{M}}$ was 7.93 ± 0.43) followed by MG3 ($\%CV_{10 \mu\text{M}}$ was 46.90 ± 1.21),

indicating that these two ether analogs were the most potent compounds toward wild-type cells. In the H1975 mutant cell line, all semi-synthesized MGs (except MG9) exhibited high cytotoxic activity with %CV_{10 μM} of <50, indicating that T790M-positive NSCLC cell line was more susceptible to MG derivatives than A549 cells. Remarkably, MG3 and MG4, exhibiting strong cytotoxicity toward A549 cells, also showed great cytotoxic effects on H1975 cells with the %CV_{10 μM} of 17.04 ± 1.42 and 23.52 ± 1.44, respectively.

Taken together, ether analogs of MG were more cytotoxic to H1975 cells than A549 cells. The two semi-synthetic ether analogs MG3 and MG4, which exhibited high cytotoxicity toward both NSCLC cell lines, were selected for further studies.

Table 1 *In vitro* cytotoxicity screening of all MG analogs against A549 and H1975 NSCLC cell lines. Cells were treated with indicated compounds at 10 μM and 100 μM for 48 h, and cell viability was determined using MTT assay. Data are expressed as mean ± SEM of two independent experiments. MG derivatives exhibiting a percentage of cell viability at 10 μM (%CV_{10 μM}) <50 were defined as potent compounds.

MG analogs	A549		H1975	
	%CV _{10 μM}	%CV _{100 μM}	%CV _{10 μM}	%CV _{100 μM}
MG	95.31 ± 2.35	10.71 ± 0.95	77.28 ± 5.80	8.26 ± 0.79
MG1	70.55 ± 0.27	9.59 ± 1.48	40.46 ± 2.83	7.04 ± 0.22
MG2	63.57 ± 0.91	8.51 ± 0.66	28.33 ± 0.82	7.29 ± 0.57
MG3	46.90 ± 1.21	8.94 ± 0.67	17.04 ± 1.42	6.50 ± 0.28
MG4	7.93 ± 0.43	7.10 ± 0.22 ^a	23.52 ± 1.44	7.42 ± 0.55 ^a
MG5	121.54 ± 0.36	12.12 ± 1.71	44.35 ± 2.98	7.79 ± 0.12
MG6	79.56 ± 4.53	12.54 ± 1.33	20.64 ± 1.17	6.73 ± 0.15
MG7	71.84 ± 1.15	7.45 ± 0.04	27.53 ± 1.54	6.57 ± 0.25

MG8	66.59 ± 5.98	7.93 ± 0.06	20.24 ± 0.92	8.25 ± 0.32
MG9	110.92 ± 1.72	72.86 ± 3.75	89.84 ± 2.39	29.50 ± 2.80
MG10	51.00 ± 0.99	8.74 ± 0.30 ^a	27.85 ± 2.35	23.19 ± 1.38 ^a

^aThe %CV was determined at 50 μ M due to the low solubility of compound.

2.3.2 Butoxy mansonone G exhibits a potent cytotoxicity against NSCLC cells

The half maximal inhibitory concentration (IC_{50}) of the two focused MG analogs, MG3 and MG4, and CDDP, the most commonly used chemotherapeutic agent for NSCLC patients, were evaluated using MTT assays on two NSCLC cell lines A549 and H1975. As shown in Fig. 6A-C, all three tested compounds decreased the viability of both A549 and H1975 cells in a concentration-dependent manner. The IC_{50} of CDDP against two NSCLC cells obtained from this study correlated well with the previous reports [45, 59]. Notably, the two selected MG derivatives were more toxic than CDDP toward cancer cells, as evidenced by the lower IC_{50} of (i) ~4-fold and ~9-fold toward A549 cells and (ii) ~8-fold and ~11-fold against H1975 cells for MG3 and MG4, respectively (Fig. 6G).

We further evaluated the toxicity of our focused MGs toward PCS201-010 normal skin fibroblast cell line (Fig. 6D-F). The obtained IC_{50} results indicated that MG4 and CDDP were toxic to normal cells, as clearly shown by a similarity of IC_{50} between cancer and normal fibroblast cells (selectivity index (SI) of ~1, Fig. 6H). Intriguingly, MG3 was relatively safe to normal cells, in which the IC_{50} observed in PCS202-010 cells was higher than those of A549 (SI of 2.48) and H1975 (SI of 5.03). Since MG3, possessing potent cytotoxicity against cancer cells, was less toxic to normal cells than MG4, we then elucidated the mechanisms underlying MG3-induced cell death in NSCLC cell lines experimentally and theoretically.

According to the morphological alteration of A549 and H1975 NSCLC cells upon MG3 treatment for 48 h (Fig. 6I), it can be clearly seen that MG3 dose-dependently induced cellular shrinking, a predominant characteristic of programmed cell death [60], suggesting that MG3 promoted cell death through an apoptosis-inducing effect.

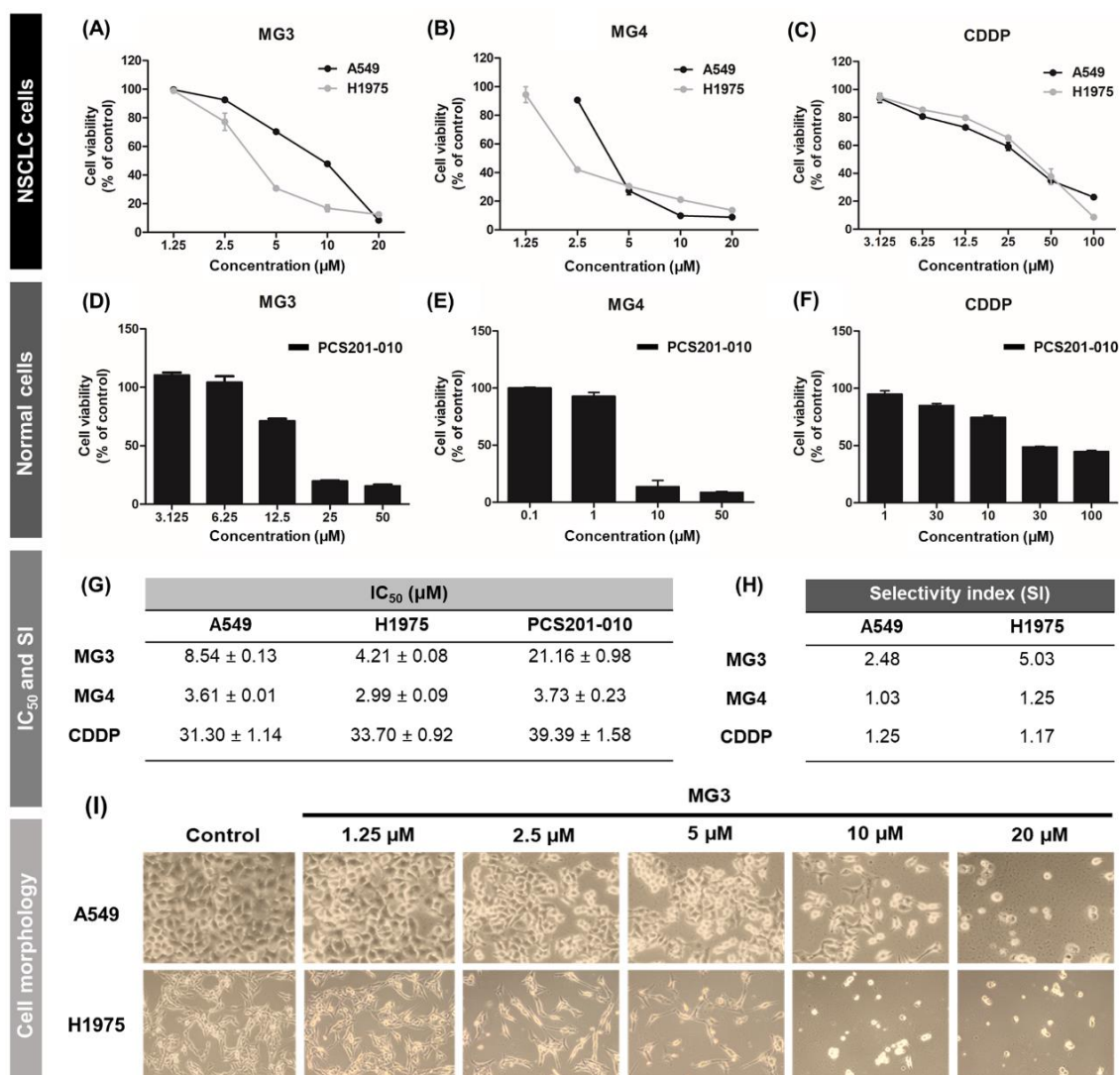


Figure 6 Cell viability of NSCLC (A-C) and PCS201-010 (D-F) cell lines after treatment with MG3, MG4, and CDDP for 48 h. The IC₅₀ (µM) and SI of three focused compounds against all studied cell lines are shown in (G) and (H), respectively. (I) The morphological changes of two NSCLC cell lines treated with MG3 at various concentrations for 48 h.

2.3.3 Butoxy mansonone G induces apoptosis in A549 and H1975 cell lines

To determine whether apoptotic mechanism is involved in MG3-induced cytotoxicity in NSCLC cells, flow cytometric analysis of Annexin V/PI stained cells was carried out. Following 24 h of treatment, MG3 at 16 μM significantly induced apoptotic cell death in A549 cells, whereas MG3 at 2 μM induced significant apoptosis in H1975 cells (Fig. 7A-B), indicating that apoptosis-inducing effect of MG3 was more pronounced in NSCLC cells carrying mutant EGFR than in NSCLC cells carrying wild-type EGFR. Additionally, MG3 at 8 μM dramatically induced apoptosis in H1975 cells (~50%) which was higher than CDDP, reflecting a strong cytotoxic activity. It should also be noted that, when compared to 30 μM CDDP, the lower concentrations of MG3 at: (i) 16 μM (~2-fold lower) for A549 cells and (ii) 2 μM (15-fold lower) for H1975 cells can significantly trigger cell apoptosis.

To further confirm the apoptosis-inducing effect of MG3 on NSCLC cells, the cleavage of procaspase-3 and poly(ADP-ribose) polymerase (PARP), key hallmarks of apoptosis, was determined using western blotting. Note that for H1975 cell line, MG3 at 8 μM was highly toxic to the cells (as evidenced by flow cytometric analysis), leading to a low concentration of extracted proteins; and thus, this concentration was excluded from this study. As shown in Fig. 7C-D, MG3 (16 μM for A549 and 2 μM for H1975) as well as 30 μM CDDP significantly induced the cleavage of procaspase-3 and PARP, which was in good agreement with a significant apoptotic cell death detected by flow cytometric analysis.

We next characterized whether caspase-3 activation (Fig. 7C-D) is mandatory for MG3-induced apoptosis. NSCLC cells were pretreated with Z-Val-Ala-Asp-(OMe)-fluoromethylketone (Z-VAD(OMe)-FMK), an irreversible pan-caspase inhibitor, for 1 h prior to challenge with MG3 for 24 h. As shown in Fig. 7E-F, both MG3 and CDDP decreased cell viability by ~40% in both A549 and H1975 cells, and Z-VAD(OMe)-FMK alone did not affect the cell viability of cancer cells (%CV of ~100). Intriguingly, blockage of caspase activation by Z-VAD(OMe)-FMK inhibitor significantly restored cell viability in A549 and H1975 cells for both MG3- and CDDP-treated groups. These findings clearly

demonstrated that activation of caspase-3 enzyme plays a crucial role in MG3-induced cell apoptosis.

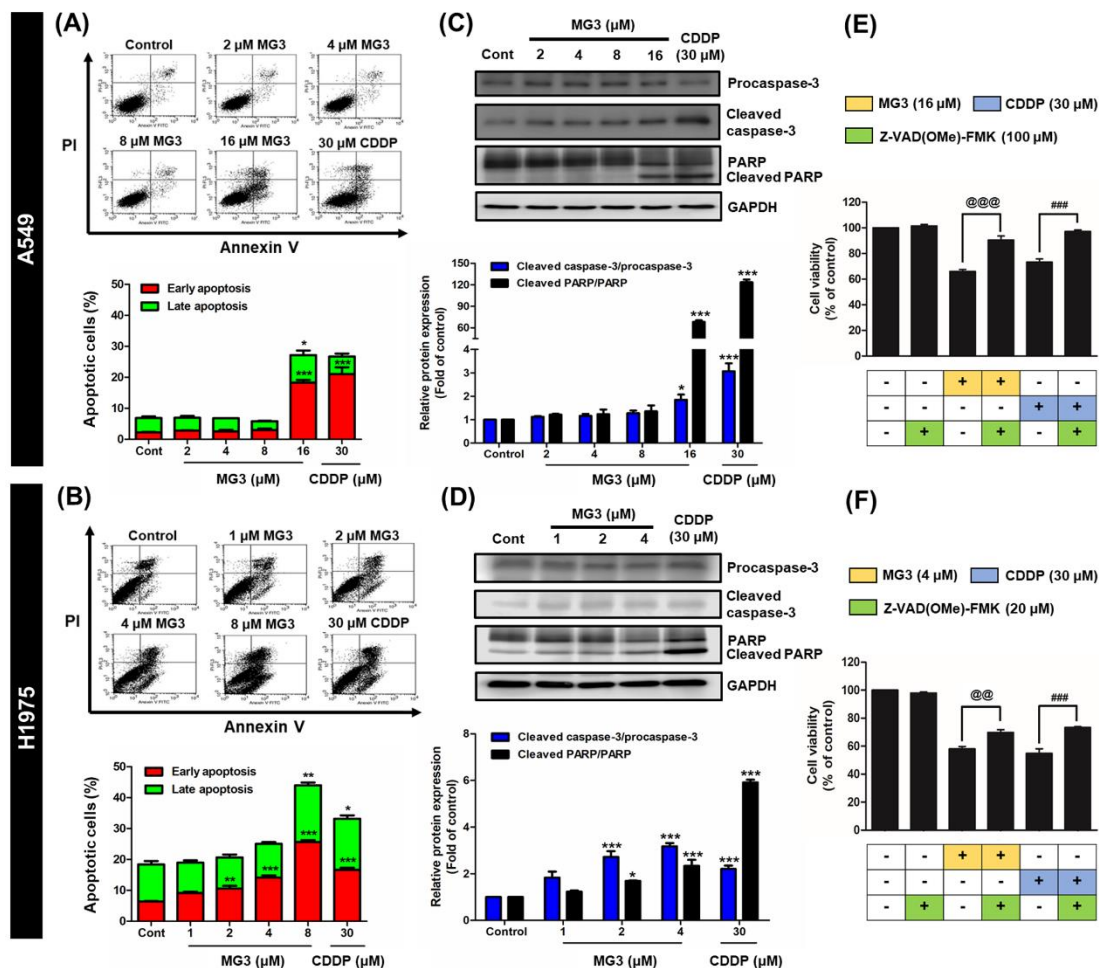


Figure 7 Flow cytometric analysis of Annexin V/PI stained cells after MG3 and CDDP treatments for 24 h on (A) A549 and (B) H1975 cells. Western blot analysis of apoptotic markers, caspase-3 and PARP, for (C) A549 and (D) H1975 cells. Inhibition of MG3-induced apoptosis by the pan caspase inhibitor Z-VAD(OMe)-FMK in (E) A549 and (F) H1975 cells. Data are expressed as mean \pm SEM (n = 3). * p <0.05, ** p <0.01, and *** p <0.001 vs. control. @ p <0.05, @@ p <0.01, and @@@ p <0.001 vs. MG3. # p <0.05, ## p <0.01, and ### p <0.001 vs. CDDP.

2.3.4 Butoxy mansonone G inhibits STAT3 and Akt signaling pathways in NSCLC cell lines

To elucidate the effect of MG3 on EGFR-mediated survival signaling pathways, western blot analysis was performed. As shown in Fig. 8A-B, MG3 and CDDP significantly inhibited the phosphorylation of STAT3 and Akt in a concentration-dependent manner in both A549 and H1975 cells. Conversely, the expression of p-Erk was significantly increased after treatment with such two compounds. Remarkably, MG3, although at lower concentrations (~2-fold lower for A549 and 15-fold lower for H1975), exhibited similar effects on EGFR-mediated survival signaling pathways as 30 μ M CDDP.

We further investigated whether the downregulation of p-STAT3 and p-Akt caused by MG3 was mediated through the inhibition of p-EGFR. The data in Fig. 8C-D demonstrate that the addition of EGF dramatically increased p-EGFR in A549 vehicle-treated cells. On the other hand, EGF has no effect on phosphorylation of EGFR in H1975 control cells, since T790M mutation enhances the ATP binding affinity without EGF binding [61]. The 10 μ M erlotinib, an EGFR TK inhibitor, totally inhibited the phosphorylation of EGFR in A549 cells, which was in agreement with a previous study [62]. However, it should be noted that pre-treatment with MG3 and CDDP did not alter the expression levels of p-EGFR following EGF stimulation, indicating that EGFR was not the preferential binding site for both MG3 and CDDP.

Taken together, the proposed underlying mechanisms of MG3 against two NSCLC cell lines are illustrated in Fig. 8E showing that MG3 inhibited downstream activity of STAT3 and Akt without interfering phosphorylation of EGFR, whilst the phosphorylation of Erk was significantly enhanced upon MG3 treatments. These signal transduction effects led to the activation of caspase-3, cleavage of PARP, and induction of apoptosis, respectively.

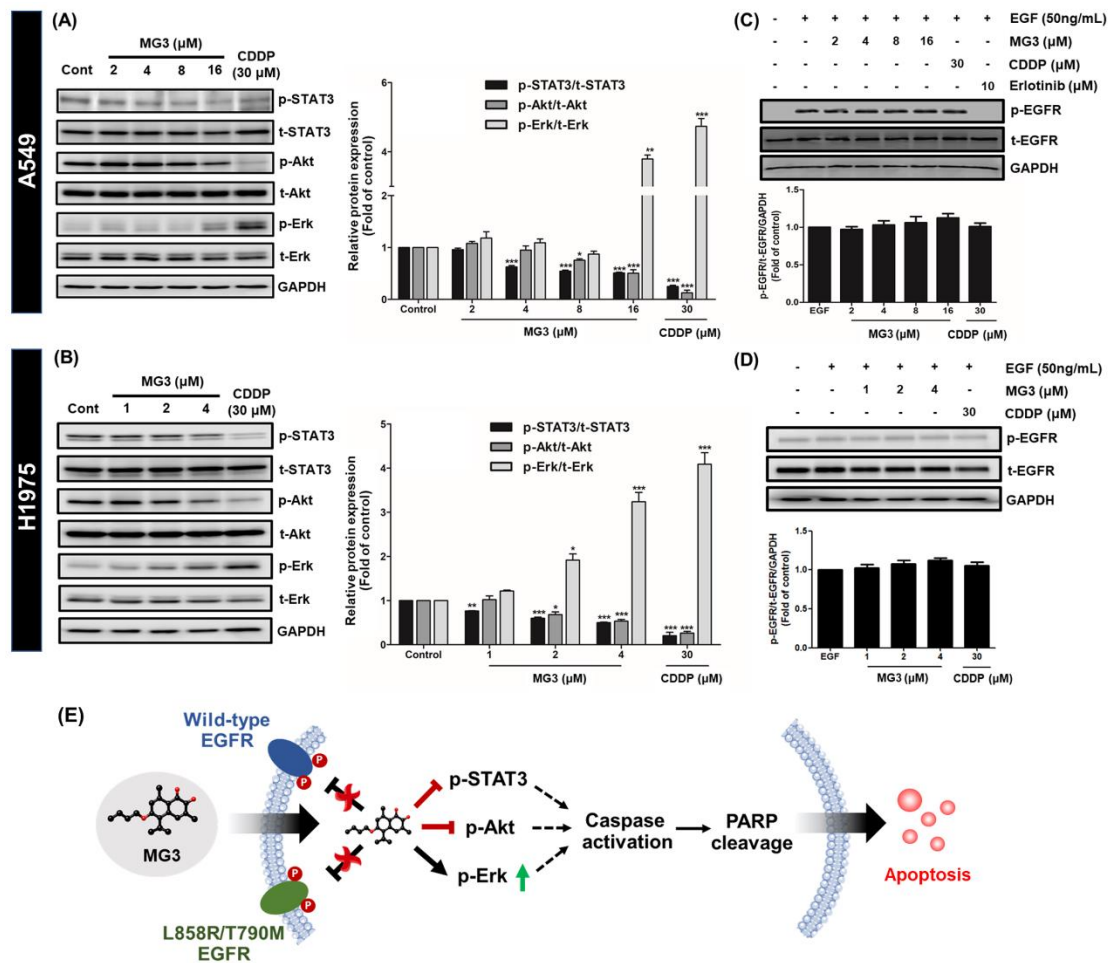


Figure 8 MG3 dose-dependently inhibits the phosphorylation of STAT3 (Tyr705) and Akt (Ser473) in (A) A549 and (B) H1975 cells at 24 h. The expression of p-Erk (Thr202/Tyr204) is found to be increased upon MG3 and CDDP treatments. The phosphorylation of EGFR (Y1068) for both (C) A549 and (D) H1975 cells is not significantly affected by MG3 and CDDP treatments. (E) Proposed mechanisms of MG3 against two studied NSCLC cell lines, in which MG3 promotes cell apoptosis through the inhibition of p-Akt and p-STAT3 as well as through the activation of MAPK signaling pathway. Data are expressed as mean \pm SEM of three independent experiments. * $p \leq 0.05$, ** $p \leq 0.01$, and *** $p \leq 0.001$ vs. control.

Since we found that MG3 inhibits p-STAT3 and p-Akt, we further elucidated the atomistic binding mechanisms of MG3 against such target proteins, which culminated in phosphorylation inhibition, using multiple computational modeling techniques. The

structural and dynamics properties, ligand-protein interactions, and binding affinity of MG3 in complex with two signaling proteins were compared to the known inhibitors as well as the apo-proteins.

2.3.5 Predictive binding affinity of butoxy mansonone G against STAT3 and Akt signaling proteins

To estimate the binding affinity of MG3 against the focused proteins STAT3 and Akt in comparison with their known inhibitors, the molecular mechanics combined with generalized Born surface area (MM/GBSA) method was applied on the 200 molecular dynamics (MD) snapshots extracted from the last 200-ns simulations. The binding free energy (ΔG_{bind}) together with its energy components are summarized in **Table 2**. In the case of STAT3, the calculated ΔG_{bind} results were ranked in the order of MG3 (-8.54 kcal/mol) \ll cryptotanshinone (CTS, -5.09 kcal/mol) $<$ S3I201 (-3.73 kcal/mol), suggesting that the susceptibility of MG3 was significantly higher than those of known inhibitors. By considering Akt models, the ΔG_{bind} of MG3 (-9.19 kcal/mol) was in the range of uprosertib (-10.45 kcal/mol) and H8 (-9.68 kcal/mol) inhibitors. Due to the nonpolar structure of MG3 and CTS (**Fig. 5A-B**), the molecular mechanics energy (ΔE_{MM}) revealed that van der Waals interaction (ΔE_{vdW}) was the main force driving protein-ligand complexation (ΔE_{vdW} of -35.77, -39.14, and -35.61 kcal/mol for MG3/STAT3, MG3/Akt, and CTS/STAT3, respectively). By contrast, the electrostatic attraction (ΔE_{ele}) was found to mainly contribute toward S3I201/STAT3 (ΔE_{ele} of -110.36 kcal/mol), uprosertib/Akt (ΔE_{ele} of -146.76 kcal/mol), and H8/Akt (ΔE_{ele} of -168.13 kcal/mol) complexes, since these inhibitors contain the ionic charged moiety in the chemical structures (R-COO⁻, R-NH₃⁺, and R-NH⁺-R groups, respectively, **Fig. 5B**).

Notably, the obtained ΔG_{bind} of all studied inhibitors agreed well with the trend of experimental ΔG_{bind} ($\Delta G_{\text{bind, exp}}$), implying that our free energy calculations could successfully predict the binding affinity of protein/inhibitor complexes. Taken together, the experimental and theoretical results suggested that the anticancer activity of MG3 was due to binding to STAT3 and Akt signaling proteins.

Table 2 The MM/GBSA ΔG_{bind} and its energy components (kcal/mol). The $\Delta G_{\text{bind, exp}}$ was calculated using the equation of $\Delta G_{\text{bind, exp}} = RT \ln IC_{50}$, where R is the gas constant (1.985×10^{-3} kcal/mol/K), T is the experimental temperature (K), and IC_{50} is the half maximal inhibitory concentration (μM).

	STAT3			Akt		
	CTS	S3I201	MG3	Uprosertib	H8	MG3
ΔE_{ele}	-6.80 ± 0.44	-110.36 ± 3.35	-1.56 ± 0.30	-146.76 ± 1.43	-168.13 ± 1.16	-9.43 ± 0.17
ΔE_{vdW}	-35.61 ± 0.21	-37.47 ± 0.23	-35.77 ± 0.22	-44.62 ± 0.20	-33.92 ± 0.18	-39.14 ± 0.17
ΔE_{MM}	-42.41 ± 0.48	-147.83 ± 3.36	-37.33 ± 0.37	-191.39 ± 1.48	-202.05 ± 1.18	-48.57 ± 0.24
$\Delta G_{\text{solv, non-polar}}$	-4.46 ± 0.02	-5.71 ± 0.02	-4.89 ± 0.02	-6.04 ± 0.02	-4.95 ± 0.01	-4.85 ± 0.01
$\Delta G_{\text{solv, polar}}$	23.99 ± 0.39	124.43 ± 3.15	15.67 ± 0.27	162.16 ± 1.22	176.02 ± 1.12	24.55 ± 0.15
ΔG_{solv}	19.53 ± 0.39	118.72 ± 3.15	10.78 ± 0.27	156.11 ± 1.22	171.07 ± 1.12	19.70 ± 0.15
$\Delta E_{\text{ele}} + \Delta G_{\text{solv, polar}}$	17.19 ± 0.58	14.07 ± 4.59	14.11 ± 0.40	15.40 ± 1.87	7.89 ± 1.61	15.12 ± 0.22
$\Delta E_{\text{vdW}} + \Delta G_{\text{solv, non-polar}}$	-40.07 ± 0.21	-43.18 ± 0.23	-40.66 ± 0.22	-50.66 ± 0.20	-38.87 ± 0.18	-43.99 ± 0.17
$-T\Delta S$	17.78 ± 1.69	25.38 ± 2.16	18.02 ± 1.93	24.82 ± 0.90	21.28 ± 0.66	19.67 ± 1.54
ΔG_{bind}	-5.09 ± 0.42	-3.73 ± 0.58	-8.54 ± 0.48	-10.45 ± 0.38	-9.68 ± 0.29	-9.19 ± 0.39
$\Delta G_{\text{bind, exp}}$	-7.26	-5.54	n/a	-9.19	-6.46	n/a
IC_{50} (μM)	4.6 [63]	86 [64]	n/a	0.18 [65]	18 [66]	n/a

2.3.6 Key binding residues

The per-residue decomposition free energy ($\Delta G_{\text{bind}}^{\text{residue}}$) calculation based on the MM/GBSA method was used to investigate the crucial amino acid residues involved in ligand binding within the SH2 domain of STAT3 and the ATP-binding pocket of Akt. The total contributing amino acids of all complexes are shown in Fig. 9, where the negative

and positive $\Delta G_{\text{bind}}^{\text{residue}}$ values represent respectively the stabilization and destabilization energies of the considered residue.

In the case of STAT3, there are three subpockets in the SH2 domain, including (i) pY+0 (residues 591 and 609–620), (ii) pY-X (residues 592–608), and (iii) pY+1 (residues 621–639) pockets. The pY+0 site contains several polar residues responsible for phosphotyrosine (pTyr) binding, while the two subsites pY-X and pY+1 are the hydrophobic regions (**Fig. 9A**). Note that among residues 458–722 of STAT3 model, only the contribution from the residues 540–660 is shown. The obtained results demonstrated that there were four and eight amino acids involved in the binding of the two STAT3 inhibitors CTS (e.g., I589, E594, L598, and I634) and S3I201 (e.g., K557, I589, E594, I597, L607, R609, I634, and Q635), respectively; whereas MG3 interacted with the residues L598, T632, and I634 inside the hydrophobic subsites pY-X and pY+1. Notably, the contribution from residues L598 and I634 toward MG3/STAT3 complex matched to the known inhibitors. The lipophilic group of ligands, including the cyclohexane ring of CTS, the *O*-tosyl group of S3I201, and the alkyl side chain of MG3 were found to be encapsulated into the hydrophobic pY+1/pY-X pocket of STAT3, while the polar moieties of S3I201 orientated in the pY+0 site, forming hydrogen bond (H-bond) interactions (**Fig. S1**).

For Akt signaling protein (**Fig. 9B**), the amino acids establishing inhibitor binding were: (i) V164, E234, E278, M281, T291, F438, and F442 for uprosertib and (ii) V164, Y229, A230, M281, and T291 for H8. Notably, the key binding residues V164, E234, M281, and F438 involved in MG3 binding were identical to those of the Akt inhibitors. Interestingly, the ligand binding mode of Akt models shared a structurally-related characteristic, in which the aromatic moiety of all studied compounds approached the key residue M281.

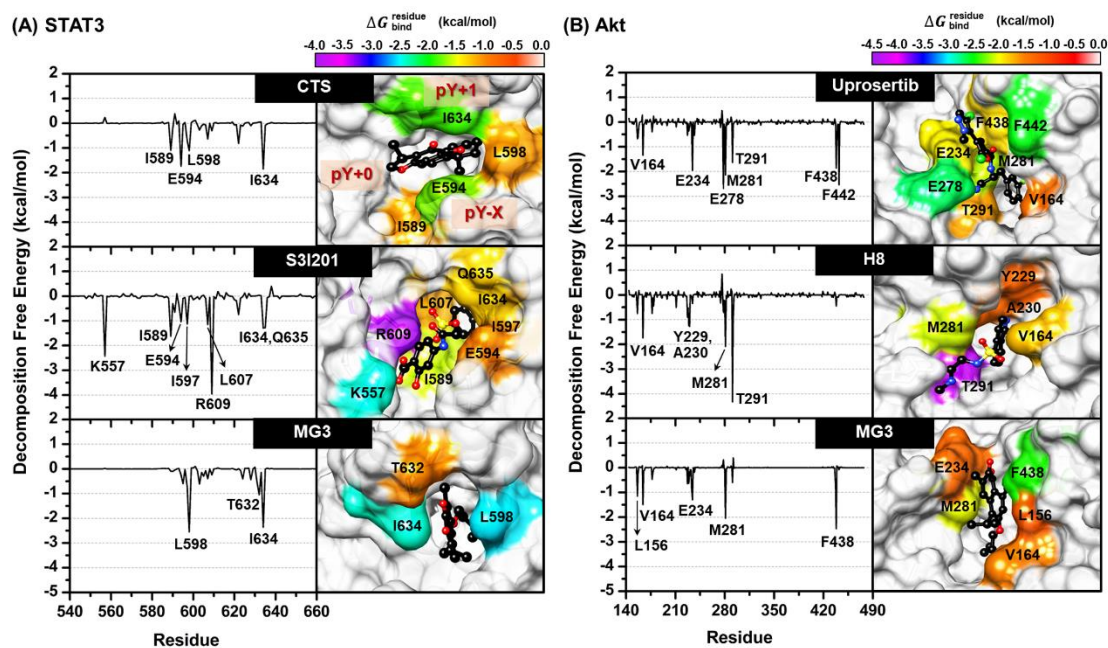


Figure 9 $\Delta G_{\text{bind}}^{\text{residue}}$ (kcal/mol) of (A) STAT3 and (B) Akt. The amino acids involved in ligand binding are shaded according to their $\Delta G_{\text{bind}}^{\text{residue}}$, in which the highest and lowest energies are ranged from red to magenta, respectively.

2.3.7 *In silico* study on conformational change of STAT3 and Akt upon butoxy mansonone G binding

The structurally relevant motions of STAT3 and Akt signaling proteins derived from MG3 recognition were investigated in comparison with the apo-protein using principal component analysis (PCA) on the 2000 MD snapshots taken from the last 200-ns simulations. The results are illustrated in Fig. 10, where the arrow and its length indicate the direction and amplitude of motions, respectively. Note that among residues 458–722 of STAT3 model, only the protein motion from the residues 499–688 is shown.

The first 15 PC modes showed the % accumulated variance of (i) 72.99 and 93.68 for apo and holo forms of STAT3 and (ii) 55.21 and 57.95 for apo and holo forms of Akt, respectively. The percentage of variances for PC1 of all systems was much higher than that of PC2, indicating that this mode could represent the significant motions of proteins.

By considering STAT3 model (Fig. 10A), the first principal component (PC1) showed that MG3 binding importantly converted the direction of motions of overall protein to approach the ligand in a different manner from that of the apo form. Remarkably, the residues 592–601 on pY-X (green) and 625–633 on pY+1 (magenta) hydrophobic pockets of STAT3 SH2 domain displayed not only increased direction of motions, but also enhanced amplitude of motions upon MG3 binding mainly through vdW interaction (Table 2). For the Akt systems (Fig. 10B), the residues 157–163 on glycine-rich loop (GRL, green) inside the ATP-binding pocket of apo form pointed outward from the binding site, making it an opened conformation. Intriguingly, a complexation with MG3 led to the conversion of direction of GRL motion to be located closer to the MG3 molecule, resulting in a closed conformation.

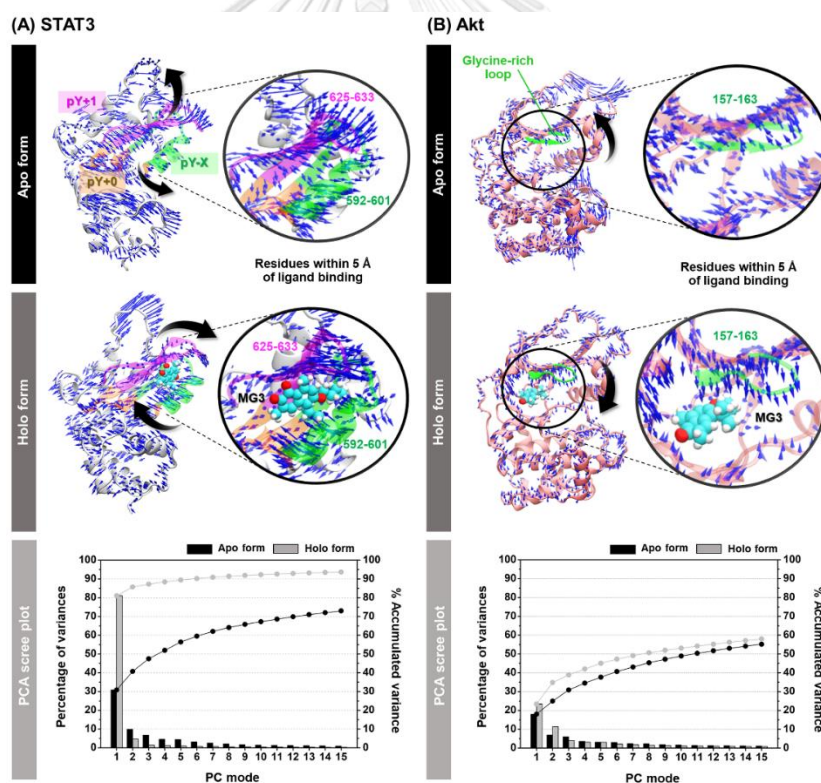


Figure 10 Porcupine plot of apo and holo forms of (A) STAT3 and (B) Akt across the PC1. The residues within 5 Å of ligand are presented in circle where the MG3 molecule is shown in vdW model. The PCA scree plot of quantitative characters for each protein is given below, in which the columns in black and grey represent the data for apo and holo forms, respectively.

2.4 Discussion

Platinum-based chemotherapy and the first-generation TKIs have been used as the first-line treatment for NSCLC patients carrying wild-type and mutant EGFRs, respectively [46, 47, 49, 50]. However, acquired drug resistance is inevitable after a progression-free period of approximately 9 to 13 months. Therefore, a novel anticancer compound that remains effective in both NSCLC cells expressing wild-type and T790M-positive EGFRs is critically needed. MG, a naphthoquinone-containing compound extracted from *Mansonia gagei* Drumm, was shown to exhibit anticancer activity toward the A2780 ovarian cancer cell line with an IC_{50} of $10.2 \pm 0.9 \mu\text{M}$ [27]. Recently, the etherification of the hydroxyl group of MG has been reported to potentially result in antibacterial activity as well as to suppress adipocyte differentiation and lipid accumulation by more than natural MG [24, 28]. In the present study, we experimentally and theoretically elucidated the cytotoxic activity of MG and its semi-synthetic derivatives against A549 (expressing wild-type EGFR) and H1975 (expressing L858R/T790M EGFR) NSCLC cell lines. We found that, among ten ether analogs, MG3 and MG4 displayed the most potent cytotoxicity toward both A549 and H1975 cells (Table 1). Notably, the IC_{50} values of such two MGs were much lower than IC_{50} of CDDP for both NSCLC cell lines (Figure 2G). Introduction of longer carbon side chain to MG makes its chemical structure more hydrophobic, which culminate in increasing cellular uptake [24, 67]. Therefore, it is likely that chemical modification of MG via increasing number of carbon units of alkyl side chain enhances the cytotoxicity of MG1-MG4 against NSCLC cell lines. Conversely, MG5 containing twelve carbons showed a dramatic reduction of cytotoxic activity, which may be due to the cut-off effect [24, 68].

Unfortunately, we found that MG4 was highly toxic toward the PCS201-010 normal skin fibroblast cell line (IC_{50} of $3.73 \pm 0.23 \mu\text{M}$), thus, this compound was excluded from our mechanistic studies. Our present findings are consistent with others showing that MG3 was less toxic to differentiated adipocytes than MG4 [28]. However, it should be noted that only one normal cell line was tested in this study; thus, further investigations on other normal cell lines as well as *in vivo* studies should be conducted.

Interestingly, as compared to the commercial EGFR-targeted drugs, the SI of gefitinib (SI = 0.81) and osimertinib (SI = 1.15) toward A549 NSCLC and normal human bronchial epithelial (HBE) cell lines is much lower than MG3 (2.48, Fig. 6H) [69]. In addition, the SI of chemotherapeutic drug methotrexate and β -lapachone, a novel anticancer drug currently under study in phase I/II clinical trials, was respectively 0.02 and 1.28 [70-72], reflecting a strong toxicity. Altogether, MG3, which showed a lower toxicity (IC_{50} of $21.16 \pm 0.98 \mu\text{M}$) against PCS201-010 cells, was then selected for further studying the mechanisms underlying cell death.

Activation of caspase enzymes leads to the generation of signaling cascades responsible for apoptotic events [73]. In the present study, we documented that MG3 induced caspase-dependent apoptosis in both A549 and H1975 cells, in which H1975 cells expressing mutant EGFR were more susceptible to apoptosis-inducing effect of MG3 rather than A549 cells expressing wild-type EGFR. The reason for this observation is that L858R/T790M EGFR stimulates cell growth through the dramatic enhancement of catalytic phosphorylating activity over wild-type EGFR [74], which can provide more preferential target signaling proteins for MG3, as evidenced by the significant downregulation of p-STAT3 and p-Akt at low concentrations of $1 \mu\text{M}$ and $2 \mu\text{M}$, respectively, in H1975 cells (Fig. 8B). Previous studies demonstrated that CDDP induced apoptosis through the activation of caspase-3 and PARP [75-78]. Similarly, this study revealed that CDDP promoted apoptotic cell death through the activation of caspase cascades (Fig. 7C-F).

Many lines of evidence have shown that several naphthoquinone-containing compounds, such as shikonin, plumbagin, furano-1,2-naphthoquinone, ramentaceone, mansonone E, and CTS significantly inhibited STAT3 and Akt signaling pathways in various kinds of malignancies [63, 79-85]. In agreement with these reports, data in Figures 4A-B show that our *ortho*-naphthoquinone MG3 concentration-dependently inhibited phosphorylation of STAT3 and Akt in both A549 and H1975 cell lines, which strongly correlated with MM/GBSA free energy calculations showing that MG3 could possibly interact with SH2 domain of STAT3 and ATP-binding pocket of Akt in a similar manner to

that of known STAT3 and Akt inhibitors (**Table 2**). Remarkably, our structural analyses on both STAT3 and Akt inhibitors were consistent with other experimentally/theoretically derived data as follows. The binding orientations ((i) *O*-tosyl group of S3I201 occupying the pY-X pocket and (ii) cyclohexane group of CTS pointing toward the pY+1 hydrophobic region), key binding amino acid residues (e.g., I597, R609, and Q635 for S3I201 and I634 for CTS), and H-bond formation patterns of STAT3 inhibitors displayed a similar manner to several research works [63, 86-89]. It was evidenced that M281 is the key binding residue for hydrophobic packing against indole/phenyl ring of Akt inhibitors through $\epsilon\text{-CH}\cdots\pi$ interaction [90, 91]. In correlation with this fact, our $\Delta G_{\text{bind}}^{\text{residue}}$ data demonstrated that the aromatic moiety of all studied ligands pointed toward M281 residue (**Fig. 9B**). Since the α,β -unsaturated carbonyl (α,β -UC) compounds can covalently interact with biological thiols of several kinase proteins via hetero-Michael addition reaction [92], we then measured the distance between the center of mass of α,β -UC unit of MG3 and the thiol group (SH-) of cysteine residues using the final snapshot from the 500-ns MD simulation. The obtained results revealed that α,β -UC part of MG3 positioned far away (>15 Å) from the cysteine residues in Akt's active site (**Fig. S2**), implying that MG3 could not form the covalent adduct with Akt. Altogether, MG3 showed a somewhat similar binding pattern to STAT3 and Akt inhibitors upon molecular complexation, suggesting that MG3 could likely inhibit the phosphorylation of such proteins in a similar fashion to that of the known inhibitors. By conducting PCA, we discovered that MG3 importantly induced large conformational changes of STAT3 and Akt, especially in ligand-binding pocket, as strongly evidenced by the superimposed X-ray crystal structures between apo (PDB ID: 1GZN [93]) and holo forms (PDB ID: 4GV1 [94]) of Akt (**Fig. S3**). This might explain the atomistic mechanisms underlying the inhibition of phosphorylation-induced activation of such signaling protein mediated by MG3, which culminate in cell apoptosis. It should be noted that *in silico* results from MD simulations were suggestive; thus, further experimental techniques (e.g., isothermal titration calorimetry (ITC), circular dichroism

(CD), and surface plasmon resonance (SPR)) should be conducted to confirm our findings.

Although our results showed that MG3 inhibited STAT3 and Akt activities, MG3 did not interfere with the phosphorylation of EGFR, indicating that MG3 preferentially targeted EGFR's downstream signaling molecules STAT3 and Akt rather than upstream EGFR. We also discovered that treatment with CDDP did not cause any significant changes in the expression of p-EGFR, which was in good agreement with the fact that DNA is a molecular target for CDDP [48, 95], and the changes of signaling cascades are derived from platinum-DNA adduct [95]. Because PARP cleavage was more pronounced in cells treated with CDDP than cells treated with MG3, it is possible that NSCLC cells induced PARP in order to repair damaged DNA caused by CDDP-mediated platination. In contrast to CDDP, DNA was found to be the non-preferential binding site for MG3, as evidenced by: (i) the lower level of cleaved PARP than CDDP (Figures 3C–D), (ii) the higher CDOCKER interaction energy (-32.22 kcal/mol) than CDDP (-44.24 kcal/mol), and (iii) the high distance between the center of mass (C_m) of MG3 and DNA ($d(C_m(\text{MG3})-C_m(\text{DNA}))$) obtained from three independent 100-ns MD simulations (Fig. S4). Altogether, MG3 exhibited overall mechanisms of action similar to those of CDDP, but preferred targeting proteins rather than DNA, which can serve as a promising anticancer agent for NSCLC patients harboring CDDP resistance.

In contrast to STAT3 and Akt, we noticed that treatment with MG3 and CDDP induced phosphorylation of Erk in both A549 and H1975 cells. A significant upregulation of p-Erk was found to be correlated with the generation of cleaved caspase-3 and cleaved PARP (Fig. 7C–D). These findings were consistent with previous studies demonstrating that high level of p-Erk can promote cell apoptosis through the activation of caspase-3 [96, 97]. Erk plays a dual role in both cell proliferation and cell death [96], and activation of Erk is extremely important for CDDP-induced apoptosis [95, 97, 98]. Thus, it is possible that, in addition to inhibition of STAT3 and Akt, cytotoxicity of MG3 may be mediated through activation of Erk in NSCLC cells.

Altogether, our present study provided the first step of the underlying mechanisms of MG3 toward EGFR-mediated signaling pathways in NSCLC cell lines expressing wild-type and mutant EGFRs. However, further investigations on other signaling pathways as well as the kinase screening assays need to be performed in order to gain more insights into the signal transduction inhibitions caused by MG3.

2.5 Materials and methods

2.5.1 Experimental part

2.5.1.1 Chemical reagents and antibodies

MG was extracted from the heartwood of *M. gagei*, whereas MG ether derivatives were semi-synthesized according to the previous study [24]. Bovine serum albumin (BSA), dimethyl sulfoxide (DMSO), CDDP, MTT, and protease inhibitor were purchased from Sigma-Aldrich (St. Louis, MO, USA). RIPA lysis buffer was purchased from Thermo Fisher Scientific (Waltham, MA, USA). The protein assay reagents were purchased from Bio-Rad (Hercules, CA, USA). Human epidermal growth factor (EGF, 8916) and antibodies against phospho-EGFR (p-EGFR, 2234), total-EGFR (t-EGFR, 4267), phospho-STAT3 (p-STAT3, 9145), total-STAT3 (t-STAT3, 12640), phospho-Akt (p-Akt, 4060), total-Akt (t-Akt, 4691), phospho-Erk (p-Erk, 4377), total-Erk (t-Erk, 4695), caspase-3 (9662), PARP (9542), GAPDH (5174), and anti-rabbit IgG HRP-linked antibody (7074) were purchased from Cell Signaling Technology (Santa Cruz, CA, USA). The pan-caspase inhibitor Z-VAD(OMe)-FMK (ab120487) was purchased from Abcam (Cambridge, UK).

2.5.1.2 Cell lines and culture

Human NSCLC cell lines A549 and H1975 as well as human normal skin fibroblast cell line (PCS201-010) were purchased from American Type Culture Collection (ATCC, Manassas, VA, USA). A549 cells were grown in Dulbecco's modified Eagle's minimal essential medium (DMEM; Gibco, Grand Island, NY, USA) supplemented with 10% fetal bovine serum (FBS; Gibco), 100 U/mL penicillin, and 100 µg/mL streptomycin

(Gibco). H1975 cells were cultured in RPMI-1640 medium containing 10% FBS, 100 U/mL penicillin, and 100 µg/mL streptomycin. The DMEM with high glucose (4500 mg/L) supplemented with 10% FBS, 100 U/mL penicillin, and 100 µg/mL streptomycin was used for culturing PCS201-010 cells. All cells were maintained at 37 °C in a humidified 5% CO₂ atmosphere.

2.5.1.3 Cell viability assay

Cell viability was assessed using the MTT assay. Cells were seeded into 96-well plates at a density of 5×10^3 cells/well for H1975 and PCS201-010 as well as of 3×10^3 cells/well for A549. After overnight incubation, cells were treated with MGs at 10 and 100 µM for 48 h. Note that, due to the low solubility of MG4 and MG10, the highest prepared concentration was 50 µM. Subsequently, the MTT solution (5 mg/mL) was added and then incubated for 4 h. The medium was removed and 150 µL of DMSO was added to each well. Finally, the absorbance of formazan product was measured at a wavelength of 570 nm using a LabSystems Multiskan MS microplate reader (Thermo Scientific, Vantaa, Finland). The selectivity index (SI) was calculated according to the following equation: $SI = IC_{50} \text{ for normal cells} / IC_{50} \text{ for cancer cells}$.

2.5.1.4 Western blotting

A549 and H1975 cells were seeded into a 6-well plate at a density of 2×10^5 cells/well and 3×10^5 cells/well, respectively. After overnight incubation, cells were treated with indicated compounds. Note that the concentration of MG3 was varied to two-fold, one-half, and one-fourth of its IC_{50} , whereas the positive control CDDP at the IC_{50} of 30 µM was used. After 24 h of incubation, cells were rinsed twice with cold PBS, homogenized in RIPA buffer containing protease inhibitor, and incubated on ice for 45 min. Total protein (20 µg) were separated on 8% SDS-PAGE and subsequently transferred to a PVDF membrane. The membrane was blocked with 3% non-fat dry milk for 1 h and then incubated with primary antibody at 4 °C overnight. After incubation, the membrane was washed thrice with TBST buffer (5 min each) and incubated with HRP-

linked secondary antibody for 2 h at room temperature. Immunoreactive bands were detected using HRP substrate (Millipore, Billerica, MA, USA) and quantitatively measured using Image Studio Lite software (LI-COR, Lincoln, NE, USA). Glyceraldehyde 3-phosphate dehydrogenase (GAPDH) was used as internal control for protein normalization.

Note that for detecting p-EGFR, it was reported that the expression of p-EGFR could not be clearly detected at 24 h due to the short half-life of activated EGFR ($\sim 1.5\text{--}4$ h) [99]; thus, we pre-incubated NSCLC cell lines with the indicated concentrations of MG3 and CDDP in serum free media for 1 h prior to stimulation of EGFR with EGF (50 ng/mL) for 10 min.

2.5.1.5 Flow cytometric evaluation of apoptosis

NSCLC cells were plated on a 6-well plate at a density of 2×10^5 cells/well for A549 cells and 3×10^5 cells/well for H1975 cells. After overnight incubation, cells were treated with 1, 2, 4, 8, and 16 μM MG3 and 30 μM CDDP for 24 h. After treatment, cells were harvested by trypsinization and collected by centrifugation at 1500 rpm. Subsequently, cells were washed with cold PBS and stained with 3 μL of Annexin-V fluorescein dye and 1 μL of propidium iodide (PI) at room temperature in the dark for 20 min. After that, cells were resuspended in 400 μL of cold assay buffer containing 0.01 M HEPES, 2.8 mM CaCl_2 , and 125 mM NaCl. The percentage of apoptotic cells was quantitatively measured using BD FACSCalibur flow cytometer (BD Bioscience, Heidelberg, Germany).

2.5.1.6 Statistical analysis

The quantitative data are expressed as mean \pm standard error of mean (SEM) of triplicate experiments. Differences between groups were determined using one-way analysis of variance (ANOVA) followed by a Turkey post hoc test. Differences were considered to be significant at $p \leq 0.05$.

2.5.2 Computational part

2.5.2.1 Preparation of initial structures

The crystal structures of human STAT3 (PDB ID: 1BG1) [100] and Akt1 (PDB ID: 4GV1) [94] were obtained from Protein Data Bank (PDB). The missing amino acid residues were completed using SWISS-MODEL server [101]. The 3D structure of MG3 was obtained from a previous study [102], whereas the known inhibitors of STAT3 (CTS and S3I201) and Akt1 (uprosertib and H8) were built and subsequently optimized by the HF/6-31(d) level of theory using the Gaussian09 program [103]. The protein-ligand complexes were generated using CDOCKER module implemented in Accelrys Discovery Studio 2.5 (Accelrys Inc.) [104] with 100 docking runs. Note that for STAT3 SH2 domain, prior to perform docking, the protein was relaxed in aqueous solution by conducting a short MD simulation at 298.0 K for 100 ps (as detailed in the next section). The residues K591, R595, R609, E612, W623, and Q635 of STAT3 were defined as binding site with a docking sphere radius of 15 Å, whereas the co-crystallized inhibitor at ATP-binding pocket was used as the docking center for Akt. In addition, the MG3/DNA complex was also tested and simulated. Totally, there are nine simulated models in which the computational details of all system preparations are summarized in **Table S1**.

The protonation states of all ionizable amino acids were characterized using PROPKA 3.0 [105] at pH 7.0. The electrostatic potential (ESP) charges of ligand were computed at the HF/6-31(d) level of theory, whereas the restrained ESP (RESP) charges and corresponding parameters of ligands were generated respectively using antechamber and parmchk modules in AMBER16 according to previous studies [106-108]. The AMBER ff14SB force field [109] was applied for protein, whilst the ligand was treated using the general AMBER force field (GAFF) [110-112]. The missing hydrogen atoms were added using the LEaP module. The added hydrogen atoms were then minimized using 1000 steps of the steepest descents (SD) and 2500 steps of conjugated gradient (CG) approaches. Subsequently, each system was solvated using TIP3P water model [113] in truncated octahedron periodic box with the minimum distance of 10 Å from the system surface. The systems were neutralized using Cl⁻ or

Na⁺ counter ions. The minimization with the SD of 1000 steps and CG of 2500 steps was performed on the added water molecules and counter ions, and finally the entire system was wholly minimized using the same procedure.

2.5.2.2 Molecular dynamics (MD) simulations and binding free energy calculations

MD simulations of all studied complexes were performed under periodic boundary condition using AMBER 16 program. The short-range cutoff of 10 Å was employed for non-bonded interactions, whilst the long-range electrostatic interactions were treated using Particle Mesh Ewald (PME) summation method [114]. SHAKE algorithm [115] was applied to constrain all chemical bonds involving hydrogen. The prepared systems were heated up from 10.0 K to 298.0 K for 100 ps. Subsequently, the MD simulations with *NPT* ensemble were performed at this temperature until reaching 500 ns. From root-mean-square displacement (RMSD) analysis shown in Figure S5, the equilibrated MD trajectories in the last 200-ns simulations of all systems were extracted for further analysis. The cpptraj module was used to compute the structural and dynamics data, including RMSD, ligand-protein H-bond occupation, and protein motion via PCA. Binding free energy of all studied complexes was calculated using the MM/GBSA method [116]. Additionally, the per-residue decomposition free energy based on MM/GBSA approach was evaluated in order to identify crucial amino acids important for ligand recognition.

2.6 Conclusions

The experimental and theoretical results obtained in this study shed light on the anticancer activity and its underlying mechanisms of butoxy MG against human NSCLC cell lines expressing wild-type EGFR and mutant EGFR, which might be useful to develop this compound as a novel anticancer agent and/or can be used as a theoretical guidance for designing and developing a new compound targeting STAT3 and Akt signaling pathways.

CHAPTER III

SUSCEPTIBILITY OF MANSONONE G DERIVATIVES AGAINST HUMAN DNA
TOPOISOMERASE II ALPHA ATPASE DOMAIN

**Molecular Recognition of Naphthoquinone-containing Compounds against Human DNA
Topoisomerase II α ATPase domain: A Molecular Modeling Study**

Panupong Mahalapbutr^a, Phakawat Chusuth^a, Nawe Kungwan^{b,c}, Warinthorn
Chavasiri^d, Peter Wolschann^{a,e,f}, and Thanyada Rungrotmongkol^{a,g*}

^aStructural and Computational Biology Research Group, Department of Biochemistry, Faculty of Science, Chulalongkorn University, 254 Phayathai Road, Bangkok 10330, Thailand

^bDepartment of Chemistry, Faculty of Science, Chiang Mai University, Chiang Mai, 50200, Thailand.

^cResearch Center on Chemistry for Development of Health Promoting Products from Northern Resources, Chiang Mai University

^dDepartment of Chemistry, Faculty of Science, Chulalongkorn University, 254 Phayathai Road, Bangkok 10330, Thailand

^eDepartment of Pharmaceutical Technology and Biopharmaceutics, University of Vienna, Vienna 1090, Austria

^fInstitute of Theoretical Chemistry, University of Vienna, Vienna 1090, Austria

^gPh.D. Program in Bioinformatics and Computational Biology, Faculty of Science, Chulalongkorn University, Bangkok 10330, Thailand

This article has been published in Journal of Molecular Liquids (2017)

3.1 Abstract

Several quinone-based metabolites of anticancer drugs and naturally occurring quinone-containing compounds have been characterized as potent inhibitors toward topoisomerase II α (Topo II α), an essential enzyme involved in maintaining genomic integrity during DNA replication and mitotic division. Mansonone G (MG), a naphthoquinone-containing compound extracted from the heartwood of *Mansonia gagei*, exhibits various biological activities including antitumor potential. In the present study, MG and its semi-synthetic derivatives were selected to study the preferential binding site and dynamics behavior as well as to predict the inhibitory activity against Topo II α using molecular modeling approaches. The molecular docking results revealed that the entire series of MG preferentially target to the ATPase domain. Among all studied MGs, the ester derivative MG14 containing C-10 length exhibited the highest binding affinity against Topo II α and greater than that of the ATP-competitive inhibitor salvicine as well as 1,4-benzoquinone. Interestingly, the MG14 binding could induce the closed form of the turn region (residues 145-151) inside the ATP-binding pocket, implying that this event might be one of the mechanisms underlying Topo II α inhibition. The obtained theoretical information is useful as rational guide for further development of new anticancer agents containing naphthoquinone moiety against Topo II α .

3.2 Introduction

DNA topoisomerase II (Topo II, Fig. 11A) is a nuclear enzyme that plays an important role in a number of DNA-related processes such as replication, transcription, recombination, and mitosis [10, 117, 118]. To maintain genomic integrity during such events, Topo II alleviates the topological constraints of the genetic material by breaking and rejoining the phosphodiester backbone of undesirable regions (i.e., superhelical twists, tangles, and knots) using double-stranded break mechanism [119]. Topo II is a homodimeric enzyme with two catalytically important domains: (i) the N-terminal ATPase domain, which catalyses the hydrolysis of ATP molecules, providing the energy for catalytic processes and (ii) the central domain, which is located at the center of

cleavage/religation domain, comprising the important catalytic residues (TOPRIM sequence and Tyr805) for DNA breaking and resealing (Fig. 11D) [120]. Mammals have two closely related Topo II isoforms, Topo II α and Topo II β , that share 93% of similarity and 81% of identity for their ATPase and cleavage/religation domains [10]. The expression level of Topo II β remains constant throughout the cell cycle, whereas Topo II α is expressed at high levels and dramatically increased during G2/M phase of the cancer cell cycle, making it an ideal protein target for molecularly targeted therapy [10, 121, 122]. There are two classes of Topo II-targeting compounds: (i) Topo II poisons (i.e., etoposide (VP-16), teniposide (VM-26), doxorubicin, amsacrine and mitoxantrone) [123], which can target the catalytic core domain or stabilize the enzyme-DNA complex (known as cleavage complex) [124-126], resulting in DNA strand breaks and (ii) Topo II catalytic inhibitors (i.e., ICRF-193 [127], novobiocin [128], sobuzoxane (MST-16) [129], and merbarone [123]), which affect the catalytic cycle of Topo II without trapping cleavage complexes and generating DNA strand breaks. Quinone moiety has been recognized as a potent pharmacophore for cytotoxicity by National Cancer Institute [130]. The antitumor potentials of quinone-containing compounds against various cancer cell lines have been reported [131-135] and Topo II is the primary targeted enzyme for quinones [136-138].

Mansonone G (MG, Fig. 12A), a 1,2-naphthoquinone-containing compound, is the major product extracted from the heartwood of *Mansonia gagei* [24]. MG exhibits a broad range of biological activities including antioxidative, antifungal, antilarvicidal [139], anti-estrogenic [57], anticholinesterase (ChE) [58], and antitumor (against A2780 ovarian cancer cell line, IC₅₀ of 10.2 μ M) activities [140]. There are many research works proved that quinone-containing compounds inhibit Topo II α enzyme at ATPase domain. Salvicine (Fig. 12C), a diterpenoid quinone, acts as an ATP-competitive inhibitor against the ATPase domain of Topo II α with the IC₅₀ of 18.8 \pm 4.0 μ M and 12.1 \pm 4.2 μ M for DNA decatenation and relaxation, respectively. Due to its potent *in vitro* and *in vivo* antitumor properties, salvicine entered the phase II clinical trials in 2006 [126]. Additionally, 1,4-benzoquinone (1,4-BQ, Fig. 12B) and hydroquinone (HQ) could interact with Asn91,

I141, Ser148, Ser149, and Asn150 residues of the same domain [141]. In addition to 1,4-BQ, 1,2-naphthoquinone (1,2-NQ), 1,4-naphthoquinone (1,4-NQ), and 9,10-phenanthroquinone (9,10-PQ) were found to inhibit Topo II α enzyme by sharing a common binding site with AMP-PNP (5'-adenylyl-imidodiphosphate, a nonhydrolyzable ATP analog) at the ATPase domain, and among these quinone-containing compounds, 1,4-BQ exhibited the lowest IC₅₀ (8.58 \pm 0.8 μ M) for ATPase activity [136]. Interestingly, the synthesized mansonone F (MF) derivatives could inhibit Topo II α activity (IC₅₀ of 1.31-4.88 μ M) better than that of the chemotherapy drug etoposide (60.3 μ M) [142]. However, the mechanism of inhibition including the exact binding site of mansonones against Topo II α enzyme have not been reported yet.

In the present study, molecular docking was applied to study the preferential binding site and evaluate the potent compounds from MG and its derivatives (Fig. 12A) against Topo II α in comparison with the known anti-Topo II α drug etoposide, the catalytic inhibitor merbarone, the ATP-competitive inhibitor salvicine, and the potent compound 1,4-BQ. Subsequently, molecular dynamics (MD) simulations were performed to investigate the structural and dynamics properties as well as intermolecular interactions at the atomic level of those focused MGs complexed with Topo II α in aqueous solution. Moreover, the binding free energies of the enzyme-ligand complexes were estimated by MM/PB(GB)SA methods in order to predict the inhibitory activity of the focused MG analogs toward Topo II α enzyme.

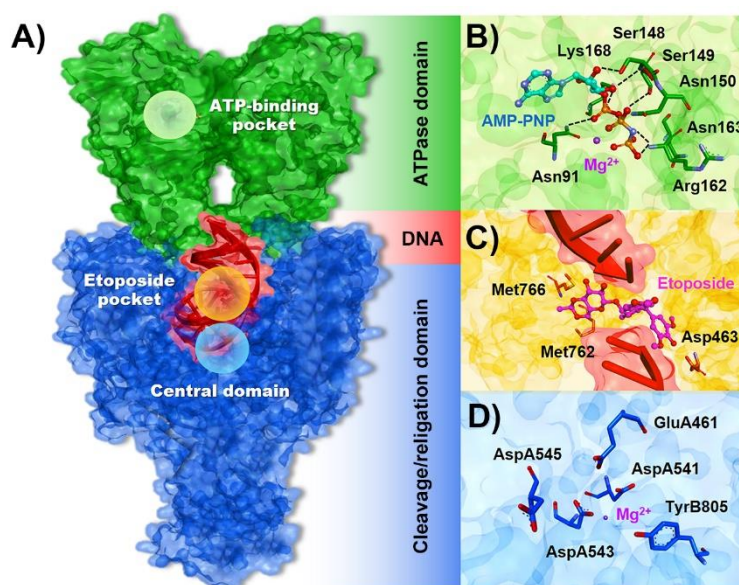


Figure 11 (A) The 3D structure of DNA topoisomerase II α , in which the ATPase and the cleavage/religation domains are shaded by green and dark blue colors. The ATP-binding pocket, etoposide pocket, and central domain are represented by light green, orange, and blue circles, respectively. The close-up regions for (B) ATP-binding pocket, (C) etoposide pocket, and (D) central domain.

3.3 Material and methods

3.3.1 Preparation of initial structures and molecular docking

The crystal structure of human Topo II α ATPase domain complexed with AMP-PNP (PDB ID: 1ZXM) [143] and cleavage/relegation domain complexed with DNA (PDB ID: 4FM9) [144] containing the merbarone binding pocket inside the central domain [120] were obtained from Protein Data Bank (PDB). To search for the etoposide binding pocket, a homology model of Topo II α was constructed by SWISS-MODEL server [101] using etoposide-Topo II β complex (PDB ID: 3QX3) as a template according to the previous study [122]. Afterward, the homology model and template were superimposed to identify the location and amino acid residues of etoposide binding site (Fig. S1 in supplementary data). The protonation states of all ionizable amino acids were determined at pH 7.0 using PROPKA 3.0 [105]. The starting structures of salvicine

(14690081), 1,4-BQ (895247), etoposide (3938684), and merbarone (17128283) were taken from ZINC database [145], whereas the MG and its 18 derivatives were built according to the previous research [24, 28] and fully optimized by the HF/6-31(d) level of theory using Gaussian09 program [103]. Subsequently, each of them was docked with 100 independent docking runs into three different pockets of Topo II α using CDOCKER module [104] in the Accelrys Discovery Studio 2.5^{Accelrys Inc.} and selective integrated tempering sampling based docking (SBD) approach [146]. Note that (i) the co-crystallized AMP-PNP (Fig. 11B), (ii) etoposide (Fig. 11C), and (iii) Mg²⁺ and TyrB805 (Fig. 11D) were defined as binding sites (CDOCKER: 15 Å of sphere radius and SBD: 22 x 18 x 20 Å of grid box) for ATPase domain, etoposide binding pocket, and central domain, respectively. According to the standard procedure [147-149], the electrostatic potential (ESP) charges around the optimized MG structures were computed using the same method and basis set. The antechamber and parmchk modules implemented in AMBER16 were used to generate the restrained ESP (RESP) charges and corresponding parameters of MGs, respectively. The AMBER ff14SB force field [109] was applied for the protein, whereas the ligands were treated by the generalized AMBER force field (GAFF) [110]. The missing hydrogen atoms were added by the LEaP module followed by minimization with 1000 steps of the steepest descents (SD) and continued by 2500 steps of conjugated gradient (CG) approaches on the hydrogen atoms only. Afterward, each system was solvated using TIP3P water model [113] in truncated octahedron periodic box with the minimum distance of 12 Å from the protein surface. The chloride ions were added for neutralizing the systems. The water molecules only were then minimized using the same SD and CG minimization processes. Lastly, the whole system was fully minimized using the same procedures.

3.3.2 Selective integrated tempering sampling (SITS) based docking

Selective integrated tempering sampling (SITS) is the technique that can selectively enhance the sampling of the solute without transforming the solvent structures [146]. This method combines the replica exchange with solute tempering

(REST) [150, 151] with integrated tempering enhanced sampling (ITS) simulations [152]. In case of REST, the system is divided into two parts: (i) the ligand (L) which is the central group and (ii) the water (W) which is the bath. Thus, the potential energy of the system (U) can be calculated using eq. 1,

$$U = E_L + E_{LW} + E_{WW} \quad (1)$$

where E_L , E_{LW} , and E_{WW} are the internal energy of the ligand, the interaction energy between the ligand and water, and the interaction energy among water molecules, respectively. In case of ITS, the potential energy of the system is shown in eq. 2 and the distribution function of such equation can be obtained by running MD simulations on a modified potential at the target temperature.

$$U_{eff} = -\frac{1}{\beta_0} \ln \sum_k n_k e^{-\beta_k U} \quad (2)$$

Where U_{eff} is the potential energy of system, $\beta_0 = 1/k_B T_0$ (where k_B is the Boltzmann constant and T_0 is the temperature), β_k represents a series of temperatures covering both low and high temperatures around T_0 , and n_k denotes the weighting factors. MG and its 18 derivatives including the reference compounds (salvicine, 1,4-BQ, etoposide, and merbarone) were solvated using octahedral box of TIP3P water model. Each aqueous system was subsequently minimized using the 50 steps of SD energy minimization, followed by 1000 steps of CG method. After that the MD simulations using time steps of 2 fs were performed with the temperature adjusted to 300 K for 200 ps by the Langevin dynamics with a friction coefficient of 5 ps^{-1} . All covalent bonds involving hydrogen atoms were constrained by the SHAKE algorithm [115]. The Particle Mesh Ewald method was used to treat long-range electrostatic interactions [114]. The pressure was adjusted to 1 atm by the Berendsen weak-coupling algorithm [153] with relaxation time constants of 0.2 ps in another 1 ns for equilibrating the system. Subsequently, the SITS simulations were applied for 100 ns using the maintained temperature at 300K and the effective potential for enhancing the sampling of MGs was

created using 60β values exponentially distributed from 220 to 720 K. Lastly, the generated conformations of MGs were then independently docked into the three different pockets of Topo II α using AutoDock Vina program [154].

3.3.3 Molecular dynamics (MD) simulations

The selected enzyme-ligand complexes from molecular docking were subsequently studied by MD simulations under periodic boundary condition with *NPT* ensemble using time steps of 2 fs according to previous works [155-157]. The Particle Mesh Ewald (PME) summation approach was applied to treat long-range electrostatic interactions [114], whereas the short-range cutoff for non-bonded interactions was set as 12 Å. Temperature and pressure were controlled by Berendsen weak coupling algorithm [153]. The SHAKE algorithm was used to constrain all covalent bonds involving hydrogen atoms [115]. The simulated models were heated up to 310 K for 100 ps and continuously held at this temperature for another 80 ns. The root-mean-square displacement (RMSD), hydrogen bond (H-bond) occupation, solvent accessible surface area (SASA), and principal component analysis (PCA) were calculated by the cpptraj module, whereas the MM/PB(GB)SA binding free energy and the per-residue decomposition energy were estimated by MM/PBSA.py implemented in AMBER16.

3.3.4 Free energy calculations based on MM/PBSA and MM/GBSA methods

The MM/PBSA and MM/GBSA approaches [116] were used to calculate the binding free energy (ΔG_{bind}), which is computed by the free energy difference between protein-ligand complex (G_{complex}) and the distinctive forms (G_{protein} and G_{ligand}) as shown in eq. 3,

$$\Delta G_{\text{bind}} = G_{\text{complex}} - (G_{\text{protein}} + G_{\text{ligand}}) \quad (3).$$

Each term is obtained from 100 MD snapshots extracted from the last 10 ns of the simulated model. ΔG_{bind} consists of the molecular mechanical energy in gas phase (ΔE_{MM}), solvation free energy (ΔG_{solv}), and entropy term (ΔS) as given in eq. 4,

$$\Delta G_{\text{bind}} = \Delta E_{\text{MM}} + \Delta G_{\text{solv}} - T\Delta S \quad (4).$$

The ΔE_{MM} is achieved from the combination of electrostatic (ΔE_{ele}) and van der Waal (ΔE_{vdW}) energies, whereas the ΔG_{solv} is calculated using eq. 5,

$$\Delta G_{\text{solv}} = \Delta G_{\text{solv}}^{\text{ele}} + \Delta G_{\text{solv}}^{\text{nonpolar}} \quad (5).$$

The $\Delta G_{\text{solv}}^{\text{ele}}$ can be estimated using either the Poisson-Boltzmann (PB) or the generalized Born (GB) models, whereas the $\Delta G_{\text{solv}}^{\text{nonpolar}}$ is calculated using solvent accessible surface area (SASA) [158] as shown in eq. 6,

$$\Delta G_{\text{solv}}^{\text{nonpolar}} = \gamma \text{SASA} + b \quad (6)$$

where γ and b are the experimental solvation parameters equal to $0.00542 \text{ kcal/mol} \cdot \text{\AA}^2$ and 0.92 kcal/mol , respectively [159]. Additionally, the contribution of each amino acid residue toward protein–ligand complex was evaluated using the per-residue decomposition free energy ($\Delta G_{\text{bind, residue}}$) based on MM/PBSA method.

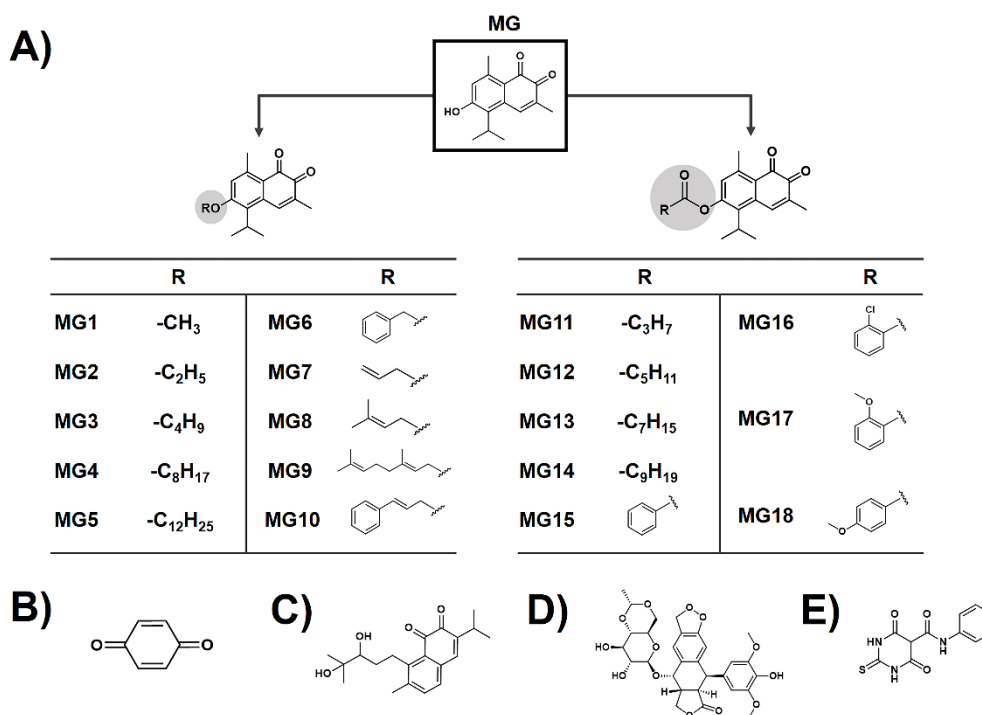


Figure 12 Chemical structures of (A) MG and its synthesized derivatives, which are ether derivatives (left panel) and ester derivatives (right panel), (B) 1,4-BQ, (C) salvicine, (D) etoposide, and (E) merbarone.

3.3 Results and discussion

3.3.1 Molecular docking

Both salvicine and 1,4-BQ were used as the reference compounds at the ATPase domain, whereas merbarone and etoposide were set as the reference compounds at the central domain and etoposide binding pocket, respectively. The docking results from both approaches are summarized in Fig. 13. The CDOCKER result showed that the entire series of MG specifically target to the ATPase domain rather than to the central domain and the etoposide binding pocket. Moreover, SITS-based docking (SBD) method exhibited the similar trend as CDOCKER, in which ATPase domain was likely to be the target site for MG analogs. These findings were correlated well with the previous reports described above [126, 136, 141]. Interestingly, for both docking techniques, all MG analogs exhibited the interaction energies significantly lower than

that of the potent 1,4-BQ, suggesting that these MG analogs might be the potent candidate compounds acting against the Topo II α ATPase domain. The six compounds from CDOCKER (MG4, MG5, MG12, MG13, MG14, and MG17) and two compounds from SBD (MG6 and MG15) with interaction energies lower than that of salvicine were then selected for MD simulations and binding free energy calculations.

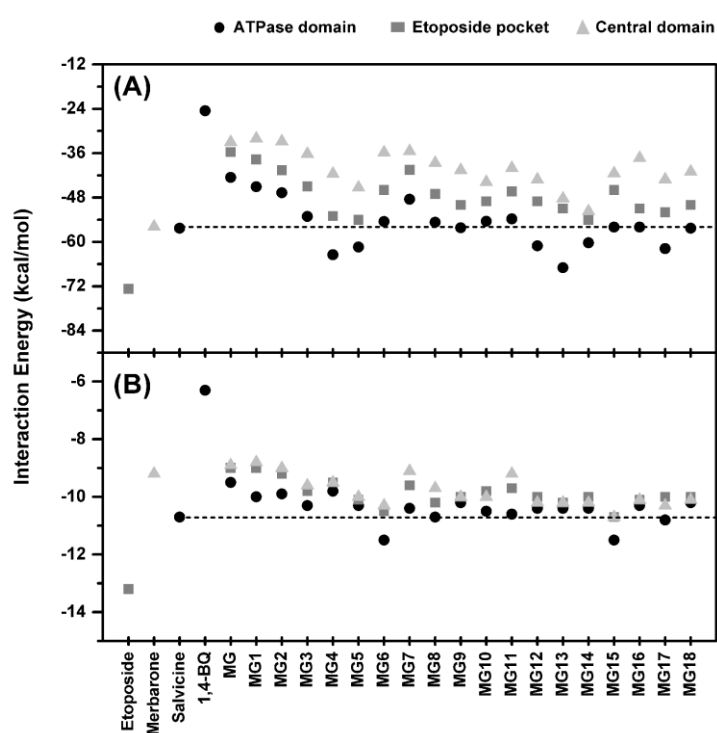


Figure 13 (A) CDOCKER and (B) SITS-based docking interaction energies (kcal/mol) of the etoposide, merbarone, salvicine, 1,4-BQ, and MG analogs binding at the three different domains of Topo II α .

3.3.2 System stability of simulated models

To evaluate the stability of MD systems, the root-mean-square displacement (RMSD) of complex (black), protein backbone (grey), and ligand (light grey) was computed relative to those of the starting structure (Fig. 14). The RMSD values of all complexes (black) continuously increased at the first 40 ns and maintained at a fluctuation of $\sim 2.75\text{--}3.50$ Å until the end of simulation time. The RMSD of MG12-Topo II

complex showed a high fluctuation during 20-40 ns and reached the equilibrium after 50 ns. The salvicine, MG4, MG6, MG12, MG15 and MG17 models exhibited the fluctuation of ~ 3 Å, while the other systems fluctuated more than 3 Å. Additionally, the backbone RMSDs (grey) showed the same fluctuation pattern with those of protein-ligand complex (black). Moreover, the RMSDs of all ligands except MG5 (light grey) were rather stable compared to their initial structures. The fluctuation pattern of MG5 was dramatically increased after 20 ns and reached the equilibrium at ~ 60 ns. These findings suggested that all systems reached the equilibrium at ~ 60 ns. In this study, the last 10 ns MD trajectories of each model were extracted for further analysis in terms of: (i) key residues for ligand binding, (ii) ligand-protein hydrogen bonding, (iii) solvent accessibility at the ATP-binding pocket along the 80 ns simulations, (iv) binding free energy prediction for ligand-protein complex, (v) protein secondary structure analysis, and (vi) principal component analysis (PCA).

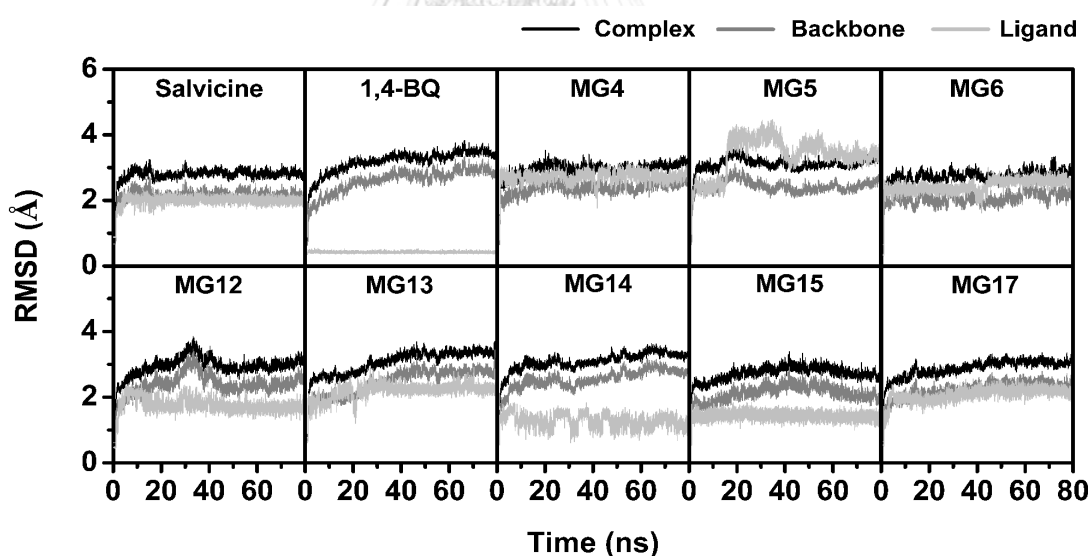


Figure 14 RMSD plot for complex (black), backbone (grey), and ligand (light grey) of the 10 simulated complexes.

3.3.3 Key residues for ligand binding

In order to evaluate the key binding residues involved in ligand binding within ATP-binding pocket located at ATPase domain of Topo II α , the per-residue decomposition free energy ($\Delta G_{\text{bind, residue}}$) calculation based on the MM/PBSA method was performed. The total contribution of each amino acid for ligand binding of all complexes are plotted in Fig. 3.5, where the negative and positive decomposition free energy values represent the ligand stabilization and destabilization, respectively. Note that among residues 29-405 in chain A of Topo II α , only contribution from the 50-250 residues are shown. Fig. 3.5 revealed that there are twenty-two amino acid residues (87-88, 91-92, 94-95, 98-99, 125, 141-142, 147, 150, 161-162, 164-168, 215, and 217) associated with ligand binding for all simulated models. The binding orientation of reference compounds and MGs inside ATP-binding pocket is displayed in Fig. 3.6. Moreover, the energy stabilization from those important twenty-two residues was separately considered in terms of the contribution from backbone (light grey bar) and sidechain (grey bar) coupled with the electrostatic ($\Delta E_{\text{ele}} + \Delta G_{\text{polar}}$, light grey line) and vdW ($\Delta E_{\text{vdW}} + \Delta G_{\text{nonpolar}}$, black line) energies (Fig. S2 in supplementary data).

The hydrophobic residues I125, I141, F142 inside the ATPase domain of Topo II α exhibited the energy stabilization of ≤ -1.0 kcal/mol for most systems (Fig. 15-16). Due to the small geometry of 1,4-BQ, there are only two amino acid residues (I141 and Y165) involved in ligand stabilization, while the importance of I141 was found from the previous docking study [136]. This might imply that I141 is a recognized residue for 1,4-BQ binding through vdW interaction. In case of salvicine, most contributing amino acids were hydrophobic residues in a good agreement with the previous report by which salvicine was hydrophobically stabilized inside this pocket [126]. Interestingly, MG12, MG14, and MG15 exhibited the greater binding strength than that of salvicine and 1,4-BQ. For MG12, the residues N91 and K168 showed the strong binding affinity with $\Delta G_{\text{bind, residue}}$ of -3.59 kcal/mol (dark blue) and -3.20 kcal/mol (blue), respectively. By contrast, the residue R98 exhibited the highest stabilization for MG14 (-5.87 kcal/mol,

magenta) and MG15 (-4.65 kcal/mol, purple) systems. Among twenty-two amino acids at the ATP-binding pocket, most residues tend to stabilize the ligands through side chain interactions rather than those of the backbone (Fig. S2). The main energy contribution for stabilizing the ligands was vdW energy (up to ~ -3.00 Å), especially for N91, I125, I141, F142, A167, T215, and I217 residues; whereas the electrostatic energy was observed in the range of -5.03 to 4.00 kcal/mol. Interestingly, the residue R98 of MG14 (Fig. 16H, magenta) exhibited a strong electrostatic contribution (-5.03 kcal/mol) with the carbonyl group of naphthoquinone-ring (NQ-ring), resulting in the strongest binding affinity compared with the other MGs. These results are correlated well with the predicted binding free energies for ligand/Topo II α complexes as discussed later.

The major contributing residues can be divided into three regions: (i) the consensus motif GXXGXG: residues 161 to 166; (ii) the magnesium-binding area: residues 87, 91, and 94; and (iii) the hydrophobic cavity: residues 125, 141, 142, and 215 [160]. In case of salvicine, 1,4-BQ, MG6, MG14, and MG15, the NQ-ring was encapsulated inside the hydrophobic cavity; whereas the aliphatic side chains of MG4, MG12, and MG13 were occupied within this region instead. However, both NQ-ring and alkyl group of MG5 were not encapsulated inside this cavity (Fig. 16D). These binding patterns can be summarized as following: (i) non-substituted aromatic ring and small substituents: NQ-ring was preferentially embedded into the hydrophobic cavity, (ii) aliphatic side chain ranged from C6 to C8 or a substituted aromatic ring: NQ-ring was flipped out of this cavity due to the enhancement of hydrophobicity of alkyl group, (iii) the C-10 length (MG14, Fig. 16H) promoted a suitable orientation by which the carbonyl group of ester bond and NQ-ring strongly interacted with Mg²⁺ (2.15 ± 0.06 Å) and the NH1 guanidinium nitrogen of R98 residue (2.96 ± 0.21 Å), respectively; as well as the NQ ring was re-encapsulated into hydrophobic cavity, and (iv) the C-12 length may cause the steric effect inside hydrophobic chamber.

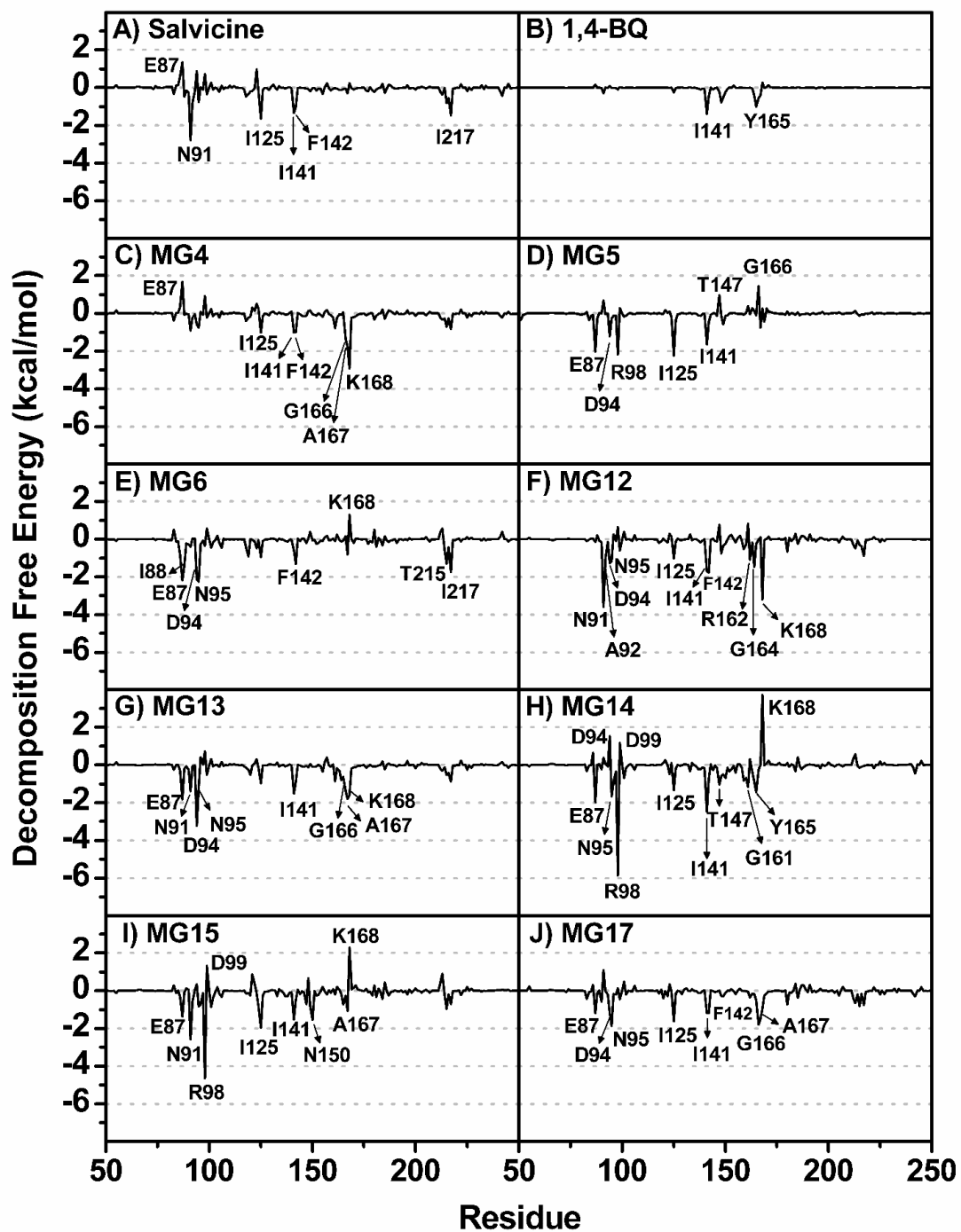


Figure 15 Per-residue decomposition free energy ($\Delta G_{\text{bind, residue}}$) of the ATPase domain of Topo II α for the binding of the two reference compounds (salvicine and 1,4-BQ) and eight selected MG analogs.

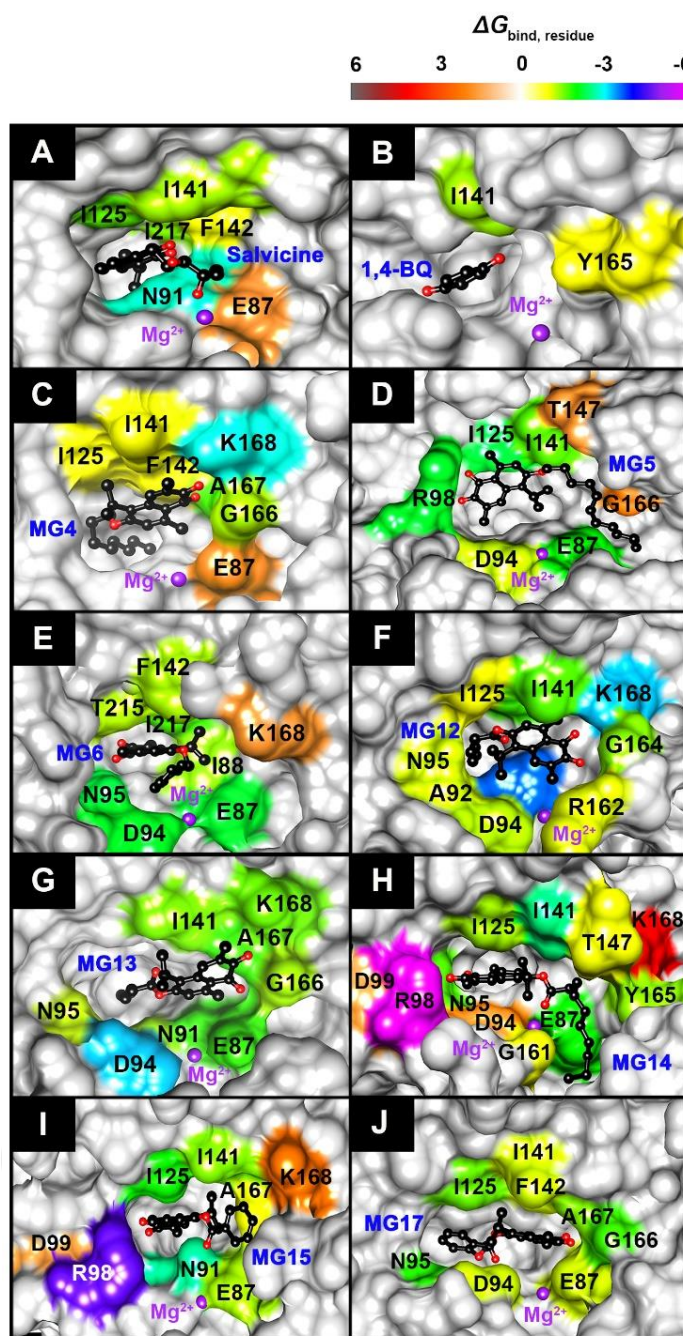


Figure 16 The binding orientation of (A) salvicine, (B) 1,4-BQ, (C) MG4, (D) MG5, (E) MG6, (F) MG12, (G) MG13, (H) MG14, (I) MG15, and (J) MG17 inside ATP-binding pocket drawn from the last MD snapshot. The amino acids involved in ligand binding are shaded according to the per-residue decomposition free energy ($\Delta G_{\text{bind, residue}}$ (kcal/mol)) in Fig. 5, in which the highest and lowest energies are ranged from dark brown to magenta, respectively.

3.3.4 Ligand-protein hydrogen bonding

Hydrogen bond formation is one of the important factors that can determine the binding strength of protein-ligand complex. Therefore, the intermolecular hydrogen bond interactions were calculated using the two criteria as following: (i) distance between hydrogen donor (HD) and acceptor (HA) $\leq 3.5 \text{ \AA}$, and (ii) the angle of HD-H \cdots HA $\geq 120^\circ$. The percentages of hydrogen bond occupations for all 10 studied systems are plotted and compared in Fig. 17. As expected, low hydrogen bond formation between the hydrophobic ligands and the surrounding residues located in the ATP binding pocket of Topo II α was observed in all complexes. Two strong hydrogen bonds ($> 70\%$ occupancy) with N91 and N120 were found to stabilize the MG15 binding. Salvicine and the five MGs (MG4, MG12, MG14, and MG17) exhibited only one strong hydrogen bond interaction, while hydrogen bond formation was occurred moderately for MG13. By contrast, the relatively low or no hydrogen bond interaction was observed in the other systems. The obtained results suggested that in this study the intermolecular hydrogen bond interactions did not play a role for stabilizing the protein-ligand complex, since the chemical structures of MG analogs contain many carbon atoms and/or aromatic moieties, resulting in high hydrophobicity. On the other hand, the ligand binding was predominantly contributed by vdW interactions as described previously.

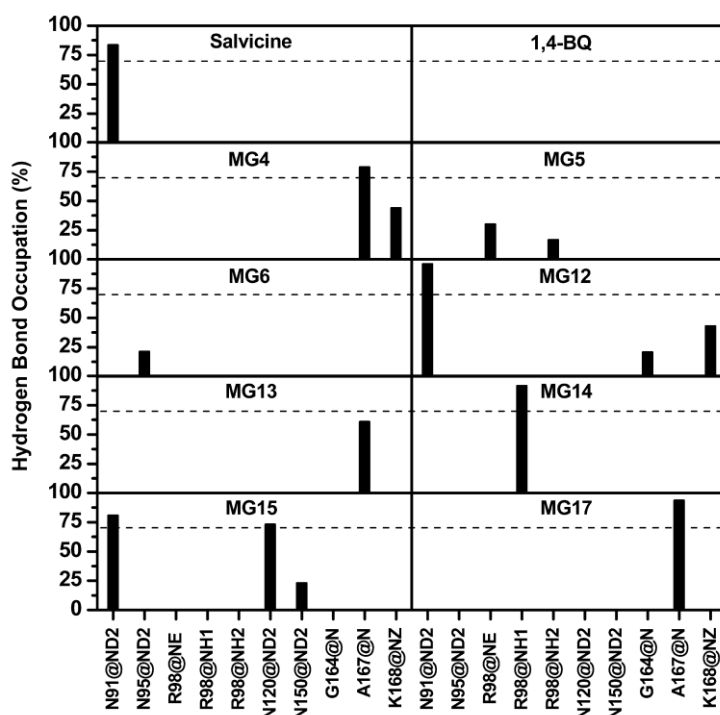


Figure 17 The percentage of H-bond occupation of the amino acid residues within ATP-binding pocket contributing to all ligands during the last 10 ns simulation.

3.3.5 Solvent accessibility at the ATP-binding pocket

To investigate the effect of solvent accessibility toward the ATP-binding pocket in both chain A and chain B (Fig. 18A), the solvent accessible surface area (SASA) calculation on the amino acid residues within a 5-Å sphere of each ligand was performed (Fig. 18B). The results are summarized in Fig. 18C. The SASAs of ATP-binding pocket without ligand binding in chain B (red) were observed in the range of $\sim 200\text{-}1000 \text{ \AA}^2$, whereas those with the ligand binding in chain A (green) mostly showed a significant decrease in the water accessibility except for the complexes of 1,4-BQ, MG5 and MG6. In such three cases, the SASAs of chain A continuously increased and retained values at $\sim 500\text{-}1000 \text{ \AA}^2$. Moreover, the SASA of MG5 was totally overlapped with chain B after 50 ns. Accordingly, the huge accessibility of water molecules could affect the ligand binding affinity by interfering the vdW interactions between ligand and

protein receptor. In case of salvicine and MG4, the SASA values exhibited the similar pattern observed in the range of 0-800 Å² and the patterns of SASA were moderately stable at ~400 Å². Whereas, the SASAs of MG13 and MG17 were higher than that of chain B (~900 Å²) at some points of simulation time and retained values at ~200-400 Å². Interestingly, the SASAs of MG12, MG14, and MG15 were satisfactorily stable at ~200 Å², from which it can be concluded that these MG analogs fitted well within ATP-binding pocket, resulting in the lower water accessibility than that of the others. These results are correlated well with the MM/PB(GB)SA calculations, where MG12, MG14, and MG15 exhibited the great binding affinity compared with the other MG analogs.

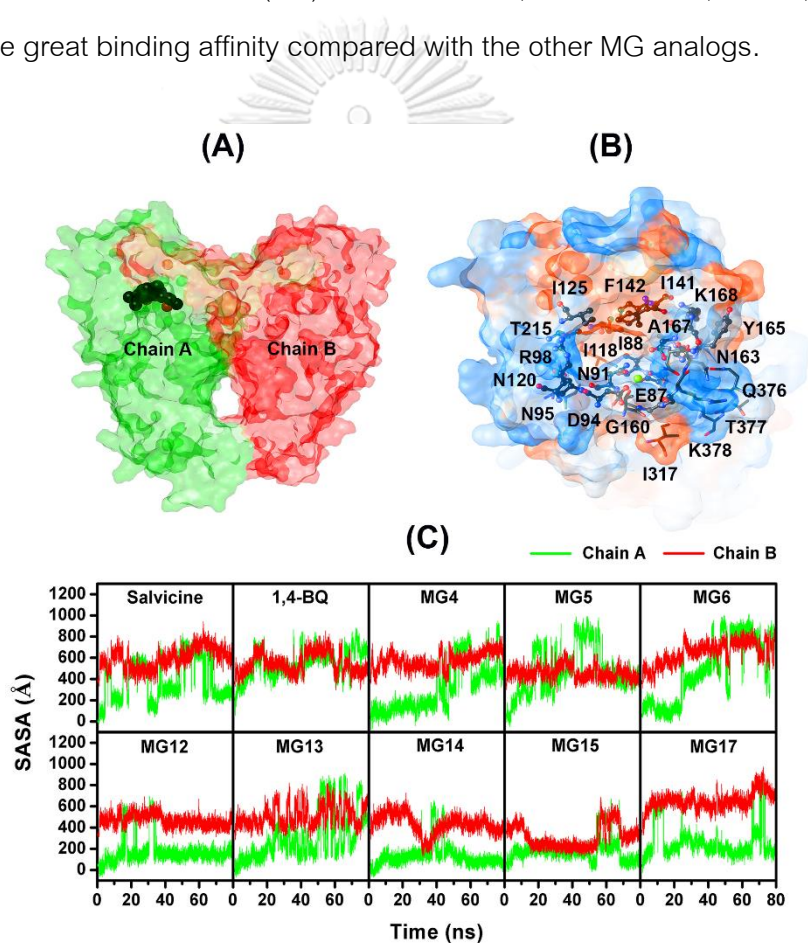


Figure 18 (A) The two chains of Topo II α ATPase domain, in which chain A and chain B are shaded by green and red colors, respectively. (B) The amino acids within a 5-Å sphere around ligands used for SASA calculations where the results are plotted in (C).

3.3.6 Binding free energy prediction for ligand-protein complex

In this study, MM/PBSA and MM/GBSA methods [161-164] were applied to predict the binding free energy of all focused ligand-Topo II α complexes in aqueous solution using 100 MD snapshots from the last 10 ns simulation. The binding free energy (ΔG_{bind}) including entropy term (estimated from 10 MD snapshots) as well as electrostatic and vdW interaction energies (ΔE_{ele} and ΔE_{vdW}) are summarized in Fig. 19, where the experimental ΔG_{bind} of 1,4-BQ converted from IC₅₀ value of $8.58 \pm 0.8 \mu\text{M}$ [136] are shown by asterisk for comparison. Note that the Mg²⁺ ion was included in the protein part for binding free energy calculations.

The molecular mechanical energy in gas phase revealed that vdW energy was the main force for stabilizing the ligand binding to Topo II α (Fig. 19A), in a correspondence with the hydrophobic (+)-rutamarin bound to the Topo II α ATPase domain at ATP-binding pocket [160]. On the other hand, the electrostatic interactions become important for N-fused imidazole in complex with this target because of the negatively charged group in its chemical structure [165]. Interestingly, both MM/PBSA and MM/GBSA approaches gave the similar trend of binding free energies in which MM/PBSA method could predict the binding free energy value of the potent compound against the ATPase domain of Topo II α (1,4-BQ with ΔG_{bind} of -6.20 kcal/mol) closer to the experimental data ($\Delta G_{\text{bind, experiment}}$ of -7.18 kcal/mol [136]). Thus, the ΔG_{bind} values based on this method were chosen for further discussion. Among the focused eight MGs, there are three compounds from ester derivatives MG14, MG12 and MG15 (-28.20, -25.30 and -21.30 kcal/mol) that showed the relatively lower binding free energies than that of the known ATP-competitive inhibitor, salvicine (-16.50 kcal/mol), while MG4 which is the only one analog in ether derivatives exhibited the binding strength (-16.90 kcal/mol) in the range of salvicine. These three ester derivatives exhibited the greater binding affinity toward Topo II α than that of ether derivatives because the two oxygen atoms of ester bond acting as hydrogen bond acceptors could form the hydrogen bond interactions with the residues N91, G164, and K168 for MG12; R98 for MG14; and N91,

N120, and N150 for MG15. Besides, the non-substituted aromatic ring (MG15) exhibited the greater binding strength than that of *para*-substituted (MG17) and ether connected benzene ring (MG6). Taken together, all MG analogs showed lower binding free energies than that of the potent 1,4-BQ, while either ester or ether derivatives of MG with a higher binding affinity than that of salvicine (MG12, MG13, MG14 and MG15) or in the range of salvicine (MG4 and MG13) are useful as rational guide for synthetic and medicinal chemists who focus on the development of new anticancer drugs against Topo II α . It should be noted that our computational results were suggestive, therefore the Topo II α enzymatic assay need to be performed in order to confirm our findings.

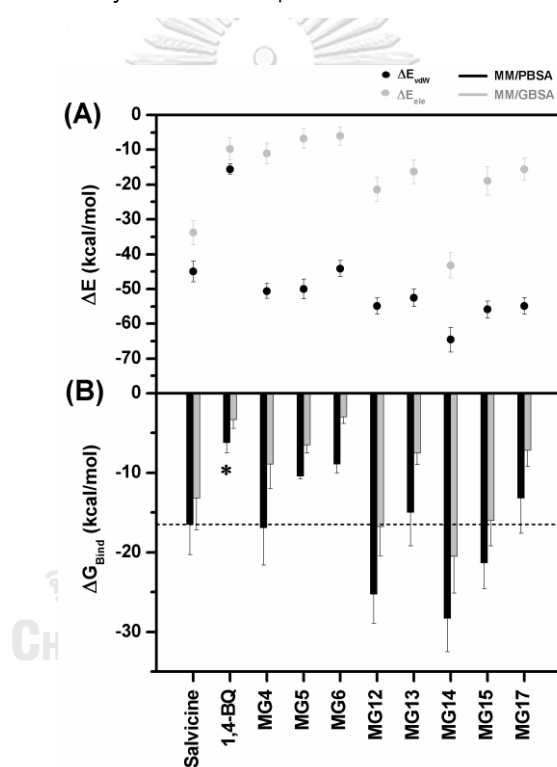


Figure 19 (A) The molecular mechanical energy in gas phase in terms of electrostatic and vdW interactions (ΔE_{elc} and (ΔE_{vdW}) and (B) MM/PB(GB)SA binding free energy, while the asterisk symbol indicates the $\Delta G_{bind, experiment}$ of 1,4-BQ (-7.18 kcal/ mol) calculated by the equation of $\Delta G_{bind, experiment} = RT \ln IC_{50}$, where R is the gas constant (8.31451 Jmol⁻¹K⁻¹), T is the experimental temperature (310K), and IC_{50} is the half maximal inhibitory concentration for ATPase activity ($8.58 \pm 0.8 \mu M$) [136].

3.3.7 Protein structure

The ligand binding at the ATP-binding site of Topo II α may affect the protein conformation. To observe such conformational change upon complexation, the timeline secondary structure calculation implemented in Visual Molecular Dynamics (VMD) software [166] was applied on 100 MD snapshots extracted from every 1 ns simulation. The protein secondary structure of the most potent MG14/Topo II α complex is plotted in Fig. 20, in which the ATP-binding pocket residues 75-225 are shown in the black box. The results of the other systems are shown in Fig. S3 in supplementary data.

The timeline calculations revealed that the ligand binding in chain A strongly promoted the 3-10 helix structures (dark blue) at residues 47-49 located outside the ATP-binding pocket for all systems except 1,4-BQ and MG17. The binding of the most predicted potent compound MG14 somewhat affected the secondary structure of Topo II α at the ATP-binding pocket residues 85-98 by changing from 3-10 helix structures into the more favorable alpha helix (pink). Additionally, the population of 3-10 helix structures within the turn region at residues 153-155 was enhanced. Interestingly, the MG14 binding induced the conformational change of Ser149 to extend the turn structure (residues 145-151, cyan focused by black dot circle in Fig. 20B) which moved closer toward the ligand (distance between centers of mass of these residues and Mg²⁺ of 9.9 ± 0.2 Å), whereas this turn structure in chain B was far from Mg²⁺ (13.3 ± 0.3 Å).

Principal component analysis (PCA) is a multivariate statistical approach that extracts the most important elements from the data using a covariance matrix which herein derived from atomic coordinates that describe the accessible degree of freedom of the protein [167]. Thus, this method can be used to describe both direction of motion and its amplitude in many biological macromolecules including proteins. To characterize the motion of entire protein as well as the turn region (residues 145- 151) motions in both holo form and apo form, PCA was performed on the last 10 ns MD trajectories of MG14/Topo II α complex. The results are shown in Fig. 21. The first principal component

(PC1, 12.58%) revealed that the MG14 binding promoted the motion of turn region to approach to ligand, whereas this region in chain B was flipped away from Mg^{2+} (Fig. 21A) supported by the distance between turn structure and Mg^{2+} described above. It can be implied that this event might be one of the crucial mechanisms of inhibition for naphthoquinone-containing compounds against ATPase domain of Topo II α . Moreover, the 2D projection of MD trajectories on the first two PCs acquired from diagonalizing the covariance matrix of atomic fluctuation (Fig. 21B) revealed that PC1 had two main conformational distributions, whereas one population was observed in PC2. The first twenty PC modes showed the 57.85% of accumulated variance (Fig. 21C) and the first two PC modes (PC1, 12.58% and PC2, 6.17%) can represent the crucial motions of MG14/Topo II α complex.

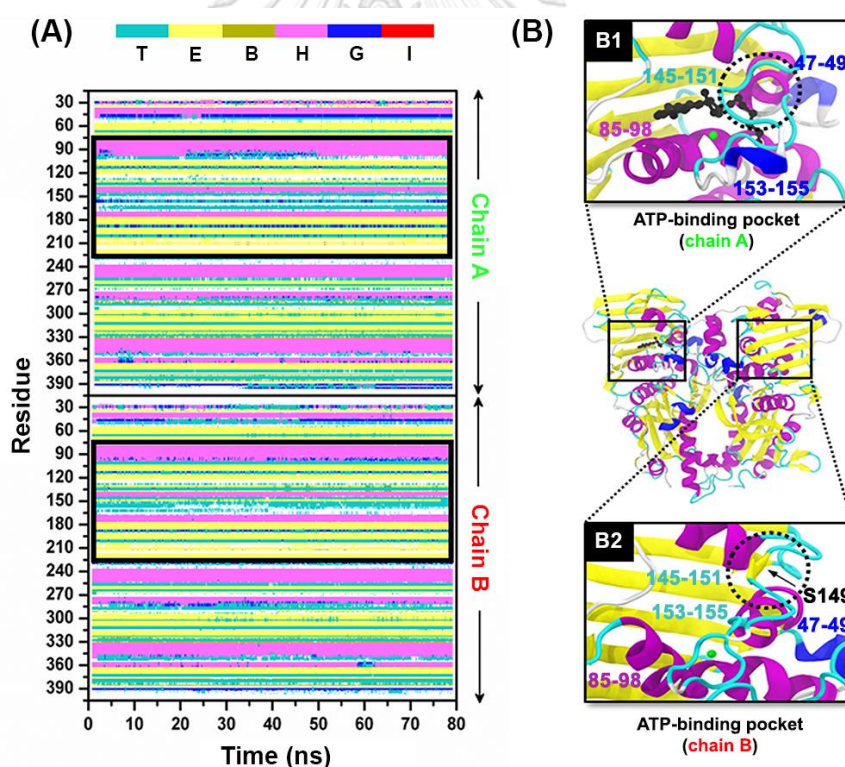


Figure 20 (A) The timeline secondary structures of MG14 system, (B) 3D representation of MG14-Topo II α complex shaded by secondary structure color using VMD program where the ATP-binding pocket is shown in black box. B1 and B2 represents the ATP-binding pocket of chain A and chain B, respectively. The secondary structure plot is

represented by six colors for turn (T: cyan), extended configuration (E: yellow), isolated bridge (B: olive green), alpha helix (H: pink), 3-10 helix (G: dark blue), and pi-helix (I: red).

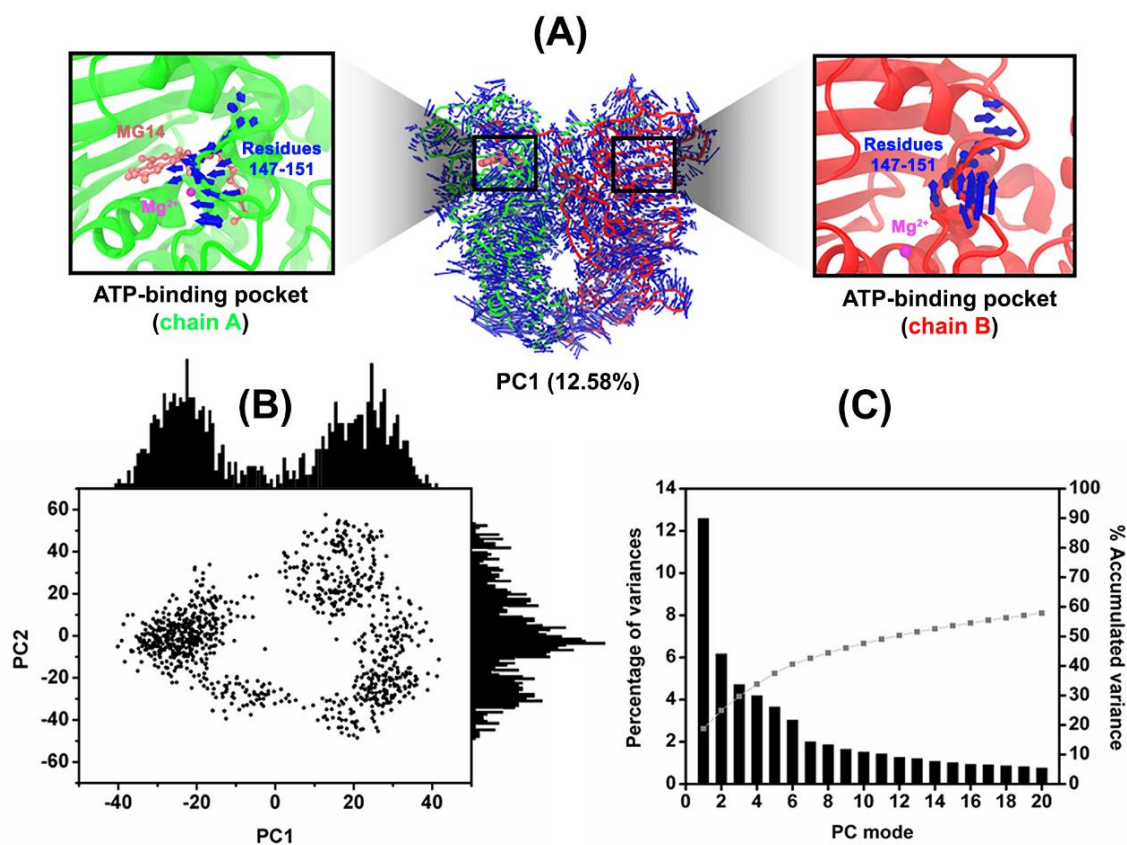


Figure 21 (A) Porcupine plot of MG14/Topo II α complex showing the significant motion, especially turn region (residues 145-151) across the first PC in the holo form (left panel) and apo form (right panel), in which head of the arrow indicates the direction of motion, while its length indicates the amplitude of motion. (B) The 2D projection of MD trajectories on the first two PCs. (C) PCA scree plot of quantitative characters.

3.5 Conclusions

In the present study, the main bioactive MG extracted from *Mansonia gagei* and its semi-synthetic compounds were selected to study the preferential binding site and dynamics behavior as well as to predict the inhibitory activity against Topo II α using molecular modeling techniques. The two molecular docking approaches suggested that MG derivatives preferentially target to the ATPase domain rather than to the etoposide pocket and the central domain. The eight potent MGs with higher binding affinities than that of salvicine, an ATP-competitive inhibitor, were selected for MD simulations and binding free energy calculations based on MM/PB(GB)SA methods. According to per-residue decomposition free energy analysis, the residues 87-88, 91-92, 94-95, 98-99, 125, 141-142, 147, 150, 161-162, 164-168, 215, and 217 were associated with ligand binding, by which van der Waals interactions mainly contributed for protein-ligand complexation rather than electrostatic forces and H-bond formations. Both MM/PB(GB)SA binding free energies showed that MG12, MG14, and MG15 exhibited the greater binding affinities with low solvent accessibility than those of salvicine and 1,4-BQ. Accordingly, the C-6 to C-10 lengths were suitable for aliphatic carbon sidechain of MG, whereas the C-12 length might cause the steric effect within ATP-binding pocket. Moreover, the ligand binding affected the secondary structures of Topo II α for both inside and outside ATP-binding pocket. Especially, the binding of the most predicted potent compound MG14 promoted the conformational change of the turn structure (residues 145-151 of chain A) to become significantly located closer to the ligand and Mg²⁺. Thus, this occurrence could be one of the crucial mechanisms underlying Topo II α inhibition for this naphthoquinone-containing compound against ATPase domain of Topo II α . Taken together, these theoretical calculations can provide useful structural information in terms of: (i) the suitable length of carbon sidechain and/or aromatic moiety for the predictably potent MGs, (ii) binding orientation of ligands, and (iii) key amino acids involved in ligand binding, for further design and development of new targeted drugs containing naphthoquinone core against Topo II α .

CHAPTER IV

ENHANCED SOLUBILITY, STABILITY, AND ANTICANCER ACTIVITY OF
MANSONONE G/BETA-CYCLODEXTRINS INCLUSION COMPLEXES

Inclusion complexes of mansonone G with β -cyclodextrins: Molecular modeling, phase solubility, characterization, and cytotoxicity

Panupong Mahalapbutr^a, Piyanuch Wonganan^{b*}, Thanapon Charoenwongpaiboon^c,
Warinthorn Chavasiri^d, Manchumas Prousoontorn^c, Thanyada Rungrotmongkol^{a,e,f*}

^aStructural and Computational Biology Research Unit, Department of Biochemistry, Faculty of Science, Chulalongkorn University, Bangkok 10330, Thailand

^bDepartment of Pharmacology, Faculty of Medicine, Chulalongkorn University, Bangkok 10330, Thailand

^cStarch and Cyclodextrin Research Unit, Department of Biochemistry, Faculty of Science, Chulalongkorn University, Bangkok 10330, Thailand

^dCenter of Excellence in Natural Products Chemistry, Department of Chemistry, Faculty of Science, Chulalongkorn University, Bangkok 10330, Thailand

^ePh.D. Program in Bioinformatics and Computational Biology, Faculty of Science, Chulalongkorn University, Bangkok 10330, Thailand

^fMolecular Sensory Science Center, Faculty of Science, Chulalongkorn University, Bangkok 10330, Thailand

This article is in preparation for publication (2019)

4.1 Abstract

Mansonone G (MG), a plant-derived compound isolated from the heartwood of *Mansonia gagei*, possesses a potent antitumor effect on several kinds of malignancy. However, its poor solubility limits its use for practical applications. Beta-cyclodextrin (β CD), a cyclic oligosaccharide composed of seven (1 \rightarrow 4)-linked α -D-glucopyranose units, is capable of encapsulating a variety of poorly soluble compounds into its hydrophobic interior. In this work, we aimed to enhance the water solubility and the anticancer activity of MG by complexation with β CD and its derivatives (e.g., 2,6-di-O-methyl- β CD (DM β CD) and hydroxypropyl- β CD). The 90-ns molecular dynamics simulations and MM/GBSA-based free energy results suggested that DM β CD was the most preferential host molecule for MG, as supported by (i) the lowest water accessibility toward MG atomic radii and (ii) the highest stability constant (K_c of 2245.26 M^{-1}) obtained from experimental phase solubility study. The encapsulation of MG into β CD's cavity resulted in the reduced flexibility of β CD through the enhancement of intramolecular H-bond formations on the wider rim. The inclusion complex formation between MG and β CD(s) was confirmed by DSC and SEM techniques. Notably, the MG/DM β CD (IC_{50} of 13.45 μ M) and MG/ β CD (IC_{50} of 17.63 μ M) inclusion complexes exerted a significantly higher cytotoxic effect on A549 lung cancer cell than that of the uncomplexed MG (IC_{50} of 42.86 μ M).

4.2 Introduction

Cancer is a major public health issue and ranks the second leading cause of mortality worldwide following cardiovascular diseases [168]. Several plant-derived compounds containing naphthoquinone (NQ) moiety such as beta-lapachone, plumbagin, and shikonin have been reported to exert a superior antiproliferative activity [79, 169, 170]. Mansonones, a group of *ortho*-NQ-containing compounds, are the major bioactive constituent of the diverse plant genera such as *Mansonia*, *Hibiscus*, and *Thespesia* [26]. Previous studies revealed that mansonones D, E, F, and H possess the anticancer effect on several kinds of solid tumor [171-173]. In addition, the novel

derivative of mansonone F exhibited 20-fold stronger DNA topoisomerase II inhibitory activity than that of the chemotherapeutic drug etoposide [174].

Among the eight different mansonones (e.g., mansonones A-H) [175], mansonone G (MG, Fig. 22A) is the major product isolated from the heartwood of *Mansonia gagei* Drumm., Sterculiaceae family found in Thailand [24]. Many lines of evidence have shown that MG exhibits the potent anticarcinogenic effect on various types of malignancy, e.g., ovarian (A278, IC_{50} of 10.2 μ M), colorectal (HCT116, IC_{50} of 63.4 μ M), liver (HepG2, IC_{50} of 36.3 μ M and Huh-7, IC_{50} of 25.9 μ M), breast (MCF-7, IC_{50} of 23.0 μ M), and cervical (HeLa, IC_{50} of 18.8 μ M) cancer cell lines [25-27]. Moreover, MG has been documented to significantly inhibit the activity of P-glycoprotein efflux pump [26]. Even though MG could serve as a promising anticancer agent, its poor water solubility leads to a limited use for pharmaceutical and medicinal purposes.

Cyclodextrin (CD), a naturally occurring cyclic oligosaccharide that is produced by CD glucanotransferase (CGTase)-catalyzed starch degradation [176], has a unique structure representing a hydrophobic inner cavity and a hydrophilic outer surface. Consequently, CD can potentially enhance the solubility, stability, and pharmacological properties of many lipophilic guest molecules [177, 178] through the formation of an inclusion complex driven mainly by van der Waals (vdW) interactions [179]. The common types of CD are alpha (α), beta (β), and gamma (γ) CDs formed by six, seven, and eight α -D-glucose subunits, respectively. Among the three CDs, β CD (Fig. 22B) is the most commonly used in many pharmaceutical purposes due to its low price, easy synthetic access, and structural orientation suitable for inclusion complex generation [29, 180]. However, the low water solubility (18.5 mg/mL at 25°C) and nephrotoxicity of β CD limit its use for practical applications [36].

In recent years, the use of β CD derivatives (e.g., methylated (M) and 2-hydroxypropylated (HP) β CDs) for host-guest encapsulation has gained much attention in an attempt to improve the water solubility and to reduce the limitations of natural β CD. The M β CD (e.g., 2,6-di-O-methyl- β CD; DM β CD) and the HP β CD derivatives exhibit the higher aqueous solubility and lower toxicity than the unmodified β CD [36, 181, 182].

Several experimental and theoretical reports have demonstrated that the water solubility, chemical stability, and anticancer activity of poorly soluble molecules are significantly improved by complexation with DM β CD and HP β CD derivatives [183-185]. However, the information on the inclusion complexes of MG with β CDs has never been reported.

In the present work, we aimed to improve the water solubility and the anticancer activity of MG using β CD and its derivatives, e.g., DM β CD and HP β CD, based on working hypothesis that the anticancer activity of MG may be positively affected by the influence of β CDs. Firstly, the computational tools were applied (i) to search for the suitable β CD encapsulating molecule for MG and (ii) to investigate the atomistic insights into host-guest complexation and its underlying interactions. Subsequently, the experimental phase solubility was verified. The spectroscopic techniques were then used to confirm the formation of MG/ β CDs. Finally, the inclusion complexes were subjected to evaluate the antitumor activity toward A549 human lung cancer cell line.

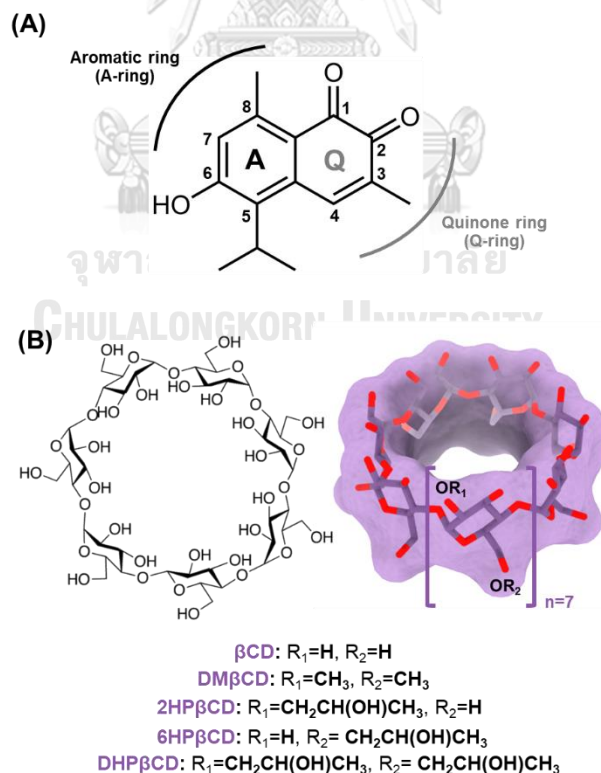


Figure 22 (A) 2D structure of MG. (B) 2D- and 3D structures of β CD, where the functional substitutions used in this study are shown below.

4.3 Material and methods

4.3.1 Computational details

The geometry of MG was constructed and fully optimized at the HF/6-31(d) level of theory using Gaussian09 program [186], whereas the 3D structures of all investigated β CD analogs (e.g., β CD, DM β CD, 2HP β CD, 6HP β CD, and DHP β CD) were taken from previous study [112]. It should be noted that, the commercially available HP β CD is a mixture of various degrees of substitution, while the models we built in this study were fully (DHP β CD) and partially (2-HP β CD and 6-HP β CD) substituted HP β CDs. The inclusion complexes were generated in Accelrys Discovery Studio 2.5 (Accelrys, Inc.). The required parameters of MG were created as per the standard procedures [102, 111, 187]. The Glycam-06 [188] and general AMBER force fields [110] were applied on β CDs and MG, respectively. Using a truncated octahedral box, the TIP3P water molecules were solvated around MG/ β CDs complexes with a spacing distance of 15 Å. After that, the added water molecules were minimized using 1000 steps of steepest descents and continued by 3000 steps of conjugated gradient. Lastly, the whole model was optimized as per the same methods.

Each solvated inclusion complex was heated up from 10K to 303K for 60 ps, and followed by all-atom molecular dynamics (MD) simulations (*NPT* ensemble, temperature of 303K, pressure of 1 atm, and time step of 2 fs) using AMBER16 for 90 ns. All chemical bonds involving hydrogen were constrained using SHAKE algorithm [115]. The particle mesh Ewald method [189] was employed to treat charge-charge interactions with the cutoff of 12 Å. The MM/GBSA-based binding free energy ($\Delta G_{\text{bind, MM/GBSA}}$) calculations [116] was used to estimate the binding affinity of all studied inclusion complexes.

4.3.2 Experimental part

4.3.2.1 Chemical reagents

MG was extracted from *Mansonia gagei* Drumm according to the previous study [24]. β CD, DM β CD (Heptakis), HP β CD, dimethyl sulfoxide (DMSO), and 3-(4,5-dimethylthiazol-2-yl)-2,5-diphenyltetrazolium bromide (MTT) were from Sigma-Aldrich (St. Louis, MO, USA).

4.3.2.2 Chemical reagents

A549 human lung cancer cell line was obtained from Dr. Apiwat Mutirangura (Chulalongkorn University, Thailand). A549 cells were cultured in Dulbecco's modified Eagle's medium (DMEM; Gibco, Grand Island, NY, USA) containing 10% fetal bovine serum (FBS; Gibco), 100 U/ml penicillin, and 100 µg/ml streptomycin (Gibco) and were maintained at 37°C in a humidified 5% CO₂ atmosphere.

4.3.2.3 Phase solubility study and evaluation of thermodynamic parameters

Phase solubility study was conducted following the method of Higushi and Connors [190]. Briefly, an excess amount of MG was added to βCD(s) solutions (0-10 mM). The mixtures were shaken (250 rpm) at 30, 37, and 45°C for 72 hours. Subsequently, the product solutions were obtained by centrifugation at 12,000 rpm for 15 minutes. The solubility of MG was characterized by measuring the absorbance at a wavelength of 415 nm. The eq. 1 was used to calculate the apparent stability constant (K_c), where S_0 is y-intercept.

$$K_c = \frac{\text{Slope}}{[S_0(1-\text{slope})]} \quad (1)$$

The Van't Hoff plot based on eq. 2 [178] was used to identify the thermodynamic properties, including enthalpy (ΔH) and entropy (ΔS) changes of inclusion complexation, whilst the experimental Gibbs free energy ($\Delta G_{\text{bind, exp}}$) was obtained from eq. 3.

$$\ln K_c = -\frac{\Delta H}{RT} + \frac{\Delta S}{R} \quad (2)$$

$$\Delta G_{\text{bind, exp}} = \Delta H - T\Delta S \quad (3)$$

4.3.2.4 Inclusion complex preparation

A 1:1 stoichiometric ratio of MG/βCD(s) inclusion complex was prepared by freeze-drying method. Each accurately weighed compound was dissolved in distilled water (30 mL), then the mixture was magnetically stirred at room temperature for 24 h. After that, the solution was centrifuged (12,000 rpm for 15 minutes) and filtered through a 0.45 µm filter. The obtained solution then was frozen overnight at -80°C and

subsequently lyophilized using LYO-LAB, Lyophilization Systems, Inc USA for 3 days. The resulting freeze-dried powders were stored in desiccator for further use.

4.3.2.5 Differential scanning calorimetry (DSC)

The thermal behavior of the MG, β CD, DM β CD, MG/ β CD, and MG/DM β CD was characterized using NETZSCH DSC 204F1 Phoenix. Each solid sample (\sim 1-2 mg) was heated from 25°C to 300°C in aluminum pans at a rate of 10°C/min.

4.3.2.6 Scanning electron microscope (SEM)

The surface morphology of MG, β CD, DM β CD, and the freeze-dried inclusion complexes was analyzed using SEM technique. Samples were coated with a thin layer of gold in vacuum before viewing under 300 times magnification. Observations were performed using an accelerating voltage of 10 kV.

4.3.2.7 Cytotoxicity of MG toward lung cancer cells

Cell viability was evaluated using MTT assay. A549 cells were seeded into 96-well plates at a density of 3×10^3 cells/well. After overnight incubation, cells were treated with logarithmic concentrations (1, 3, 10, 30, and 100 μ M) of MG, MG/ β CD, and MG/DM β CD for 48 hours. Note that, the amount of MG in complexes was equivalent to the free form of MG. After that, MTT solution (5 mg/ml) was added to each well and then incubated at 37°C for another 4 hours. Subsequently, the culture medium was withdrawn and 150 μ L of DMSO solution was added to dissolve formazan crystals. Finally, the absorbance was measured at 570 nm using UV spectrophotometer (Thermo Scientific, Vantaa, Finland). The half-maximal inhibitory concentration (IC_{50}) were calculated using GraphPad Prism 7 software.

4.3.2.8 Statistical analysis

The quantitative data are expressed as mean \pm standard error of mean (SEM) of three independent experiments. Differences between groups were determined using one-way analysis of variance (ANOVA) followed by a Newman-Keuls post hoc test. The p value of ≤ 0.05 was considered as statistically significant.

4.4 Results and discussion

4.4.1 System stability of simulated models

The stability of all MD simulations was investigated using root-mean square displacement (RMSD) calculations (Fig. 23). In the case of MG/ β CD, MG/DM β CD, and MG/2HP β CD, all systems are relatively stable in comparison to their initial minimized structure. The RMSD of the MD1 of MG/2HP β CD exhibits the high fluctuation ($\sim 4.5\text{\AA}$) during 55-70 ns and subsequently reduces to $\sim 3\text{-}4\text{\AA}$ after 70 ns. This finding suggests that all simulated complexes enter the equilibrium state at ~ 70 ns; thus, the last 20-ns simulations were selected for further analysis in terms of: (i) ligand mobility inside β CD's hydrophobic cavity along the simulation times, (ii) β CDs conformations upon MG binding, (iii) solvent accessibility toward inclusion complexes, and (iv) binding free energy of inclusion complexes. Surprisingly, the RMSDs of MG/6HP β CD and MG/DHP β CD models highly fluctuate (up to 10\AA) as compared to their starting geometry for all three independent MD runs, indicating that the dissociation of host-guest inclusion complexes was occurred during simulations, which is in accordance with distance analysis (Fig. 24) as discussed later.

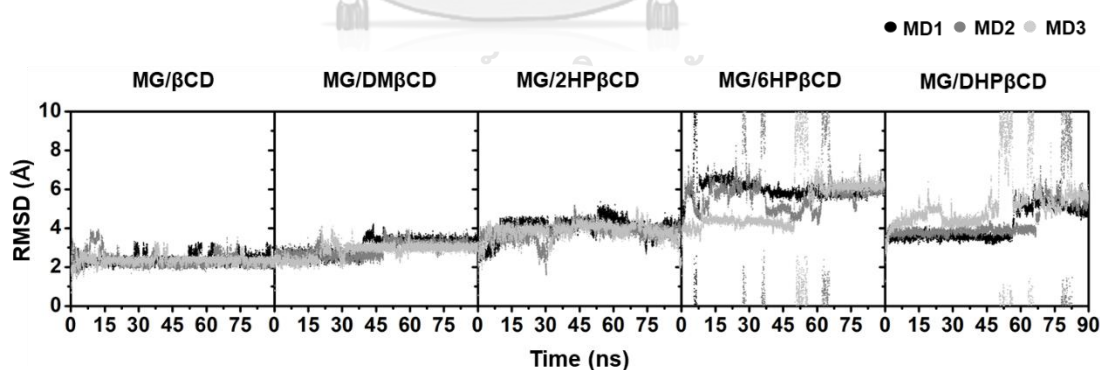


Figure 23 RMSD plot of all investigated inclusion complexes for the three independent MD simulations.

4.4.2 Ligand mobility inside β CD's hydrophobic cavity

The dynamic behavior of the encapsulated MG inside hydrophobic interior of β CD(s) along the simulation times was studied using the calculations of the distance between (i) the center of mass (C_m) of each ring of MG, i.e., aromatic ring (A-ring, black) and quinone ring (Q-ring, grey), and (ii) the C_m of β CD without taking into account the functional substituents. The obtained results are shown in Fig. 24A, whereas the representative binding mode of MG/ β CD(s) taken from the final MD snapshot are depicted in Fig 24B. The horizontal blue box ranging from -3.95\AA to 3.95\AA ($\sim 7.9\text{\AA}$) represents the positions of the primary (narrow) and secondary (wider) rims of native β CD, respectively [191].

In the case of MG/ β CD and MG/2HP β CD systems, MG stably positions nearby the wider rim of β CD(s) and preferentially inserts the A-ring inside the hydrophobic inner cavity. By considering the MG/DM β CD models, MG rapidly moves toward the narrow rim of DM β CD after the heating step and subsequently locates at this orientation until the end of the simulations.

For MG/6HP β CD, and MG/DHP β CD complexes, the ligand moves out of the β CD's cavity, as supported by RMSD calculations (Fig. 23), indicating that HP substitution at C2-position is the preferred host molecule for MG. Our findings are consistent with previous study demonstrating that the HP modification on β CD at C6-position led to the dissociation of the encapsulated mansonones from of β CD's hydrophobic inner cavity [107]. Accordingly, MG/ β CD, MG/DM β CD, and MG/2HP β CD inclusion complexes were selected for further studies, whereas MG/6HP β CD and MG/DHP β CD models were excluded from this research.

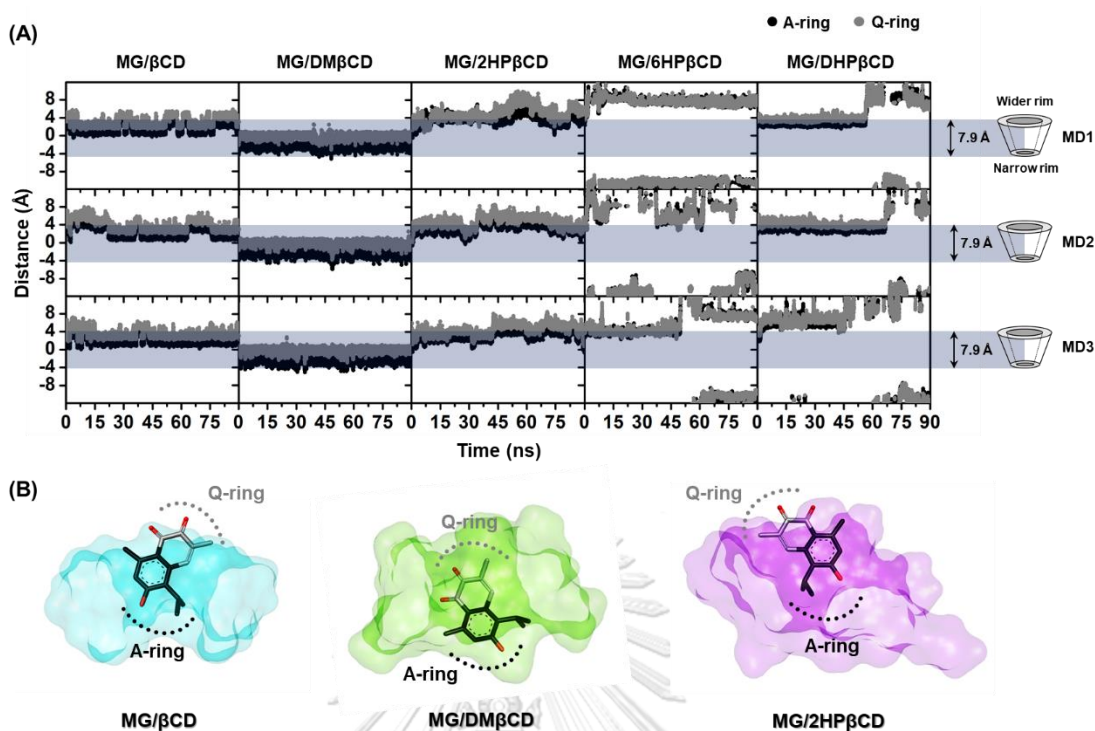


Figure 24 (A) The distance between C_m (A/Q-ring) of MG and C_m of β CD of all studied inclusion complexes for the three MD independent simulations. (B) The binding orientation of MG inside β CD (blue), DM β CD (green), and 2HP β CD (violet) cavities drawn from the last MD snapshot.

4.4.3 β CDs conformations upon MG binding

The β CD(s) conformational changes upon MG encapsulation were investigated by calculating (i) the distance of the secondary hydroxyl groups on the wider rim of β CDs ($O3_{(n)} - O2_{(n+1)}$, dO_{3-2}), corresponding to a possibility of intramolecular hydrogen bond (H-bond) generation (dO_{3-2} of ≤ 3.5 Å), and (ii) the distance of glycosidic oxygen atoms ($O4_{(n)} - O4_{(n+1)}$, dO_{4-4}) (Fig. 25A, left). Afterward, the eq. 4 was used to transform the distributions of these two parameters into the free energy value, $F(x,y)$;

$$F(x,y) = -k_B T \log[P(x,y)] \quad (4)$$

where k_B is the Boltzmann constant, T is the temperature (303K), and $P(x,y)$ is the probability of $dO_{3-2}(x)$ and $dO_{4-4}(y)$. As shown in Fig. 25, the M1 area is the most stable form of the β CD(s), whilst the M2 region represents the rotation of the glucose subunits.

As compared to the unbound form of β CDs exhibiting three local minima areas: M1 (dO_{3-2} of ~ 3 to 4.5 Å and dO_{4-4} of ~ 4.3 to 4.7 Å), M2 (dO_{3-2} of ~ 5 Å and dO_{4-4} of ~ 4.5 to 5.2 Å), and M3 (dO_{3-2} of ~ 5 Å and dO_{4-4} of ~ 6 Å) [192], the molecular encapsulation of MG toward DM β CD and 2HP β CD dramatically induces the stable conformation of β CD(s) by enhancing the formation of intramolecular H-bonds on the wider rim, as evidenced by the obviously increased population in M1 region (dO_{3-2} of ~ 2.5 – 4.5 Å and dO_{4-4} of ~ 4.1 – 4.9 Å, Fig. 25A). In addition, the M3 region with both lengthened distances, which was only detected in free form of β CDs, is completely disappeared in all the bound systems. These H-bond-operated conformational changes of β CD(s) upon the ligand binding correlate well with previously published research [193]. However, the distortion of glucopyranose subunits represented by M2 area is found in MG/ β CD and MG/HP β CD systems but not in MG/DM β CD models, indicating that MG/DM β CD is the most stable complex, in good agreement with $\Delta G_{\text{bind, MM/GBSA}}$ calculations (Table 3) as well as the experimental K_c and $\Delta G_{\text{bind, exp}}$ values (Table 4).

We further characterized the native contact points within 3Å between MG and β CDs during the last 20-ns MD simulations. The obtained results (Fig. 25B) revealed that MG/DM β CD inclusion complex displays the highest number of contacts (6.97 ± 0.62) followed by MG/2HP β CD (6.58 ± 0.78) and MG/ β CD (6.06 ± 0.40) complexes, respectively, as evidenced by the representative 3D contact structures (Fig. 25B, top) showing that MG/DM β CD exhibits the most compact feature. Altogether, the native-contact-driven structures consistently support the PES calculations.

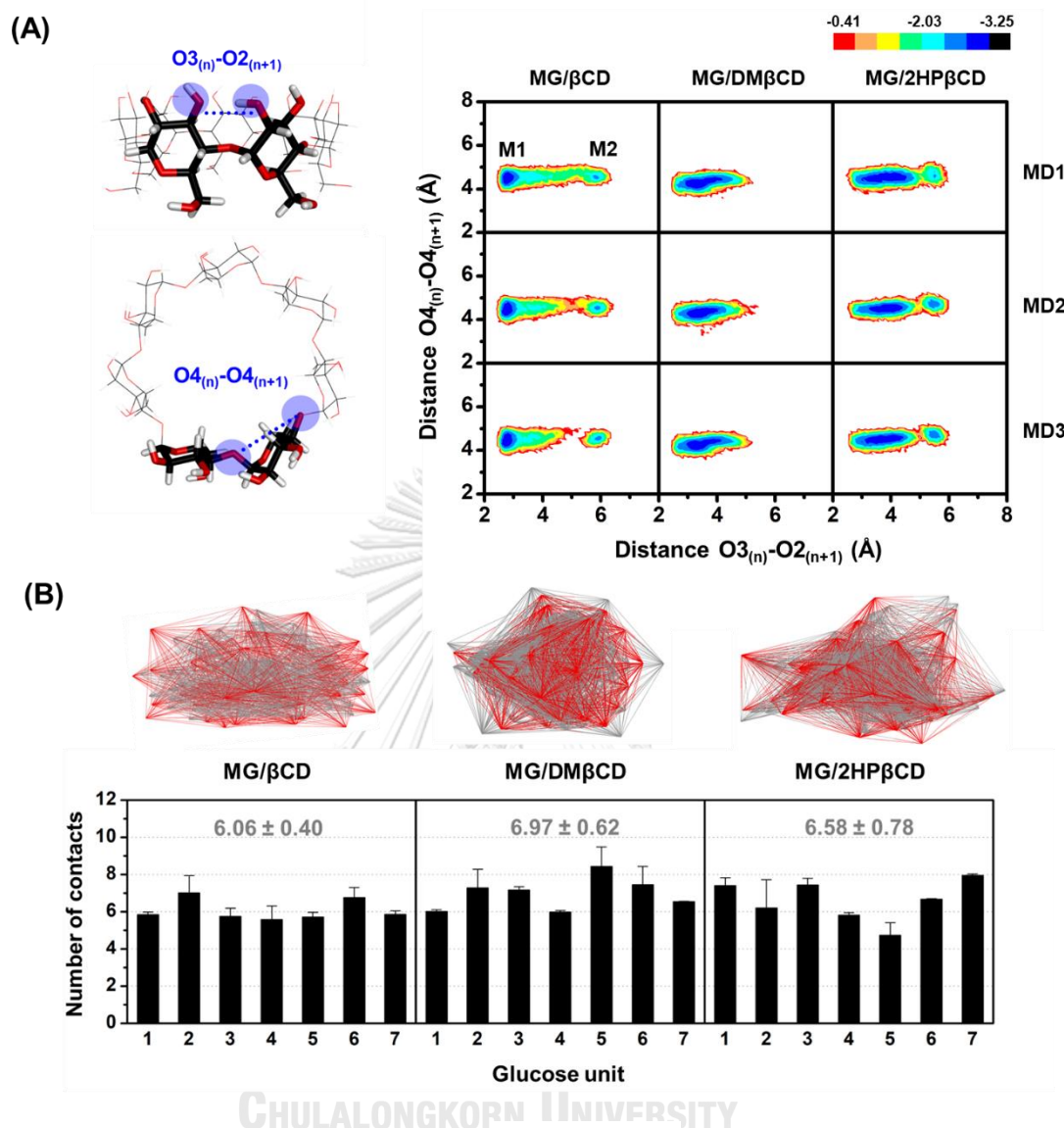


Figure 25 (A) The distance parameters (dO_{3-2} and dO_{4-4}) used for PES calculations (left) as well as the obtained results (right). (B) The representative native contact PDB structures shown in line mode (top) and the number of contacts between MG and glucose units of β CDs (bottom). Data are expressed as mean \pm SEM of three independent MD simulations.

4.4.4 Solvent accessibility toward inclusion complexes

The effect of water accessibility on MG/ β CD(s) inclusion complex formation was characterized by solvent accessible surface area (SASA) calculations using MG as the atomic radii for solvent-exposed area. The entire SASA results are depicted in Fig. 26A,

whereas the averaged SASA values taken from the last 20-ns MD simulations are illustrated in Fig. 26B.

Data in Fig. 426A indicate that the SASAs of MG/ β CD and MG/DM β CD systems are more stable than MG/2HP β CD complexes. The high SASA fluctuation is observed in some systems of MG/ β CD ($\geq 175 \text{ \AA}^2$ at $\sim 50\text{-}90$ ns), whereas the SASAs of MG/DM β CD is relatively steady at $\sim 150 \text{ \AA}^2$ for MD1-3. In the case of MG/2HP β CD models, the SASA values highly fluctuate ($\sim 200\text{-}300 \text{ \AA}^2$) at 40-70 ns and subsequently decrease to $\sim 150 \text{ \AA}^2$ after 70 ns (except MD1). The averaged SASA values in Fig. 26B revealed that the complexation of MG with DM β CD can significantly decrease the water accessibility toward the MG molecule inside β CD inner cavity as compared to the MG/ β CD and MG/2HP β CD ($p \leq 0.05$). These observations correlate well with previous study demonstrating that the lowest solvent exposed inclusion complex displayed the highest binding affinity [194]. However, the SASAs of MG/ β CD and MG/2HP β CD are not significantly different, suggesting that DM β CD is the most preferred encapsulating agent for MG, which is in good correlation with MM/GBSA-based free energy calculations as discussed in the next section.

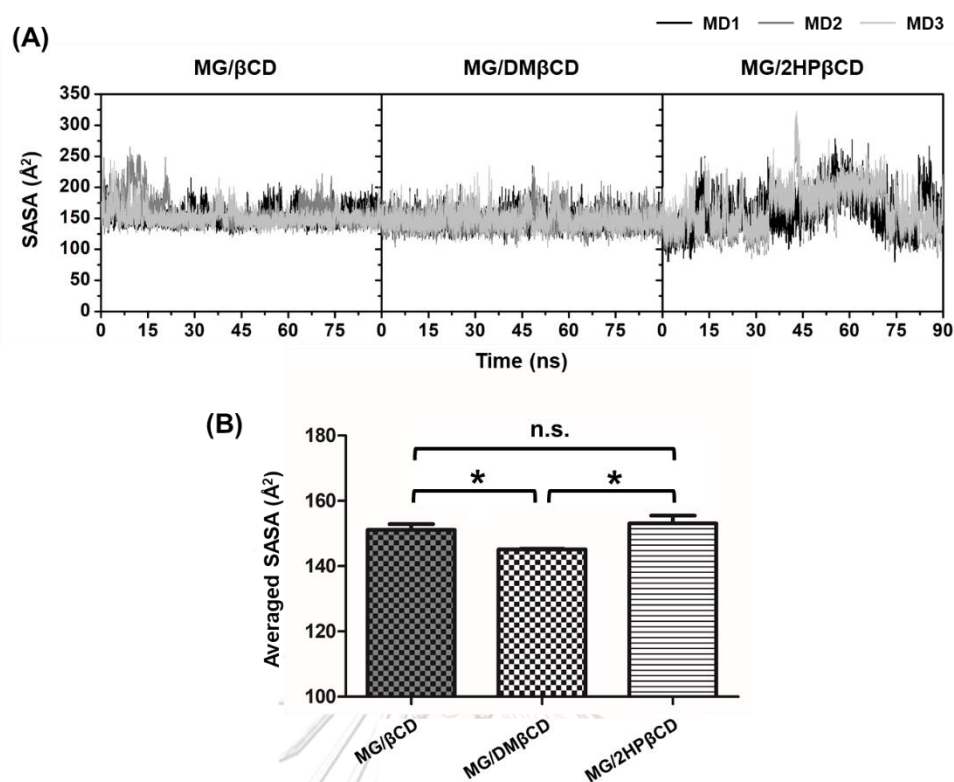


Figure 26 (A) SASA of MG/βCD, MG/DMβCD, and MG/DHPβCD for three different MD runs. (B) The averaged SASA in the last 20-ns MD simulations for each inclusion complex. Data are expressed as mean ± SEM (n=3). *p≤0.05, **p≤0.01, and ***p≤0.001.

4.4.5 Binding free energy of inclusion complexes

To estimate the binding affinity of MG/βCDs inclusion complexes, we applied a molecular mechanics combined with continuum solvation method based on the generalized Born model [195]. The averaged $\Delta G_{\text{bind, MM/GBSA}}$ and its energy component, e.g., vdW (ΔE_{vdW}) and electrostatic (ΔE_{ele}) energies, are summarized in Table 3. As expected, due to the poor solubility of MG, the host-guest complexation in gas phase is driven predominantly by vdW interactions (~-27-29 kcal/mol). Similarly, the summation of $\Delta G_{\text{solv, non-polar}} + \Delta E_{\text{vdW}}$ energies (~-30-32 kcal/mol) is much lower than the $\Delta G_{\text{solv, polar}} + \Delta E_{\text{ele}}$ terms (~8-10 kcal/mol), indicating the vdW forces play a pivotal role in the formation of MG/βCDs in an aqueous environment. These findings strongly correlate with those reported for other hydrophobic ligands in complex with βCDs [196-198].

Several studies have shown that the methyl and hydroxypropyl modifications on β CD can significantly enhance the stability of many lipophilic guest molecules [199-201]. In good agreement with these reports, our results demonstrate that the $\Delta G_{\text{bind, MM/GBSA}}$ of MG in complex with modified β CDs is significantly lower than that of MG in complex with unsubstituted β CD, which can be ranked in the order of MG/ β CD (-2.34 \pm 0.35 kcal/mol) > MG/ β CD (-3.35 \pm 0.14 kcal/mol, *) > MG/DM β CD (-5.73 \pm 0.04 kcal/mol, ***), suggesting that DM β CD analog is the most suitable for MG encapsulation, as supported by a number of structural analyses as described above.

Table 3 The averaged $\Delta G_{\text{bind, MM/GBSA}}$ and its energy components (kcal/mol) of MG/ β CDs inclusion complexes. Data are expressed as mean \pm SEM from three independent MD simulations. ΔE_{MM} , molecular mechanics energy; ΔG_{solv} , solvation free energy comprising polar ($\Delta G_{\text{solv,polar}}$) and non-polar ($\Delta G_{\text{solv,non-polar}}$) terms; ΔS , entropy. * $p \leq 0.05$, ** $p \leq 0.01$, and *** $p \leq 0.001$ vs. MG/ β CD.

Energy component (kcal/mol)	MG/ β CD	MG/DM β CD	MG/2HP β CD
ΔE_{vdW}	-27.61 \pm 1.19	-29.19 \pm 0.29	-28.59 \pm 0.64
ΔE_{ele}	-11.79 \pm 0.40	-4.43 \pm 0.19	-6.40 \pm 0.90
ΔE_{MM}	-39.40 \pm 1.58	-33.62 \pm 0.26	-34.99 \pm 0.26
$\Delta G_{\text{solv,polar}}$	22.14 \pm 0.91	12.72 \pm 0.13	17.17 \pm 0.54
$\Delta G_{\text{solv,non-polar}}$	-2.83 \pm 0.04	-2.98 \pm 0.01	-3.10 \pm 0.02
ΔG_{solv}	19.31 \pm 0.86	9.73 \pm 0.12	14.06 \pm 0.57
$\Delta G_{\text{solv,polar}} + \Delta E_{\text{ele}}$	10.35 \pm 0.53	8.29 \pm 0.19	10.77 \pm 0.47
$\Delta G_{\text{solv,non-polar}} + \Delta E_{\text{vdW}}$	-30.44 \pm 1.24	-32.18 \pm 0.31	-31.69 \pm 0.66
$T\Delta S$	-17.74 \pm 0.36	-18.16 \pm 0.13	-17.57 \pm 0.42
$\Delta G_{\text{bind, MM/GBSA}}$	-2.34 \pm 0.35	-5.73 \pm 0.04 (***)	-3.35 \pm 0.14 (*)

4.4.6 Phase solubility study and thermodynamic parameters

Based on molecular modeling results, we found that DM β CD derivative is the most preferential host for MG; thus, we further confirm our findings by conducting the experimental phase solubility study and Van't Hoff-based thermodynamic parameter evaluation.

Phase solubility diagrams of all studied inclusion complexes at temperatures 30, 37, and 45°C are summarized Fig. 27, where the corresponding K_c values are given in Table 4. The obtained results show that the increased β CD(s) concentrations can enhance the solubility of MG in a liner manner (ranked in the order of DM β CD >> 2HP β CD > β CD), indicating that the stoichiometric ratio between MG and β CD(s) is 1:1 (A_L type) [190]. By considering the stability of all studied inclusion complexes at 30°C, the highest K_c value is detected in MG/DM β CD (2245.26 M⁻¹) followed by MG/HP β CD (684.30 M⁻¹) and MG/ β CD (561.99 M⁻¹), respectively. This observation is consonant well with several reports demonstrating that β CD derivatives, especially DM β CD, could significantly enhance the stability of hydrophobic guest molecules better than natural β CD [184, 202, 203]. However, the increased temperature remarkably reduces the stability of all investigated complexes, in a manner similar to previous works [204, 205].

Using Van't Hoff plot (see Supporting Information, Fig. S2), the obtained thermodynamic values, i.e., ΔH , ΔS , and $\Delta G_{\text{bind, exp}}$, are summarized in Table 5. The negative ΔH (-20.78, -23.27, and -17.39 kcal/mol for MG/ β CD, MG/DM β CD, and MG/HP β CD, respectively) suggests an exothermic process. Moreover, the formation of all inclusion complexes is spontaneous, as evidenced by the negative sign of $\Delta G_{\text{bind, exp}}$ values at 30°C (-3.72, -4.56, -3.85 kcal/mol for MG/ β CD, MG/DM β CD, and MG/HP β CD, respectively). Notably, the trend of $\Delta G_{\text{bind, exp}}$ values strongly agrees with free energies obtained from MM/GBSA method, indicating that our calculations can successfully predict the binding affinity of MG/ β CDs inclusion complexes (Table 5).

Taken together, based on theoretical and experimental investigations, we selected the MG/DM β CD, showing the highest stability, for further structural

characterizations and antitumor evaluation in comparison to the MG/ β CD as well as the free form of MG.

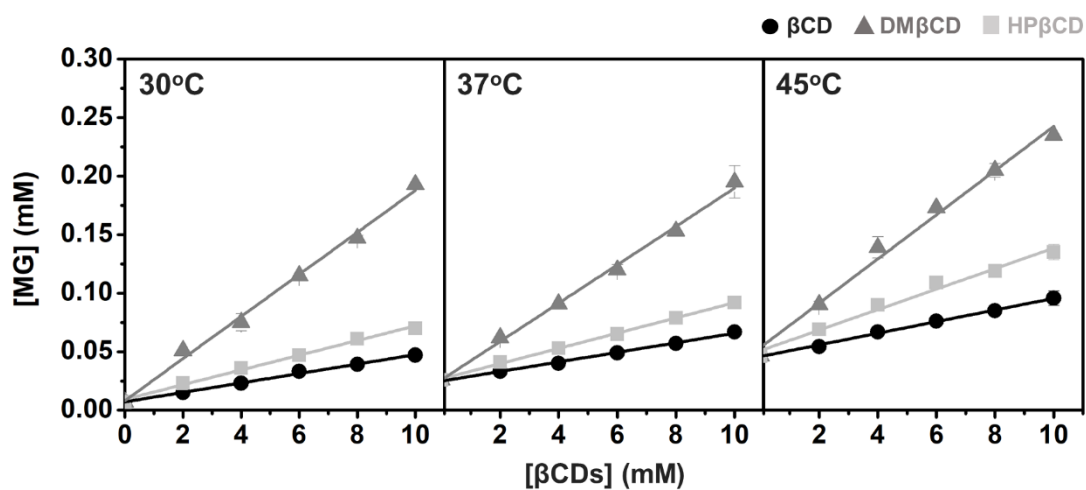


Figure 27 Phase solubility diagram of MG with all studied β CDs in water at 30, 37, and 45 $^{\circ}$ C.

Table 4 K_c of MG/ β CDs inclusion complexes at different temperatures.

Temperature ($^{\circ}$ C)	Stability constant (K_c , M^{-1})		
	MG/ β CD	MG/DM β CD	MG/HP β CD
30	561.99	2245.26	684.30
37	164.87	643.11	244.78
45	108.82	358.08	173.12

Table 5 Thermodynamic values for the inclusion complex formation of MG with β CDs derived from Van't Hoff plots (using R of $1.985 \text{ cal mol}^{-1} \text{ K}^{-1}$ and T of 303K) in comparison to the ΔG_{bind} obtained from MM/GBSA method.

Thermodynamic parameter (kcal/mol)	MG/ β CD	MG/DM β CD	MG/HP β CD
ΔH	-20.78	-23.27	-17.39
$T\Delta S$	-17.06	-18.71	-13.54
$\Delta G_{\text{bind, exp}} (30^\circ\text{C})$	-3.72	-4.56	-3.85
$\Delta G_{\text{bind, MM/GBSA}} (\text{Table 1})$	-2.34	-5.73	-3.35

4.4.7 Inclusion complex characterization

4.4.7.1 Thermal behavior of MG and its inclusion complexes

The thermal behaviors of the starting materials (MG, β CD, and DM β CD) and the inclusion complexes (MG/ β CD, and MG/DM β CD) were characterized in the solid state by DSC analysis (Fig. 28). The characteristic endothermic/exothermic peaks of the free compounds are as follows: MG at 204.9°C and 214.2°C , β CD at 104.3°C and 221.0°C , and DM β CD at 292.7°C . The broad endothermic peak of β CD detected at 104.3°C corresponds to the release of water molecules from the hydrophobic cavity [206].

As a host-guest complexation process is occurred, the thermal features of the acquired product are dramatically changed [207]. In accordance with these facts, our data in Fig. 28 reveal that the thermal peaks of free MG are totally disappeared in the freeze-dried inclusion complexes. In addition, the characteristic peak of the β CD at 104.3°C in MG/ β CD complex is shifted to 57.2°C by the influence of the MG-induced water replacement. The similar change of dehydration peak of β CD after complexation was also found by Rajendiran and coworkers [208]. By considering MG/DM β CD complex, the appearance of new endothermic (42.2°C) and exothermic peaks (187°C)

suggests the formation of a new solid phase [209]. Therefore, the freeze-dried method can successfully generate the inclusion complex between MG and β CDs.

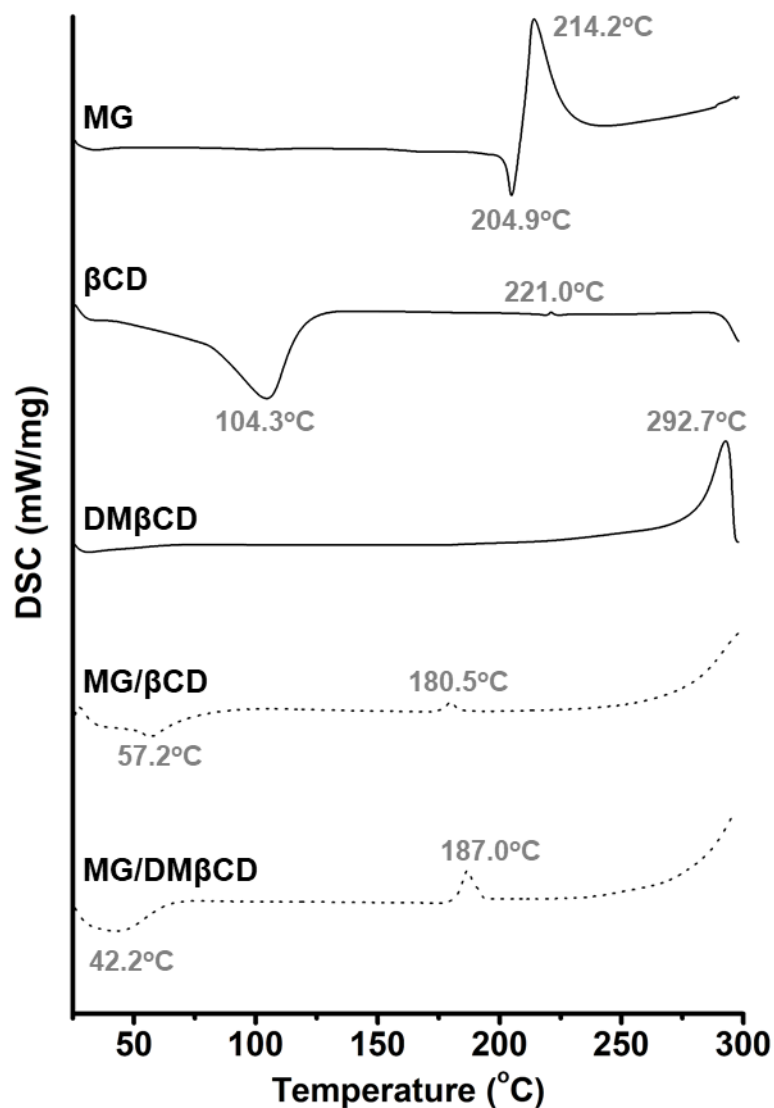


Figure 28 DSC thermogram of MG, β CD, DM β CD, and the freeze-dried inclusion complexes MG/ β CD and MG/DM β CD.

4.4.7.2 Surface morphological changes upon complexation

It was evident that the inclusion complex formation dramatically induces the alterations of the particle shape and surface morphology of the resulting products [210-212]; thus, we performed SEM analysis in order to characterize the morphological

changes upon host-guest encapsulations. The SEM micrographs at 300 times magnification of all investigated samples are summarized in Fig. 29. In the case of the unbound forms, β CD and DM β CD are defined as rod-shaped structure, whereas MG displays a flake-like feature. The particle size can be ranked in the order of β CD \gg DM β CD $>$ MG (Fig. 29A-C). Upon molecular complexation, the surface morphology and the particle shape/size of the obtained freeze-dried inclusion complexes MG/ β CD and MG/DM β CD (Fig. 29D-E) are totally different from those of the free forms (Fig. 29A-C). Remarkably, the MG/DM β CD particles are more compact than MG/ β CD pieces, indicating that MG interacts with DM β CD better than β CD as evidently supported by the native contact calculations as mentioned earlier (Fig. 25B). Taken together, these microscopic results can confirm the successful formation between MG and β CDs, in good agreement with DSC analysis (Fig. 28).

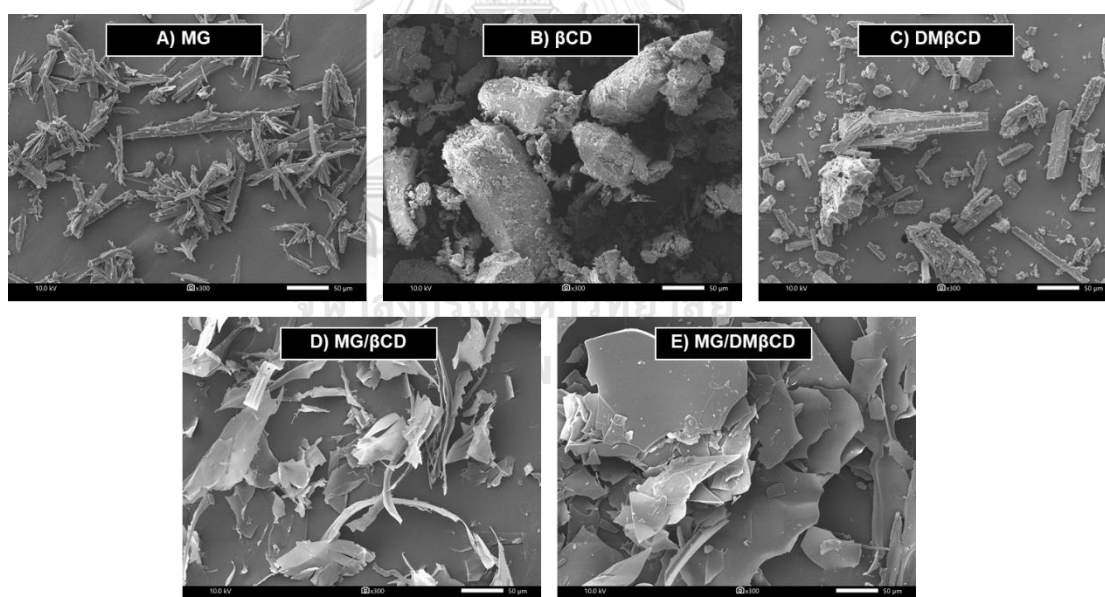


Figure 29 SEM images of (A) MG, (B) β CD, (C) DM β CD, (D) MG/ β CD, and (E) MG/DM β CD at 300 times magnification.

4.4.8 Cytotoxicity of MG/ β CDs inclusion complexes toward lung cancer

Lung cancer is the first leading cause of cancer-related death globally with its five-year survival rate of only 17.8% [3]. In this study, we evaluated the cytotoxic activity of MG and its inclusion complexes, e.g., MG/ β CD and MG/DM β CD against A549 human lung cancer cell line using MTT assay. The cell viability (% of control) results are summarized in Fig. 30A, whereas the IC_{50} values (μ M) are shown in Fig. 30B. The obtained results reveal that MG, MG/ β CD and MG/DM β CD decrease cell viability in a concentration-dependent manner, in which MG/DM β CD (light grey) exhibit the lowest cell viability followed by MG/ β CD (grey) and MG (black), respectively (Fig. 30A).

Multiple lines of evidence have shown that the β CD inclusion complexation can potentially enhance the antitumor activity of lipophilic guest compounds [184, 212, 213]. In correlation with these reports, the present study shows that the inclusion complexes of MG significantly increase the anticancer effect on A549 cells, which can be ranked in the order of MG/DM β CD (IC_{50} of $13.45 \pm 0.24 \mu$ M, ***) > MG/ β CD (IC_{50} of $17.63 \pm 0.42 \mu$ M, ***) >> MG (IC_{50} of $42.86 \pm 2.09 \mu$ M) (Fig. 30B). The enhancement of anticancer activity of MG by β CDs might be due to the enhanced drug permeation through a diffusion barrier called unstirred water layer [214]. Importantly, the free form of β CD and DM β CD does not affect the antitumor property of MG/ β CDs inclusion complexes, as evidenced by the cell viability values of >90% (Fig. 30C).

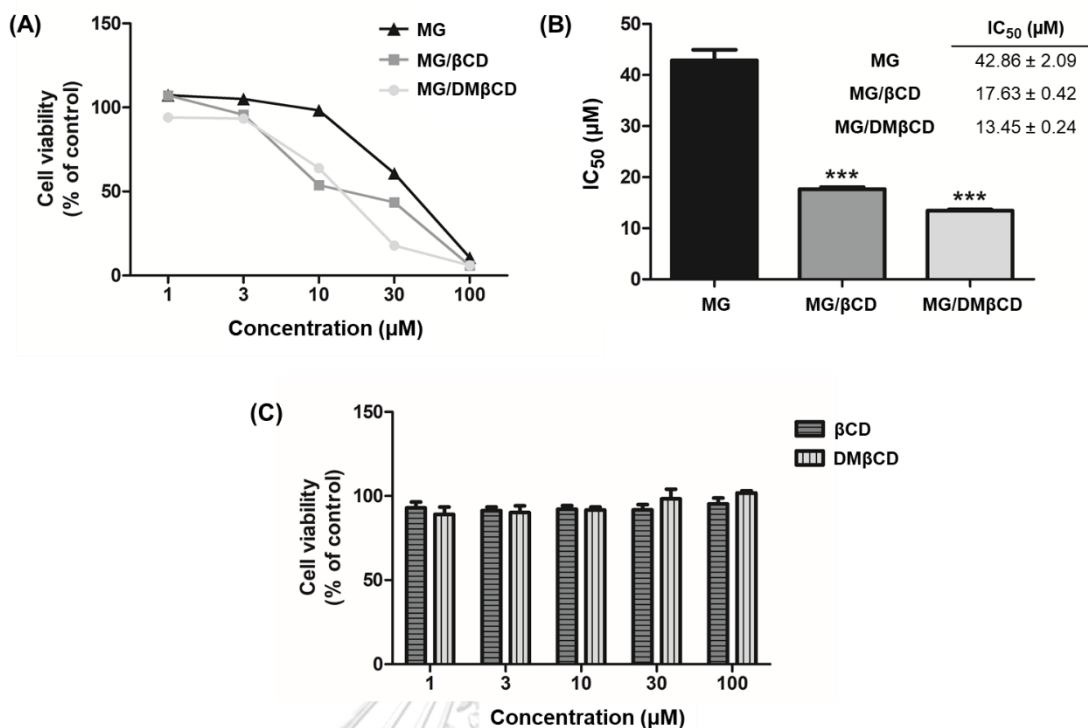


Figure 30 (A) Cell viability of MG, MG/ βCD , and MG/DM βCD against A549 human lung cell line. (B) The IC_{50} of all investigated compounds. (C) Cell viability of the free form of βCD and DM βCD . Data are expressed as mean \pm SEM of three independent experiments. * $p \leq 0.05$, ** $p \leq 0.01$, and *** $p \leq 0.001$ vs. MG.

4.5 Conclusions

In the present study, we combined theoretical and experimental studies to identify the most suitable β CD host molecule for MG, a promising anticancer agent extracted from *Mansonia gagei*, for improving the aqueous solubility and antitumor potential. The 90-ns MD simulations in triplicate revealed that MG preferentially positioned inside β CD, DM β CD, and 2HP β CD cavities rather than C6-substituted HP β CD derivatives. The MG binding led to the rigidity of β CDs by increasing the intramolecular H-bond formations on the wider rim. The lowest SASA toward MG atomic radii was found in MG/DM β CD complex, in correlation with $\Delta G_{\text{bind, MM/GBSA}}$ calculations and experimental phase solubility study. Different spectroscopic techniques confirm the successful formation of MG/ β CDs. The anticancer activity of MG toward A549 lung cancer cells was significantly enhanced (~2-3 fold) by complexation with β CDs, especially DM β CD analog. Altogether, the obtained results confirmed the working hypothesis and demonstrated the good potentiality of DM β CD as the most suitable formulation on MG for further pharmaceutical and medicinal applications.

CHAPTER V

ENHANCED STABILITY AND ENANTIOSEPARATION OF MANSONONE E AND
H/BETA-CYCLODEXTRINS INCLUSION COMPLEXES

**Molecular Insights into Inclusion Complexes of Mansonone E and H Enantiomers with
various β -cyclodextrins**

Panupong Mahalapbutr^a, Bodee Nutho^b, Peter Wolschann^{a,c,d}, Warinthorn Chavasiri^e

Nawee Kungwan^{f,g}, and Thanyada Rungrotmongkol^{a,h*}

^a*Structural and Computational Biology Research Group, Department of Biochemistry, Faculty of Science, Chulalongkorn University, Bangkok 10330, Thailand*

^b*Program in Biotechnology, Faculty of Science, Chulalongkorn University, Bangkok 10330, Thailand*

^c*Department of Pharmaceutical Technology and Biopharmaceutics, University of Vienna, Vienna 1090, Austria*

^d*Institute of Theoretical Chemistry, University of Vienna, Vienna 1090, Austria*

^e*Center of Excellence in Natural Products Chemistry, Department of Chemistry, Faculty of Science, Chulalongkorn University, Bangkok 10330, Thailand*

^f*Department of Chemistry, Faculty of Science, Chiang Mai University, Chiang Mai 50200, Thailand.*

^g*Research Center on Chemistry for Development of Health Promoting Products from Northern Resources, Chiang Mai University, Chiang Mai 50200, Thailand.*

^h*Ph.D. Program in Bioinformatics and Computational Biology, Faculty of Science, Chulalongkorn University, Bangkok 10330, Thailand*

This article has been published in Journal of Molecular Graphic and Modelling (2018)

5.1 Abstract

The structural dynamics and stability of inclusion complexes of mansonone E (ME) and H (MH) including their stereoisomers with various β CDs (methylated- and hydroxypropylated- β CDs) were investigated by classical molecular dynamics (MD) simulations and binding free energy calculations. The simulation results revealed that mansonones are able to form inclusion complexes with β CDs. The guest molecules are not completely inserted into the host cavity, their preferably positions are nearby the secondary rim with the oxane ring dipping into the hydrophobic inner cavity. The encapsulation process leads to a higher rigidity of the β CDs enhancing the intramolecular hydrogen bond formation ability and decreasing the chance of glucopyranose rotation. According to the MM-PBSA binding free energy calculation, all considered inclusion complexes are stable and the binding energies are mainly caused by van der Waals interactions. Moreover, the free energy calculations showed significant differences in the complexation energies for the stereoisomers, which could enable the separation of the isomers by analytical techniques for further pharmaceutical applications.

5.2 Introduction

Quinones and particularly naphthoquinones are cyclic organic compounds ubiquitous in many plants as well as in numerous microorganisms serving as secondary metabolites. These naturally occurring compounds are of intensive research interest due to their wide spectrum of biological activities including antibacterial, antifungal, antimalarial, anti-inflammatory, and antitumor activities [215-218]. The naphthoquinone-containing compounds (NQC), especially mansonones, exhibit great pharmacological activities and have been used in traditional medicine preparations in Thailand over a period of several hundred years. Mansonone E (ME, Fig. 31A) and its hydroxylated form, mansonone H (MH, Fig. 31B) are in the subclass of 1,2-naphthoquinones (*ortho*-naphthoquinone) isolated from the heartwood of *Mansonia gagei* [219] as well as from other plants [216, 220-222]. Their various biological activities were reported including

antifungal activity, radical scavenging property, larvicidal activity [219], cholinesterase (ChE) inhibitory activity [223], topoisomerase I and II inhibitors [224], trypanosomatid growth inhibitors [225], NADPH-dependent microsomal lipid peroxidation [226], and cytotoxicity against various cancer cell lines [220-222]. The cytotoxic action of NQC against cancer cells is resulted from the quinone moiety in their chemical structures [215, 227]. Although many benefits of mansonones were reported, the pharmaceutical and biomedical applications are limited by their low water solubility.

β -cyclodextrin (β CD, Fig. 31C) is a cyclic oligosaccharide consisting of seven D-(+)-glucopyranose units linked together by α -(1,4) glycosidic bonds. In particular, β CD is produced by intramolecular transglycosylation reaction using a cyclodextrin glycosyltransferase (CGTase) enzyme [29]. From the geometry of β CD, the outer surface is hydrophilic to some extent, whilst the inner cavity is rather hydrophobic. Since the D-(+)-glucopyranose units exist in a chair form, the shape of β CD is that of a truncated cone rather than a perfect cylinder [31]. Consequently, β CD can form inclusion complexes with various lipophilic guest molecules by an encapsulation process into its hydrophobic inner cavity. In the recent years, cyclodextrin complexation technology was successfully used to enhance the solubility, stability against oxidative and light degradation, dissolution rate, masking malodors, and bioavailability of many hydrophobic drugs [29-31]. Moreover, β CDs can be used as the chiral selector of many racemic mixtures [32-35] in both the pharmaceutical and chemical industries [228]. However, the practical applications of β CD in pharmaceutical products are still limited by its low water solubility (18.5 mg/mL at 25 °C) and nephrotoxicity [36]. Therefore, the use of higher water-soluble and lower toxic β CD derivatives are immensely required. For instance, 2,6-dimethyl- β CD (2,6-DM β CD), randomly methylated- β CD (RM β CD), and hydroxypropyl- β CD (HP β CD) exhibit a greater water solubility and lower toxicity [31, 36]. Several studies have shown that the water solubility, stability, and biological activities of NQC are increased, while the toxicity of those molecules is reduced by a complexation with β CDs [37-41].

Accordingly, the aims of this work are to predict the encapsulation of ME and MH stereoisomers by suitable β CD derivatives as well as to understand the structural and dynamics properties of the formed inclusion complexes using computational tools.

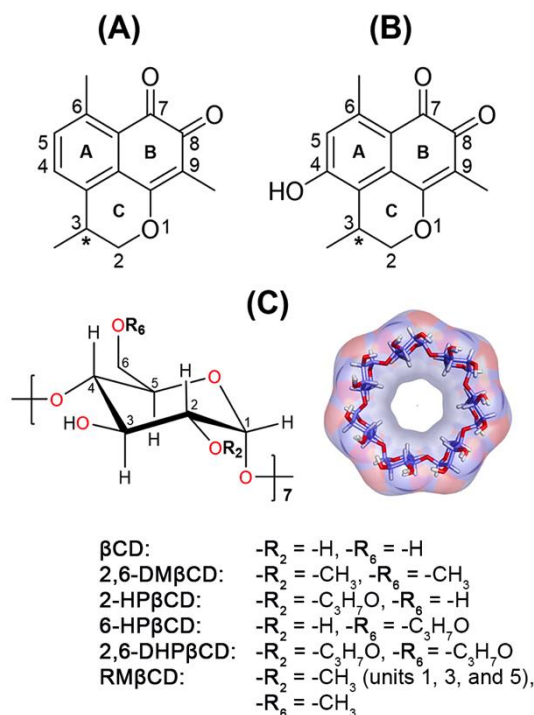


Figure 31 Chemical structures of (A) ME, (B) MH; A, B, and C represent aromatic, quinone, and oxane rings, respectively; C3-position presents the chiral center. (C) Survey of the β CD derivatives used in this study and the 3D structure of β CD.

CHULALONGKORN UNIVERSITY

5.3 Computational details

The optimized structures of β CD and its four derivatives (2,6-DM β CD, 2-HP β CD, 6-HP β CD and 2,6-DHP β CD) were taken from our previous study [229]. Note that the commercially available HP β CD is a partially substituted poly(hydroxypropyl) ether of β CD with various degrees of substitution (DS) [230]. Three models of HP β CD derivatives including 2-HP β CD (DS=1), 6-HP β CD (DS=1) and 2,6-DHP β CD (DS=2) [231] were used as representative structures for the study of the encapsulation reaction. For the RM β CD, the structure was constructed by removing some substituents from 2,6-DM β CD according to the strength of nucleophilicity (primary hydroxyl groups >

secondary hydroxyl groups). Therefore, the three methyl groups are located on the secondary rim at the D-(+)-glucopyranose units 1, 3 and 5, while the hydroxyl groups on the primary rim were fully substituted by seven methyl groups. The starting structures of two mansonones, ME and MH, including their stereoisomers were built and subsequently optimized by the HF/6-31(d) basis set using Gaussian09 program [186]. The inclusion complexes between each mansonone molecule and all six β CDs were constructed by a docking procedure with 500 independent runs using the CDOCKER module implemented in the Accelrys Discovery Studio 2.5^{Accelrys Inc.}. Subsequently, the best three docked complexes at each binding mode were then studied by the classical MD simulations in aqueous solutions using the AMBER14 software package [232]. According to the standard procedures [147, 233-235], the electrostatic potential (ESP) charges around the optimized mansonone structures were calculated by HF/6-31(d) level of theory using Gaussian09 program. The charge fitting procedure (antechamber module) and parmchk module were used for generating the restrained electrostatic potential (RESP) charges and their parameters of two mansonones, respectively. The Glycam06 force field [188] was applied for β CD and its derivatives, whereas the mansonones were treated by the generalized AMBER force field (GAFF). To release bad contacts and to relax the structures prior to MD simulations, all hydrogen atoms of β CDs and the mansonone molecules were minimized with 1000 steps of the steepest descents (SD) method and continued by 3000 steps of conjugated gradient (CG) method. Afterwards, the inclusion complexes were solvated using TIP3P water model with the minimum distance of 15 Å from the system surface. As a result, all systems consisted of 2100 ± 42 water molecules in an approximately $50 \times 50 \times 50 \text{ \AA}^3$ truncated octahedron periodic box. The water molecules were then only minimized with the SD (1000 steps) and CG (3000 steps). Finally, the whole system was minimized using the same minimization process. The periodic boundary condition with *NPT* ensemble was applied for all simulated systems using a time step of 2 fs. Pressure and temperature were controlled by the Berendsen weak coupling algorithm [153]. The cutoff distance for long-range electrostatic interactions was set to 12 Å using the Particle Mesh Ewald

(PME) summation approach [189]. The SHAKE algorithm [115] was used to constrain all bonds involving hydrogen atoms. The models were heated up to 298 K with the relaxation time of 60 ps, and continuously held at this temperature for another 30 ns. The cpptraj module of AMBER14 program was used to calculate the root-mean-square displacement (RMSD), the potential energy surface (PES), the flip angle of glucopyranose units, the distance between the centers of gravity of each mansonone ring and β CD(s), and the radial distribution function (RDF). The MM-PBSA binding free energy of all inclusion complexes were estimated by mm_pbsa.pl module [161] using the 100 snapshots extracted from the last 5-ns simulation.

5.4 Results and discussion

Three independent simulations with different initial structures gave rather similar results. Accordingly, the results from only one system of each stereoisomer are presented here for a simplified interpretation, while the other systems are shown in the supplementary data.

5.4.1 System stability

The system stability of all simulated complexes was evaluated using the root-mean-square displacement (RMSD) calculation. The results showed that all systems reach the equilibrium at ~ 20 ns (Fig. 32). The last 5-ns MD trajectories of each simulated system were extracted for further analysis. The RMSD values of (*R*)- and (*S*)-configurations showed a similar trend observed in the range of 2.5-3.5 Å, 3.0-3.5 Å, 3.5-3.8 Å, 3.0-3.8 Å, and 2.0-2.5 Å for β CD, 2,6-DM β CD, 2,6-DHP β CD, 2-HP β CD, and RM β CD, respectively. Surprisingly, in 6-HP β CD system, both mansonone molecules moved out of the hydrophobic cavity through the primary rim in all 20 individual simulations, resulting in inclusion complex dissociation (data not shown) and thus, these systems were excluded from this study.

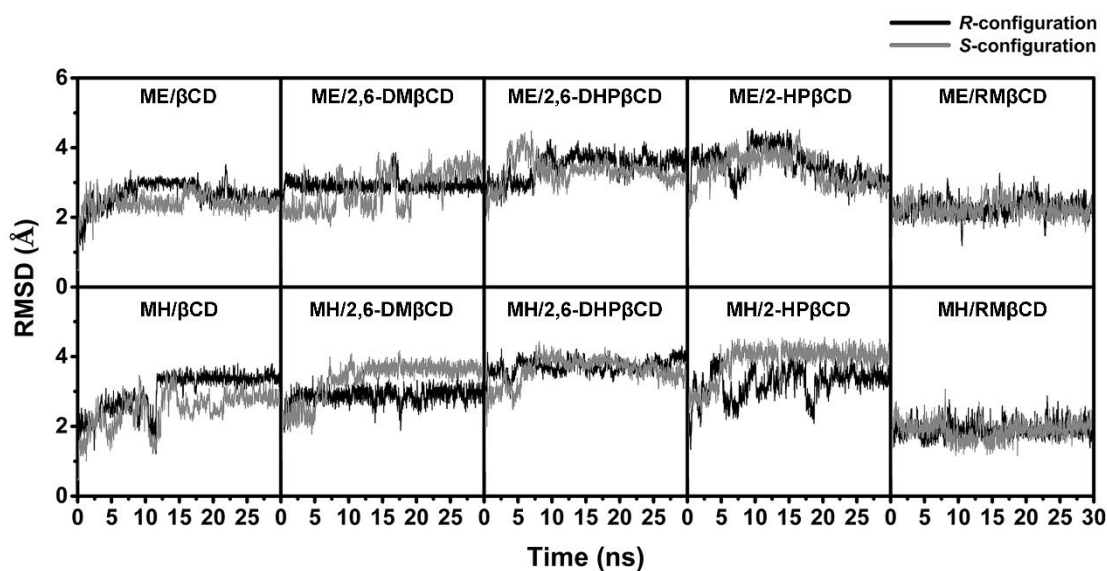


Figure 32 RMSD plots for all atoms of the two stereoisomers of ME and MH inclusion complexes.

5.4.2 βCDs conformation

To investigate the effect of ligand binding on the conformation of βCDs, the distance between two oxygen atoms of all glycosidic linkages ($O4_{(n)} - O4_{(n+1)}$), and the distance between secondary hydroxyl groups on the wider rim of the adjacent glucopyranoses ($O3_{(n)} - O2_{(n+1)}$), corresponding to intramolecular hydrogen bonding, were measured. The distributions of these two distances were converted into the free energy terms (Fig. 33) using the following equation:

$$F(x,y) = -k_B T \log[P(x,y)] \quad (1)$$

where k_B is Boltzmann constant, T is absolute temperature, and $P(x,y)$ is the probability of distances ($O3_{(n)} - O2_{(n+1)}$) and ($O4_{(n)} - O4_{(n+1)}$) as x and y , respectively.

Fig. 33 revealed that the binding of ME and MH in both stereoisomer conformations increases the rigidity of the geometries of βCDs (higher population in M1 than those of the free forms of all βCDs) indicated by a reduction of both focused distances ($O3_{(n)} - O2_{(n+1)}$) and ($O4_{(n)} - O4_{(n+1)}$), leading to an almost perfect conical shape. A rather similar phenomenon was observed in the inclusion complexes of pinostrobin-

and neral- β CDs [229, 231]. The M1 area of the free form of RM β CD appeared to be smaller than that of the parent β CD [229] (Fig. S2 in supplementary data). However, the conformational change of β CDs upon complexation was not only dependent on the ligand binding mode but also on the steric hindrance of such ligands.

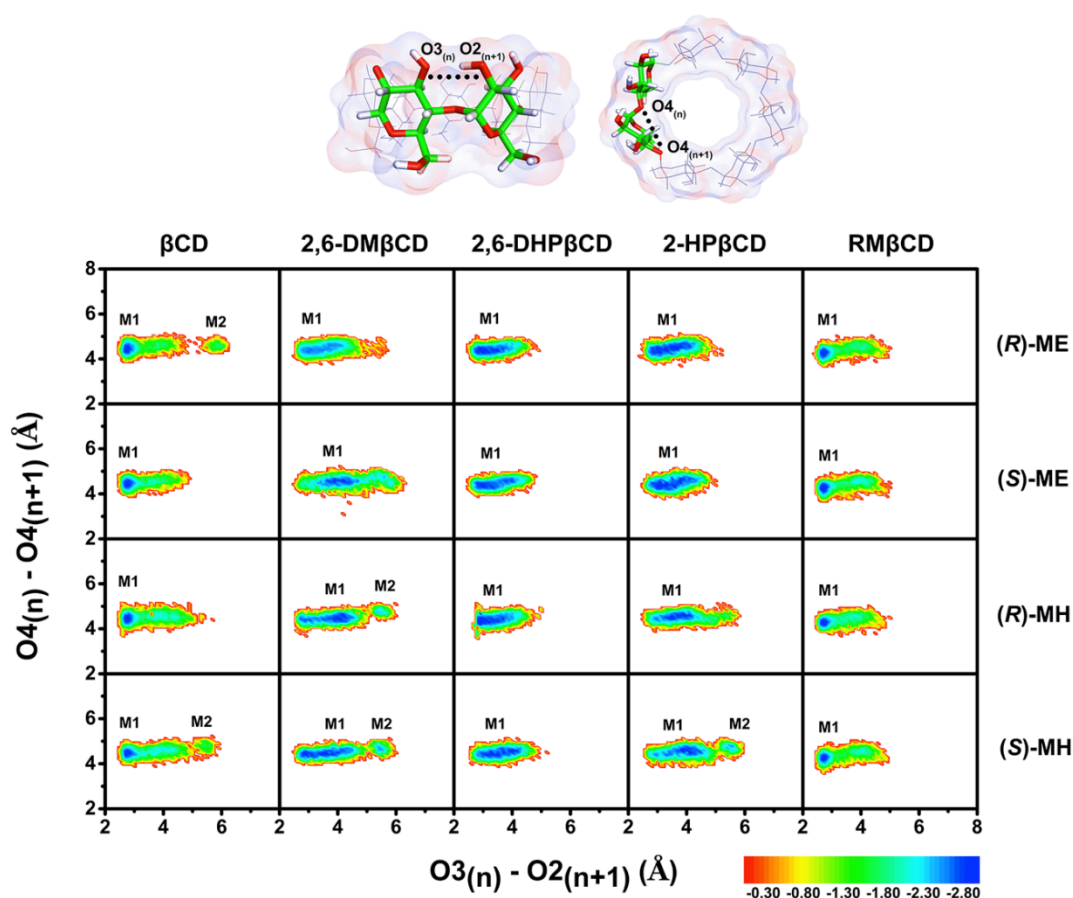


Figure 33 The potential energy surface (PES) spanned by the distance between the adjacent glycosidic oxygens, $O4_{(n)} - O4_{(n+1)}$ and the distance between the secondary hydroxyl groups on the wider rim, $O3_{(n)} - O2_{(n+1)}$ of β CDs in complex with ME and MH.

5.4.3 Transformation of *cis*- to *trans*-configuration of glucopyranose units

The solvation effect derived from water molecules is the important factor affecting β CDs conformations. The water solvation significantly induces the twisted form (82%) of *iota*-cyclodextrin containing fourteen glucopyranose units (CD14)

compared with implicit solvent model (circular form, 85%) [236]. The rotation of glucopyranose units of ϵ -cyclodextrin (CD10) tended to be increased at high temperature simulations [237]. Accordingly, to observe the effect of ligand binding on β CDs conformations, specifically the flips of glucopyranose subunits, the structural parameter of angle $\theta[C6_{(n)} - C2_{(n+1)} - C6_{(n+1)}]$ (Fig. 34A) of the adjacent subunits was calculated. Note that if the angle value was higher than 90 degrees, it could be counted as a flip. The examples of flipped conformations of 2,6-DM β CD are randomly selected as representative structures (Fig. 34B). The averaged percentages of flipped conformations (no-, one-, and two-flip) for all studied systems are summarized in Fig. 35. In case of (*R*)-configurations of ME and MH, no-flip conformation was the major population, especially in (*R*)-ME/2,6-DHP β CD system (almost 100%). The similar finding was observed in (*S*)-configuration in complex with β CD and RM β CD, but the one-flip conformation tended to be significantly increased for 2,6-DM β CD, 2,6-DHP β CD, and 2-HP β CD compared with (*R*)-configuration. According to the previous work [229], the free form of β CD exhibited the no-flip conformation of 58%, which is importantly lower than that of ME and MH/ β CD inclusion complexes (>70% of all systems, Fig. 35). Taken together, the ligand binding likely promoted the stable conformation of β CDs by decreasing the chance of glucopyranose rotation.

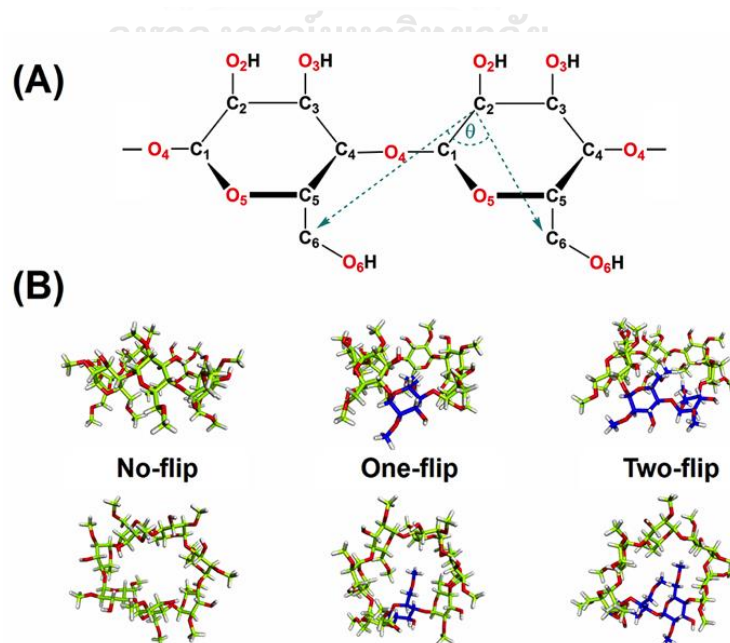


Figure 3 4 (A) The structural parameter of angle $\theta[C6_{(n)} - C2_{(n+1)} - C6_{(n+1)}]$, (B) The examples of flipped conformations of 2,6-DM β CD with different numbers of flipped glucopyranose units.

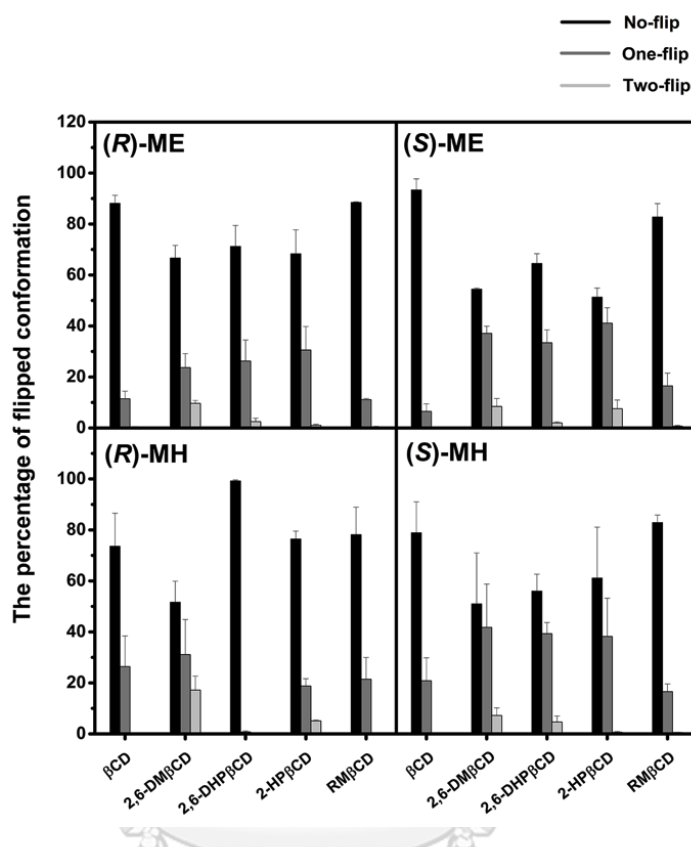


Figure 35 The averaged percentage of flip conformations of β CDs in ligand bound form using the structural parameter of angle $\theta[C6_{(n)} - C2_{(n+1)} - C6_{(n+1)}]$. Note that the standard deviation (SD) was calculated from three independent simulations.

5.4.4 Ligand mobility in β CDs cavities

The dynamics behavior of mansonones inside the β CDs hydrophobic cavity was considered by calculating the distance between the center of gravity of each ring ($Cg_{ringA/B/C}$) and the center of gravity of CD (Cg_{CD}) without taking into account the substituents. The results are summarized in Fig. 36. Normally, the height of unmodified β CD is around 7.9 Å represented by light grey box ranged from -3.95 Å to 3.95 Å according to the positions of the primary and secondary rims, respectively [176, 191]. In case of β CD, 2,6-DM β CD, and RM β CD, the ligands were stably positioned close to the

secondary rim rather than moved down to the CD center or close to the primary rim. This is because these two mansonone molecules consist of three hexagonal rings in the same plane substituted by methyl groups in different positions (Fig. 31). Especially in case of MH, its hydroxyl group has a more pronounced steric influence on the chemical structure, thus, the ligand is positioned closer to secondary rim compared with ME. However, when the height of cavity was significantly increased (i.e., in 2,6-DHP β CD and 2-HP β CD) by addition of hydrophilic functional groups on the rim(s), such a steric hindrance with the rear of the CD cavity was reduced and the two ligands were slightly moved closer to the center of β CDs (~ 1 Å). The oxane ring (C-ring, blue) of ME and MH was more preferentially positioned inside the hydrophobic inner cavity than the other two rings. Especially in the systems (S)-MH/2,6-DM β CD, (R)-ME/2,6-DHP β CD, (S)-MH/2,6-DHP β CD, (R)-ME/2-HP β CD, (R)-MH/2-HP β CD, and (S)-MH/2-HP β CD, the C-ring was flipped to the lower position compared with the initial binding mode and retained this orientation inside CD cavity till the end of simulation. However, the C-ring can be found to be located near the secondary rim in some systems (Fig. S4 in supplementary data). The aromatic ring (A-ring, black) of MH with the hydroxyl group tended to be oriented out of the cavities for reducing the stress in the complexes and interacting with water molecules in correspondence with RDF results (discussed later). Overall, it can be seen that the two stereoisomers of mansonones can form inclusion complexes well with all studied β CDs.

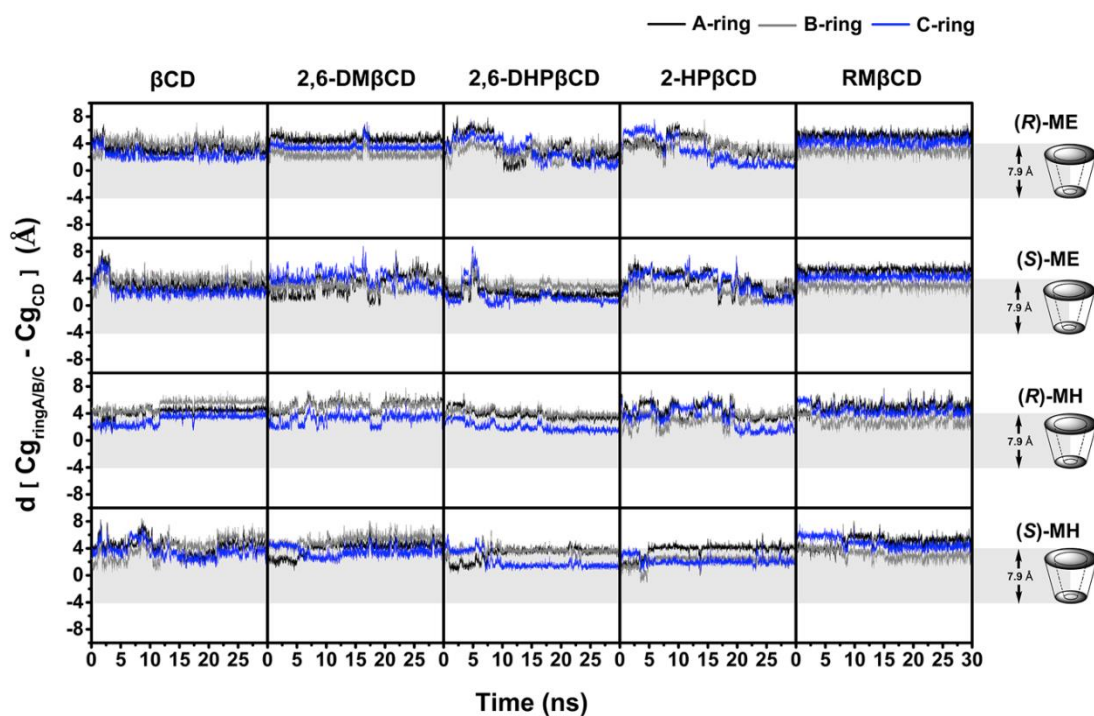


Figure 36 Distance between the center of gravity (Cg) of each ring of ligand and CD ($d [Cg_{\text{ringA/B/C}} - Cg_{\text{CD}}]$). Light grey box represents the height of torus of β CD without the functional modification.

5.4.5 Water accessibility toward inclusion complexes

The radial distribution function (RDF, $g_{ij}(r)$) was used to visualize the water molecules (water oxygen atom j) within a spherical radius r of the mansonone oxygen atom, i . The investigated systems consist of the three oxygen atoms (O1, O7, and O8) for ME and four oxygen atoms (O1, O4, O7, and O8) for MH. The RDFs of the focused oxygen atoms coupled with the integration number ($n(r)$) for all β CDs are plotted in Fig. 37. The $n(r)$ values at the first minimum are summarized in Table 6, corresponding to the number of water molecules pointing toward the targeted oxygen. From RDF plots for all systems, no peak was observed within ~ 3 Å of the O1 oxane oxygen indicating a rather low water accessibility toward the C-ring which is mostly positioned inside the hydrophobic inner cavity. On the other hand, the other oxygen atoms exhibit the first sharp peak at ~ 2.8 Å, corresponding to a better hydration at the first hydration shell. In

case of ME, both O7 and O8 oxygen atoms on the B-ring of unmodified β CD inclusion complexes show the highest water accessibility ($n(r) = 2.0, 2.2, 1.8,$ and 2.5 for O7 of (R)-ME, O8 of (R)-ME, O7 of (S)-ME, and O8 of (S)-ME respectively) compared with the other β CDs, suggesting that these oxygen atoms positioned nearby secondary rim are stabilized by water molecules. However, when the height of cavities was increased by the number of hydrophilic substituents, the solvation interaction was diminished as seen by the lower $n(r)$ values of these two atoms in the modified β CDs. In case of MH, the highest water accessibility was also found in β CD inclusion complexes for O7 and O8 ($n(r) = 2.5, 2.5, 2.0,$ and 2.2 for O7 of (R)-MH, O8 of (R)-MH, O7 of (S)-MH, and O8 of (S)-MH, respectively). The high $n(r)$ values of the O4 oxygen atoms on the A-ring of MH were observed for most systems, especially for RM β CD with $n(r)$ of 2.5 for both (R)- and (S)-MH), suggesting that the A-ring tends to be moved outwards the cavity for alleviating the stress in the complexes and approaching the water molecules outside the hydrophobic inner cavities (evidently from distance analysis).



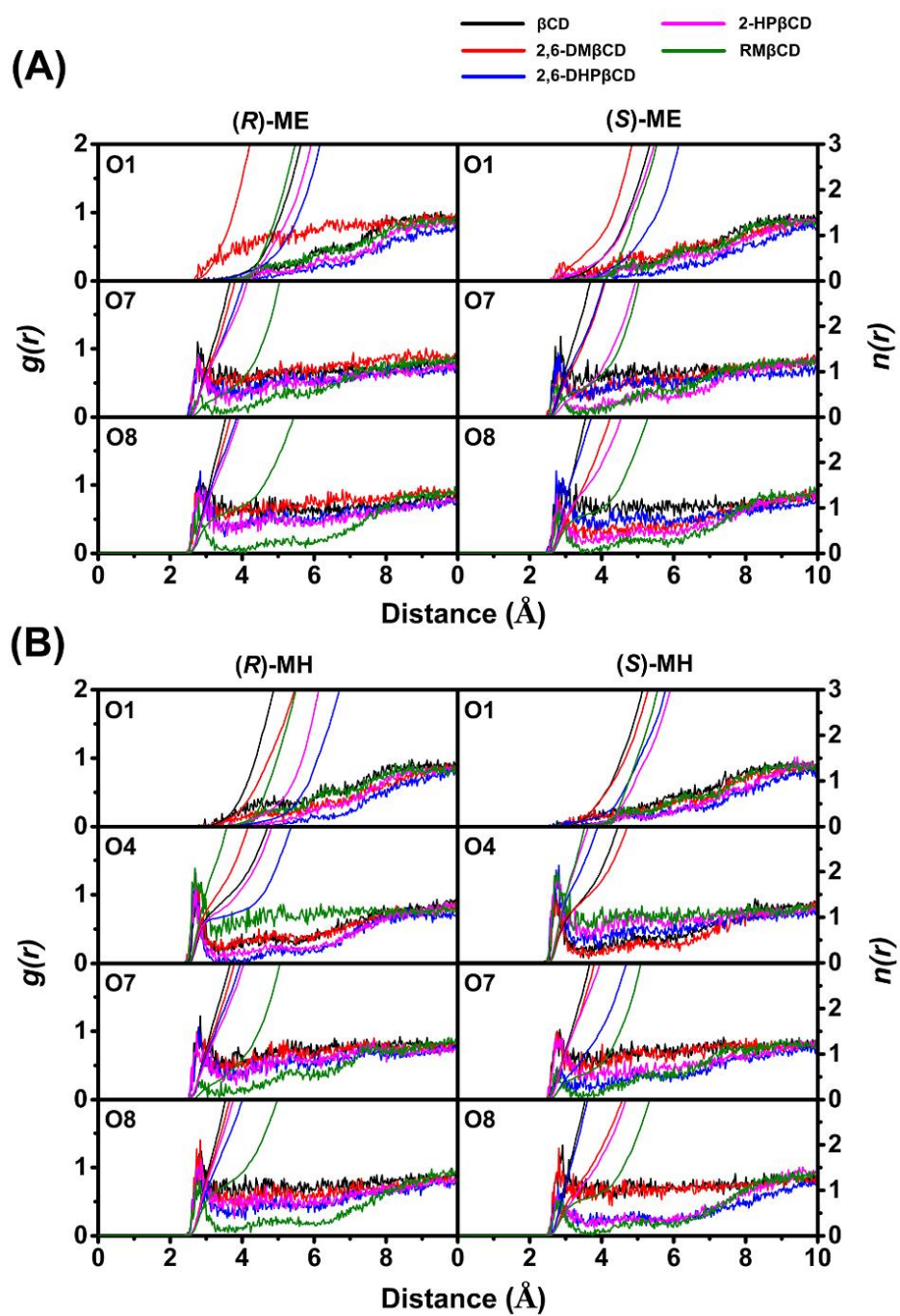


Figure 37 Radial distribution function (RDF) of water oxygen atoms around the focused oxygen atoms of mansonone molecules in different β CDs.

Table 6 Integration number, $n(r)$, up to the first minimum derived from Figure 7 around the focused oxygen atoms of mansonones.

		β CD		2,6-DM β CD		2,6-DHP β CD		2HP β CD		RM β CD	
		(R)-	(S)-	(R)-	(S)-	(R)-	(S)-	(R)-	(S)-	(R)-	(S)-
ME	O1	-	-	-	-	-	-	-	-	-	-
	O7	2.0	1.8	1.8	1.2	1.5	1.5	1.5	0.5	0.5	0.6
	O8	2.2	2.5	1.8	1.2	1.8	2.0	1.8	1.2	1.0	1.0
MH	O1	-	-	-	-	-	-	-	-	-	-
	O4	1.5	1.6	1.5	1.5	1.0	1.8	1.0	2.5	2.5	2.5
	O7	2.5	2.0	2.2	1.8	2.0	0.8	2.0	1.8	0.2	0.5
	O8	2.5	2.2	2.2	1.2	2.0	2.0	2.0	1.2	1.0	0.8

5.4.6 Binding free energy of inclusion complexes

The MM-PBSA approach was performed on 100 MD snapshots extracted from the last 5-ns of the three individual simulations for each complex. The ΔE_{ele} , ΔE_{vdW} , and ΔG_{bind} values of all simulated models are shown in Fig. 38. In the gas phase, the van der Waals energy (ΔE_{vdW}) was approximately 5-fold greater than that of the electrostatic component (ΔE_{ele}) for all systems (Fig. 38A), indicating that van der Waals interaction plays a key role in the complexation process as found in previous studies [148, 197, 229, 238]. The averaged ΔG_{bind} values of inclusion complexes (Fig. 38B) showed that the functional modification of β CD could enhance the stability of both mansonones. In case of ME, the ΔG_{bind} values were ranked in the order of 2,6-DHP β CD > 2-HP β CD ~ RM β CD > 2,6-DM β CD ~ β CD for both (R)- and (S)-configurations. Whereas, the ΔG_{bind} values of MH were ranked in the order of 2,6-DHP β CD > 2-HP β CD ~ RM β CD ~ 2,6-DM β CD ~ β CD for (R)-configuration and of 2,6-DHP β CD > 2-HP β CD ~ RM β CD > 2,6-DM β CD ~ β CD for (S)-configuration. These findings suggest that 2,6-DHP β CD is the most suitable host molecule for the inclusion complex formation, since it has a higher cavity compared with other β CDs, resulting in decreasing of steric hindrances derived from binding of the mansonone molecules inside the hydrophobic cavity. It is worth noting that the commercially available HP β CD derivative is a mixture of various degrees of substitutions, whilst the derivatives used in this study are fully (2,6-DHP β CD) or partial

(2-HP β CD and 6-HP β CD) substituted. Interestingly, the binding free energies estimated from MM-PBSA method correlated well with the experimental phase solubility of other hydrophobic guest molecules, in which β CD derivatives gave the higher K_c values compared with the parent β CD [205, 229, 239].

Additionally, the obtained binding free energies can predict the enantioselectivity of ME and MH stereoisomers. β CD (-8.86 and -11.01 kcal/mol), 2-HP β CD (-10.84 and -14.68 kcal/mol), and RM β CD (-9.30 and -14.30 kcal/mol) can be used as chiral selectors for (*R*)- and (*S*)-MH, while 2,6-DHP β CD (-14.15 and -17.92 kcal/mol) was the enantioseparator for (*R*)- and (*S*)-ME. Importantly, the height of β CDs are also involved in the enantioselectivity as shown in Fig. 39 using (*S*)-ME as a representative model. Due to the fact that the heights of β CD, 2,6-DM β CD, and RM β CD are not significantly different, the enantiomeric separation ability were lower than those of hydroxypropylated β CDs. In case of RM β CD, a high chiral selection toward (*S*)-MH was observed, since the stability of (*S*)-MH inside hydrophobic cavity was greater than that of (*R*)-MH (Fig. 36). Additionally, the $d [Cg_{\text{ringA/B/C}} - Cg_{\text{CD}}]$ of (*R*)-MH reached 8 Å at ~22 ns (Fig. S4), reflecting a high possibility to dissociation. The 2,6-DHP β CD and 2-HP β CD have higher cavities compared with the other β CDs, thus, the preferred enantiomer can be deeply encapsulated into their hydrophobic inner cavities, resulting in a better chiral selectivity. These results correlated well with the previous research in which β CDs, especially hydroxypropylated β CDs, could enhance enantioselectivity of several molecules [240-242]. Taken together, hydroxypropylated β CD derivative was suggested to be the most suitable host molecule for inclusion complex formation in this study and each β CD had the individually enantioselective character toward the focused mansonones.

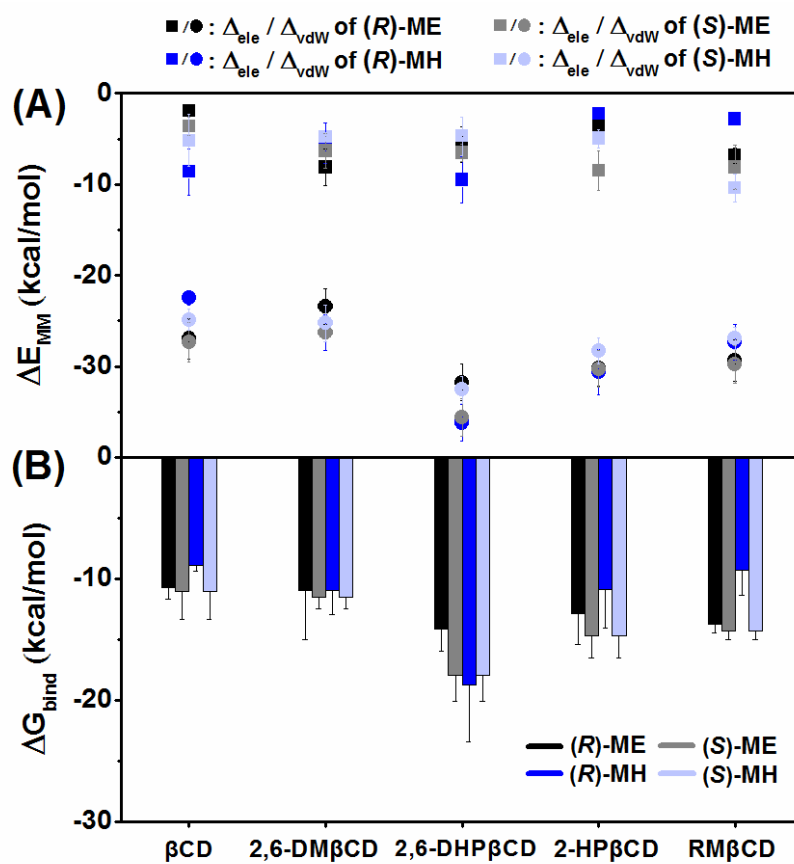


Figure 38 (A) Molecular mechanics energy components in gas phase and (B) the MM-PBSA binding free energy (ΔG_{bind}) for all simulated systems.

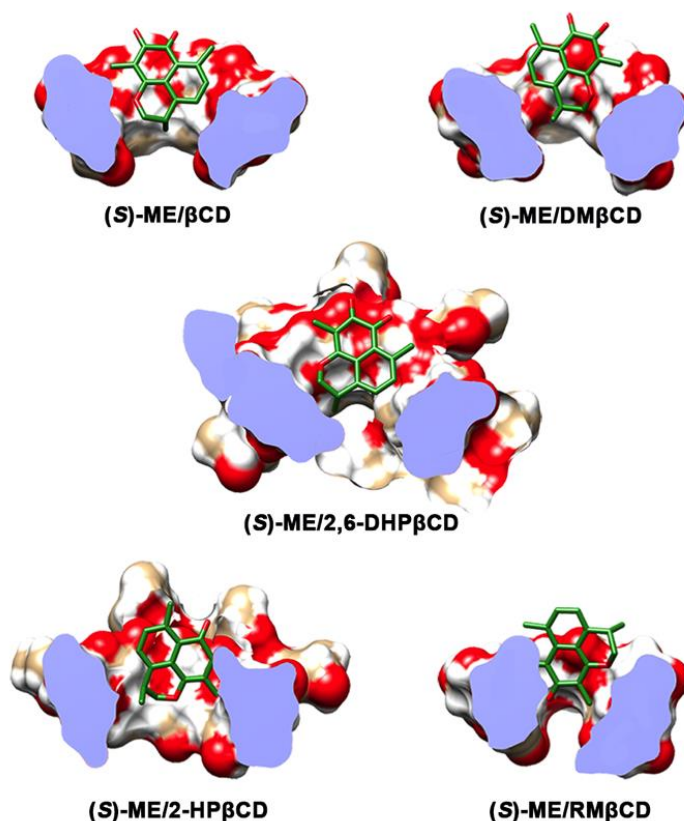


Figure 39 Binding orientations of (S)-ME inside all βCDs taken from the last MD snapshot.

5.5 Conclusions

In the present study, mansonone E (ME) and H (MH) enantiomers were subjected to investigate the structural dynamics as well as to predict the suitable host molecules for inclusion complexation using computational tools. From the classical MD simulations, the system stability of all models reached the equilibrium at ~20 ns and the last 5-ns was subsequently used for investigations. The distance ($d [Cg_{\text{ringA/B/C}} - Cg_{\text{CD}}]$) analysis revealed that mansonone molecules are able to form inclusion complexes quite well and that they are mostly positioned nearby the secondary rim due to the effect of steric hindrance, which was supported by the highest amount of $n(r)$ values of the unmodified βCD from RDF calculations. On the other hand, when the height of cavity was significantly increased (i.e., 2,6-DHPβCD and 2-HPβCD), such steric hindrance was diminished and the ligands could slightly move down to the center of cavity coupled

with the reduction of $n(r)$ values of water accessibility. The PES calculation showed that the ligand binding affected the conformational changes of β CDs by inducing the intramolecular hydrogen bond formation within the inclusion complexes to the most stable form. From the structural parameters of the angle analysis, the no-flip conformation was found to be the major population rather than one- or two-flip conformations of glucopyranose units, resulting from the small fluctuation occurred in the simulation. According to the MM-PBSA binding free energy calculation, as expected for encapsulating the lipophilic guest molecules into the hydrophobic inner cavities, van der Waals interaction was the main driving force for the complexation process rather than long-range electrostatic interactions. The inclusion complexes of mansonones with hydroxypropylated β CD derivative have a higher stability, and are suitable for inclusion complex formation. Moreover, the obtained free energies can provide the effect of enantioselectivity of β CD derivatives toward ME and MH enantiomers for further use in analytical techniques and pharmaceutical applications.



CHAPTER VI

CONCLUSIONS

In the present study, the combination of experimental and theoretical techniques was used to investigate the antitumor potential of MG derivatives on EGFR-mediated signaling pathways in NSCLC cell lines expressing wild-type EGFR (A549) and mutant EGFR (H1975). According to *in vitro* cytotoxicity screening results, MG3 was more susceptible to H1975 mutant cells than A549 wild-type cells. It should be noted that the SI of MG3 was lower than several known anticancer drugs (methotrexate and β -lapachone) and kinase inhibitors (gefitinib and osimertinib). Additionally, the IC_{50} of MG3 in both NSCLC cell lines was 4-8 times lower than the first-line chemotherapeutic drug for lung cancer, CDDP. Mechanistic studies on EGFR-mediated signaling pathways revealed that MG3 induced caspase-dependent apoptosis mechanism through (i) inhibiting p-STAT3 and p-Akt signaling proteins, as supported by MM/GBSA binding free energy calculations, without affecting upstream p-EGFR and (ii) activating MAPK signaling pathway. The PCA results suggested that the binding of MG3 toward STAT3 and Akt dramatically induced protein conformational changes, especially the residues in the binding pocket. These experimental and theoretical findings highlighted MG3 as a possible ligand for further anticancer drug development for NSCLC patients harboring CDDP and TKI resistances.

High expression level of Topo II α , a nuclear enzyme involved in DNA replication and mitotic division, in NSCLC results in the increased rate of cancer cell proliferation. The SITS-based and CDOCKER molecular docking results revealed that MG derivatives preferentially targeted to ATPase domain of Topo II α rather than etoposide pocket and central domain. According to per-residue decomposition free energy analysis, the residues 87-88, 91-92, 94-95, 98-99, 125, 141-142, 147, 150, 161-162, 164-168, 215, and 217 inside ATP-binding pocket were associated with MG(s) binding, by which vdW interactions mainly contributed to protein-ligand complexation. The 100-ns MD

simulations and free energy calculations showed that among all studied MGs, an ester derivative MG14 displayed the highest binding affinity toward ATPase domain of Topo II α by more than the known inhibitors salvicine and 1,4-BQ. By conducting PCA, the results revealed that the MG14 binding affected the secondary structures of Topo II α for both inside and outside ATP-binding pocket. Interestingly, the binding of the most predicted potent compound MG14 promoted the conformational change of the turn structure (residues 145-151) to become significantly located closer to the ligand and Mg²⁺. Altogether, the obtained results suggested that MG14 analog could potentially be developed as a novel Topo II α inhibitor.

β CD complexation technology has been widely used to enhance solubility, stability, enantioselectivity, and biological activity of many lipophilic guest molecules. Note that in this study we chose MG as a representative model since the amount of extracted MG is much higher than a synthesized MG3. The 90-ns MD simulations in triplicate revealed that MG preferentially positioned inside β CD, DM β CD, and 2HP β CD cavities rather than C6-substituted HP β CD derivatives. The MG binding led to the rigidity of β CDs by increasing the intramolecular H-bond formations on the wider rim. The lowest SASA toward MG atomic radii was found in MG/DM β CD complex, in correlation with $\Delta G_{\text{bind, MM/GBSA}}$ calculations and experimental phase solubility study. Different spectroscopic techniques confirm the successful formation of MG/ β CDs. The anticancer activity of MG toward A549 lung cancer cells was significantly enhanced (\sim 2-3 fold) by complexation with β CDs, especially DM β CD analog. Altogether, the obtained results demonstrated the good potentiality of DM β CD as the most suitable formulation on MG for further pharmaceutical and medicinal applications. In addition, the MM/PBSA free calculation on the complexation of ME/MH inclusion complexes provided the effect of enantioselectivity of β CD derivatives toward ME and MH enantiomers, which might be useful for analytical techniques and pharmaceutical applications.

REFERENCES

1. Bray, F., et al., *Global cancer statistics 2018: GLOBOCAN estimates of incidence and mortality worldwide for 36 cancers in 185 countries*. CA: A Cancer Journal for Clinicians, 2018. **68**(6): p. 394-424.
2. Virani, S., et al., *National and Subnational Population-Based Incidence of Cancer in Thailand: Assessing Cancers with the Highest Burdens*. Cancers (Basel), 2017. **9**(8).
3. Wong, M.C.S., et al., *Incidence and mortality of lung cancer: global trends and association with socioeconomic status*. Scientific Reports, 2017. **7**(1): p. 14300.
4. Seshacharyulu, P., et al., *Targeting the EGFR signaling pathway in cancer therapy*. Expert Opinion on Therapeutic Targets, 2012. **16**(1): p. 15-31.
5. Yan, S., et al., *Topoisomerase II alpha expression and the benefit of adjuvant chemotherapy for postoperative patients with non-small cell lung cancer*. BMC Cancer, 2010. **10**(1): p. 621.
6. Zhang, H., *Osimertinib making a breakthrough in lung cancer targeted therapy*. OncoTargets and therapy, 2016. **9**: p. 5489-5493.
7. Bethune, G., et al., *Epidermal growth factor receptor (EGFR) in lung cancer: an overview and update*. Journal of Thoracic Disease, 2010. **2**(1): p. 48-51.
8. Li, X., et al., *Shikonin inhibits gefitinib-resistant non-small cell lung cancer by inhibiting TrxR and activating the EGFR proteasomal degradation pathway*. Pharmacological Research, 2017. **115**: p. 45-55.
9. Yarden, Y. and M.X. Sliwkowski, *Untangling the ErbB signalling network*. Nature Reviews Molecular Cell Biology, 2001. **2**(2): p. 127-37.
10. Pommier, Y., et al., *DNA topoisomerases and their poisoning by anticancer and antibacterial drugs*. Chemistry & Biology, 2010. **17**(5): p. 421-33.
11. Jimenez-Alonso, S., et al., *Design and synthesis of a novel series of pyranonaphthoquinones as topoisomerase II catalytic inhibitors*. Journal of Medicinal Chemistry, 2008. **51**(21): p. 6761-72.

12. Chauhan, M., et al., *Epidermal Growth Factor Receptor (EGFR) and its Cross-Talks with Topoisomerases: Challenges and Opportunities for Multi-Target Anticancer Drugs*. *Current Pharmaceutical Design*, 2016. **22**(21): p. 3226-36.
13. Fennell, D.A., et al., *Cisplatin in the modern era: The backbone of first-line chemotherapy for non-small cell lung cancer*. *Cancer Treatment Reviews*, 2016. **44**: p. 42-50.
14. Smit, E., et al., *Cisplatin and carboplatin-based chemotherapy in the first-line treatment of non-small cell lung cancer: Analysis from the European FRAME study*. *Lung Cancer*, 2016. **92**: p. 35-40.
15. Ozkaya, S., et al., *Cisplatin-based chemotherapy in elderly patients with advanced stage (IIIB and IV) non-small cell lung cancer patients*. *Neoplasma*, 2011. **58**(4): p. 348-51.
16. Rose, M.C., E. Kostyanovskaya, and R.S. Huang, *Pharmacogenomics of Cisplatin Sensitivity in Non-small Cell Lung Cancer*. *Genomics, Proteomics & Bioinformatics*, 2014. **12**(5): p. 198-209.
17. Sarin, N., et al., *Cisplatin resistance in non-small cell lung cancer cells is associated with an abrogation of cisplatin-induced G2/M cell cycle arrest*. *PLoS One*, 2017. **12**(7): p. e0181081.
18. Rosell, R., et al., *Nucleotide excision repair pathways involved in Cisplatin resistance in non-small-cell lung cancer*. *Cancer Control*, 2003. **10**(4): p. 297-305.
19. Kuo, M.T., et al., *The roles of copper transporters in cisplatin resistance*. *Cancer and Metastasis Reviews*, 2007. **26**(1): p. 71-83.
20. Galluzzi, L., et al., *Molecular mechanisms of cisplatin resistance*. *Oncogene*, 2011. **31**: p. 1869.
21. Sun, X. and Y. Zheng, *Cisplatin or Carboplatin for Advanced Non-Small-Cell Lung Cancer?* *Journal of Thoracic Oncology*, 2014. **9**(9): p. e70.
22. Prabhakar, C.N., *Epidermal growth factor receptor in non-small cell lung cancer*. *Translational Lung Cancer Research*, 2015. **4**(2): p. 110-118.
23. Chan, B.A. and B.G.M. Hughes, *Targeted therapy for non-small cell lung cancer:*

- current standards and the promise of the future*. Translational Lung Cancer Research, 2015. 4(1): p. 36-54.
24. Hairani, R., R. Mongkol, and W. Chavasiri, *Allyl and prenyl ethers of mansonone G, new potential semisynthetic antibacterial agents*. Bioorganic & Medicinal Chemistry Letters, 2016. 26(21): p. 5300-5303.
 25. Aljohani, H.G., et al., *Abstract LB-073: Mansonone-G is more potent antiproliferative against liver cancer cells than its coumarin derivative (mansorin-A) despite their antagonistic interaction with 5-fluorouracil*. Cancer Research, 2018. 78(13 Supplement): p. LB-073-LB-073.
 26. Baghdadi, M.A., et al., *Anticancer Profiling for Coumarins and Related O-Naphthoquinones from *Mansonia gagei* against Solid Tumor Cells In Vitro*. Molecules, 2018. 23(5).
 27. Dai, Y., et al., *Isolation and Synthesis of Two Antiproliferative Calamenene-type Sesquiterpenoids from *Sterculia tavia* from the Madagascar Rain Forest*. Bioorganic & Medicinal Chemistry, 2012. 20(24): p. 6940-6944.
 28. Kim, H.K., et al., *CBMG, a novel derivative of mansonone G suppresses adipocyte differentiation via suppression of PPAR γ activity*. Chemico-Biological Interactions, 2017. 273: p. 160-170.
 29. Del Valle, E.M.M., *Cyclodextrins and their uses: a review*. Process Biochemistry, 2004. 39(9): p. 1033-1046.
 30. Loftsson, T. and M.E. Brewster, *Pharmaceutical Applications of Cyclodextrins. 1. Drug Solubilization and Stabilization*. Journal of Pharmaceutical Sciences, 1996. 85(10): p. 1017-1025.
 31. Loftsson, T. and M. Masson, *Cyclodextrins in topical drug formulations: theory and practice*. International Journal of Pharmaceutics, 2001. 225(1-2): p. 15-30.
 32. Vakily, M., et al., *Inclusion complexation of heptakis(2,6-di-O-ethyl)-beta-cyclodextrin with tiaprofenic acid: pharmacokinetic consequences of a pH-dependent release and stereoselective dissolution*. Journal of Pharmaceutical Sciences, 1995. 84(8): p. 1014-9.

33. Desiderio, C., C.M. Polcaro, and S. Fanali, *Stereoselective analysis of herbicides by capillary electrophoresis using sulfobutyl ether beta-cyclodextrin as chiral selector*. *Electrophoresis*, 1997. **18**(2): p. 227-34.
34. Quang, C. and M.G. Khaledi, *Improved chiral separation of basic compounds in capillary electrophoresis using beta-cyclodextrin and tetraalkylammonium reagents*. *Analytical Chemistry*, 1993. **65**(23): p. 3354-8.
35. Zhou, S., et al., *Chiral separation of four fluoroquinolone compounds using capillary electrophoresis with hydroxypropyl-beta-cyclodextrin as chiral selector*. *Journal of Chromatography A*, 2006. **1130**(2): p. 296-301.
36. Zhao, Y., et al., *Preparation, characterization, and pharmacokinetics study of capsaicin via hydroxypropyl-beta-cyclodextrin encapsulation*. *Pharmaceutical Biology*, 2016. **54**(1): p. 130-8.
37. Nasongkla, N., et al., *Enhancement of Solubility and Bioavailability of β -Lapachone Using Cyclodextrin Inclusion Complexes*. *Pharmaceutical Research*, 2003. **20**(10): p. 1626-1633.
38. Wang, F., et al., *Modulating β -lapachone release from polymer millirods through cyclodextrin complexation*. *Journal of Pharmaceutical Sciences*, 2006. **95**(10): p. 2309-2319.
39. Groom, C.A. and J.H.T. Luong, *Fluorescence studies on the reduction of quinone by cyanide in aqueous 2-hydroxypropyl- β -cyclodextrin solutions*. *Analytica Chimica Acta*, 1994. **296**(3): p. 255-261.
40. Zhao, M.-X., et al., *Enhanced anti-cancer efficacy to cancer cells by doxorubicin loaded water-soluble amino acid-modified β -cyclodextrin platinum complexes*. *Journal of Inorganic Biochemistry*, 2014. **137**: p. 31-39.
41. Linares, M., M.a.M. de Bertorello, and M. Longhi, *Solubilization of naphthoquinones by complexation with hydroxypropyl- β -cyclodextrin*. *International Journal of Pharmaceutics*, 1997. **159**(1): p. 13-18.
42. L., S.R., M.K. D., and J. Ahmedin, *Cancer statistics, 2018*. CA: A Cancer Journal for Clinicians, 2018. **68**(1): p. 7-30.

43. Cheng, T.-Y.D., et al., *The International Epidemiology of Lung Cancer: Latest Trends, Disparities, and Tumor Characteristics*. Journal of Thoracic Oncology, 2016. 11(10): p. 1653-1671.
44. Islami, F., L.A. Torre, and A. Jemal, *Global trends of lung cancer mortality and smoking prevalence*. Translational Lung Cancer Research, 2015. 4(4): p. 327-338.
45. Su, T.-J., et al., *Oncogenic miR-137 contributes to cisplatin resistance via repressing CASP3 in lung adenocarcinoma*. American Journal of Cancer Research, 2016. 6(6): p. 1317-1330.
46. Raimbourg, J., et al., *Sensitization of EGFR Wild-Type Non-Small Cell Lung Cancer Cells to EGFR-Tyrosine Kinase Inhibitor Erlotinib*. Molecular Cancer Therapeutics, 2017. 16(8): p. 1634-1644.
47. Leighl, N.B., *Treatment paradigms for patients with metastatic non-small-cell lung cancer: first-, second-, and third-line*. Current Oncology, 2012. 19(Suppl 1): p. S52-8.
48. Dasari, S. and P.B. Tchounwou, *Cisplatin in cancer therapy: molecular mechanisms of action*. European journal of pharmacology, 2014. 0: p. 364-378.
49. Weber, B., et al., *EGFR mutation frequency and effectiveness of erlotinib: a prospective observational study in Danish patients with non-small cell lung cancer*. Lung Cancer, 2014. 83(2): p. 224-30.
50. Matsuo, N., et al., *Association of EGFR Exon 19 Deletion and EGFR-TKI Treatment Duration with Frequency of T790M Mutation in EGFR-Mutant Lung Cancer Patients*. Scientific Reports, 2016. 6: p. 36458.
51. Wakeling, A.E., et al., *ZD1839 (Iressa). An Orally Active Inhibitor of Epidermal Growth Factor Signaling with Potential for Cancer Therapy*, 2002. 62(20): p. 5749-5754.
52. Wang, S., S. Cang, and D. Liu, *Third-generation inhibitors targeting EGFR T790M mutation in advanced non-small cell lung cancer*. Journal of Hematology & Oncology, 2016. 9: p. 34.
53. Mayor, S., *Osimertinib effective in EGFR T790M-positive lung cancer*. The Lancet

- Oncology, 2017. **18**(1): p. e9.
54. Ma, C., S. Wei, and Y. Song, *T790M and acquired resistance of EGFR TKI: a literature review of clinical reports*. Journal of Thoracic Disease, 2011. **3**(1): p. 10-18.
 55. Ko, B., D. Paucar, and B. Halmos, *EGFR T790M: revealing the secrets of a gatekeeper*. Lung Cancer: Targets and Therapy, 2017. **8**: p. 147-159.
 56. Mongkol, R. and W. Chavasiri, *Antimicrobial, herbicidal and antifeedant activities of mansonone E from the heartwoods of Mansonia gagei Drumm*. Journal of Integrative Agriculture, 2016. **15**(12): p. 2795-2802.
 57. El-Halawany, A.M., R. Salah El Dine, and M. Hattori, *Anti-estrogenic activity of mansonone G and mansorin A derivatives*. Pharm Biol, 2013. **51**(8): p. 948-54.
 58. Changwong, N., et al., *Acetyl- and butyryl-cholinesterase inhibitory activities of mansorins and mansonones*. Phytotherapy Research, 2012. **26**(3): p. 392-6.
 59. Cetintas, V.B., et al., *Cisplatin resistance induced by decreased apoptotic activity in non-small-cell lung cancer cell lines*. Cell Biology International, 2012. **36**(3): p. 261-5.
 60. Bortner, C.D. and J.A. Cidlowski, *A necessary role for cell shrinkage in apoptosis*. Biochemical Pharmacology, 1998. **56**(12): p. 1549-59.
 61. Yen, H.-Y., et al., *Effect of sialylation on EGFR phosphorylation and resistance to tyrosine kinase inhibition*. Proceedings of the National Academy of Sciences, 2015. **112**(22): p. 6955-6960.
 62. Lelj-Garolla, B., et al., *Hsp27 Inhibition with OGX-427 Sensitizes Non-Small Cell Lung Cancer Cells to Erlotinib and Chemotherapy*. Molecular Cancer Therapeutics, 2015. **14**(5): p. 1107-1116.
 63. Shin, D.-S., et al., *Cryptotanshinone Inhibits Constitutive Signal Transducer and Activator of Transcription 3 Function through Blocking the Dimerization in DU145 Prostate Cancer Cells*. Cancer Research, 2009. **69**(1): p. 193-202.
 64. Siddiquee, K., et al., *Selective chemical probe inhibitor of Stat3, identified through structure-based virtual screening, induces antitumor activity*. Proceedings of the

- National Academy of Sciences of the United States of America, 2007. **104**(18): p. 7391-7396.
65. Pachl, F., et al., *Characterization of a chemical affinity probe targeting Akt kinases*. J Proteome Res, 2013. **12**(8): p. 3792-800.
 66. Burns, S., et al., *Identification of small-molecule inhibitors of protein kinase B (PKB/AKT) in an AlphaScreen™ high-throughput screen*. Journal of Biomolecular Screening, 2006. **11**(7): p. 822-7.
 67. Samadi Moghaddam, M., M. Heiny, and V.P. Shastri, *Enhanced cellular uptake of nanoparticles by increasing the hydrophobicity of poly(lactic acid) through copolymerization with cell-membrane-lipid components*. Chemical Communications, 2015. **51**(78): p. 14605-14608.
 68. Franks, N.P. and W.R. Lieb, *Partitioning of long-chain alcohols into lipid bilayers: implications for mechanisms of general anesthesia*. Proceedings of the National Academy of Sciences of the United States of America, 1986. **83**(14): p. 5116-5120.
 69. Li, Y., et al., *Novel Selective and Potent EGFR Inhibitor that Overcomes T790M-Mediated Resistance in Non-Small Cell Lung Cancer*. Molecules, 2016. **21**(11).
 70. Vazirian, M., et al., *Comparison of cytotoxic activity of some Iranian Stachys spp. extracts on different cancer cell lines*. Vol. 1. 2014. 23-28.
 71. Patel, R.M. and S.K. Patel, *Cytotoxic activity of methanolic extract of artocarpus heterophyllus against a549, hela and mcf-7 cell lines*. Vol. 1. 2011. 167-171.
 72. Paludo, C.R., et al., *Inactivation of beta-Lapachone Cytotoxicity by Filamentous Fungi that Mimic the Human Blood Metabolism*. European Journal of Drug Metabolism and Pharmacokinetics, 2017. **42**(2): p. 213-220.
 73. McIlwain, D.R., T. Berger, and T.W. Mak, *Caspase functions in cell death and disease*. Cold Spring Harbor perspectives in biology, 2013. **5**(4): p. a008656.
 74. Suda, K., et al., *EGFR T790M Mutation: A Double Role in Lung Cancer Cell Survival?* Journal of Thoracic Oncology, 2009. **4**(1): p. 1-4.
 75. Henkels, K.M. and J.J. Turchi, *Cisplatin-induced apoptosis proceeds by caspase-3-dependent and -independent pathways in cisplatin-resistant and -sensitive*

- human ovarian cancer cell lines*. Cancer Research, 1999. **59**(13): p. 3077-83.
76. Cummings, B.S. and R.G. Schnellmann, *Cisplatin-induced renal cell apoptosis: caspase 3-dependent and -independent pathways*. Journal of Pharmacology and Experimental Therapeutic, 2002. **302**(1): p. 8-17.
77. Kaushal, G.P., et al., *Role and regulation of activation of caspases in cisplatin-induced injury to renal tubular epithelial cells*. Kidney International, 2001. **60**(5): p. 1726-1736.
78. Dai, C.H., et al., *RNA interferences targeting the Fanconi anemia/BRCA pathway upstream genes reverse cisplatin resistance in drug-resistant lung cancer cells*. Journal of Biomedical Science, 2015. **22**: p. 77.
79. Aziz, M.H., N.E. Dreckschmidt, and A.K. Verma, *Plumbagin, a Medicinal Plant-Derived Naphthoquinone, Is a Novel Inhibitor of the Growth and Invasion of Hormone-Refractory Prostate Cancer*. Cancer Research, 2008. **68**(21): p. 9024-9032.
80. Sandur, S.K., et al., *5-hydroxy-2-methyl-1,4-naphthoquinone, a vitamin K3 analogue, suppresses STAT3 activation pathway through induction of protein tyrosine phosphatase, SHP-1: potential role in chemosensitization*. Molecular Cancer Research, 2010. **8**(1): p. 107-18.
81. Sand, J.M., et al., *Plumbagin (5-hydroxy-2-methyl-1,4-naphthoquinone), isolated from *Plumbago zeylanica*, inhibits ultraviolet radiation-induced development of squamous cell carcinomas*. Carcinogenesis, 2012. **33**(1): p. 184-90.
82. Qiu, H.-Y., et al., *Identification of new shikonin derivatives as STAT3 inhibitors*. Biochemical Pharmacology, 2017. **146**: p. 74-86.
83. Qiu, H.-Y., et al., *Identification of New Shikonin Derivatives as Antitumor Agents Targeting STAT3 SH2 Domain*. Scientific Reports, 2017. **7**(1): p. 2863.
84. Kawiak, A. and E. Lojkowska, *Ramentaceone, a Naphthoquinone Derived from *Drosera* sp., Induces Apoptosis by Suppressing PI3K/Akt Signaling in Breast Cancer Cells*. PLOS ONE, 2016. **11**(2): p. e0147718.
85. Nishina, A., et al., *Mansonone E from *Mansonia gagei* Inhibited alpha-MSH-*

- Induced Melanogenesis in B16 Cells by Inhibiting CREB Expression and Phosphorylation in the PI3K/Akt Pathway*. Biological and Pharmaceutical Bulletin, 2018. **41**(5): p. 770-776.
86. Fletcher, S., et al., *Disruption of Transcriptionally Active Stat3 Dimers with Non-phosphorylated, Salicylic Acid-Based Small Molecules: Potent in vitro and Tumor Cell Activities*. Chembiochem : a European journal of chemical biology, 2009. **10**(12): p. 1959-1964.
87. Liu, L.J., et al., *Identification of a natural product-like STAT3 dimerization inhibitor by structure-based virtual screening*. Cell Death Dis, 2014. **5**: p. e1293.
88. Shao, S., et al., *Dual-inhibitors of STAT5 and STAT3: studies from molecular docking and molecular dynamics simulations*. Journal of Molecular Modeling, 2014. **20**(8): p. 2399.
89. Sgrignani, J., et al., *Structural Biology of STAT3 and Its Implications for Anticancer Therapies Development*. International Journal of Molecular Sciences, 2018. **19**(6): p. 1591.
90. Davies, T.G., et al., *A structural comparison of inhibitor binding to PKB, PKA and PKA-PKB chimera*. Journal of Molecular Biology, 2007. **367**(3): p. 882-94.
91. Allen, F.H., *The Cambridge Structural Database: a quarter of a million crystal structures and rising*. Acta Crystallographica Section B, 2002. **58**(Pt 3 Pt 1): p. 380-8.
92. Jackson, P.A., et al., *Covalent Modifiers: A Chemical Perspective on the Reactivity of α,β -Unsaturated Carbonyls with Thiols via Hetero-Michael Addition Reactions*. Journal of Medicinal Chemistry, 2017. **60**(3): p. 839-885.
93. Yang, J., et al., *Molecular mechanism for the regulation of protein kinase B/Akt by hydrophobic motif phosphorylation*. Molecular Cell, 2002. **9**(6): p. 1227-40.
94. Addie, M., et al., *Discovery of 4-amino-N-[(1S)-1-(4-chlorophenyl)-3-hydroxypropyl]-1-(7H-pyrrolo[2,3-d]pyrimidin-4-yl)piperidine-4-carboxamide (AZD5363), an orally bioavailable, potent inhibitor of Akt kinases*. Journal of Medicinal Chemistry, 2013. **56**(5): p. 2059-73.

95. Siddik, Z.H., *Cisplatin: mode of cytotoxic action and molecular basis of resistance*. *Oncogene*, 2002. **22**: p. 7265.
96. Tan, B.J. and G.N. Chiu, *Role of oxidative stress, endoplasmic reticulum stress and ERK activation in triptolide-induced apoptosis*. *International Journal of Oncology*, 2013. **42**(5): p. 1605-12.
97. Zhuang, S. and R.G. Schnellmann, *A death-promoting role for extracellular signal-regulated kinase*. *Journal of Pharmacology and Experimental Therapeutics*, 2006. **319**(3): p. 991-7.
98. Persons, D.L., E.M. Yazlovitskaya, and J.C. Pelling, *Effect of extracellular signal-regulated kinase on p53 accumulation in response to cisplatin*. *Journal of Biological Chemistry*, 2000. **275**(46): p. 35778-85.
99. Greig, M.J., et al., *Effects of Activating Mutations on EGFR Cellular Protein Turnover and Amino Acid Recycling Determined Using SILAC Mass Spectrometry*. *International Journal of Cell Biology*, 2015. **2015**: p. 798936.
100. Becker, S., B. Groner, and C.W. Muller, *Three-dimensional structure of the Stat3beta homodimer bound to DNA*. *Nature*, 1998. **394**(6689): p. 145-51.
101. Schwede, T., et al., *SWISS-MODEL: an automated protein homology-modeling server*. *Nucleic Acids Research*, 2003. **31**(13): p. 3381-3385.
102. Mahalapbutr, P., et al., *Molecular recognition of naphthoquinone-containing compounds against human DNA topoisomerase II α ATPase domain: A molecular modeling study*. *Journal of Molecular Liquids*, 2017. **247**: p. 374-385.
103. Frisch, M.J., et al., *Gaussian 09*. 2009, Gaussian, Inc.: Wallingford, CT, USA.
104. Wu, G., et al., *Detailed analysis of grid-based molecular docking: A case study of CDOCKER-A CHARMM-based MD docking algorithm*. *Journal of Computational Chemistry*, 2003. **24**(13): p. 1549-62.
105. Olsson, M.H., et al., *PROPKA3: Consistent Treatment of Internal and Surface Residues in Empirical pKa Predictions*. *Journal of Chemical Theory and Computation*, 2011. **7**(2): p. 525-37.
106. Phanich, J., et al., *Role of R292K mutation in influenza H7N9 neuraminidase*

- toward oseltamivir susceptibility: MD and MM/PB(GB)SA study. *Journal of Computer-Aided Molecular Design*, 2016. **30**(10): p. 917-926.
107. Mahalapbutr, P., et al., *Molecular insights into inclusion complexes of mansonone E and H enantiomers with various beta-cyclodextrins*. *Journal of Molecular Graphics and Modelling*, 2018. **79**: p. 72-80.
108. Meeprasert, A., S. Hannongbua, and T. Rungrotmongkol, *Key Binding and Susceptibility of NS3/4A Serine Protease Inhibitors against Hepatitis C Virus*. *Journal of Chemical Information and Modeling*, 2014. **54**(4): p. 1208-1217.
109. Maier, J.A., et al., *ff14SB: Improving the Accuracy of Protein Side Chain and Backbone Parameters from ff99SB*. *Journal of Chemical Theory and Computation*, 2015. **11**(8): p. 3696-3713.
110. Wang, J., et al., *Development and testing of a general amber force field*. *Journal of Computational Chemistry*, 2004. **25**(9): p. 1157-74.
111. Sangpheak, W., et al., *Enhanced stability of a naringenin/2,6-dimethyl β -cyclodextrin inclusion complex: Molecular dynamics and free energy calculations based on MM- and QM-PBSA/GBSA*. *Journal of Molecular Graphics and Modelling*, 2014. **50**: p. 10-15.
112. Mahalapbutr, P., et al., *A theoretical study on the molecular encapsulation of luteolin and pinocembrin with various derivatized beta-cyclodextrins*. *Journal of Molecular Structure*, 2019. **1180**: p. 480-490.
113. Jorgensen, W.L., et al., *Comparison of simple potential functions for simulating liquid water*. *The Journal of Chemical Physics*, 1983. **79**(2): p. 926-935.
114. York, D.M., T.A. Darden, and L.G. Pedersen, *The effect of long-range electrostatic interactions in simulations of macromolecular crystals: A comparison of the Ewald and truncated list methods*. *The Journal of Chemical Physics*, 1993. **99**(10): p. 8345-8348.
115. Ryckaert, J.-P., G. Ciccotti, and H.J.C. Berendsen, *Numerical integration of the cartesian equations of motion of a system with constraints: molecular dynamics of n-alkanes*. *Journal of Computational Physics*, 1977. **23**(3): p. 327-341.

116. Genheden, S. and U. Ryde, *The MM/PBSA and MM/GBSA methods to estimate ligand-binding affinities*. *Expert Opinion on Drug Discovery*, 2015. **10**(5): p. 449-461.
117. Jiménez-Alonso, S., et al., *Design and Synthesis of a Novel Series of Pyranonaphthoquinones as Topoisomerase II Catalytic Inhibitors*. *Journal of Medicinal Chemistry*, 2008. **51**(21): p. 6761-6772.
118. Regal, K.M., S.L. Mercer, and J.E. Dewese, *HU-331 Is a Catalytic Inhibitor of Topoisomerase II α* . *Chemical Research in Toxicology*, 2014. **27**(12): p. 2044-2051.
119. Bender, R.P., A.J. Ham, and N. Osheroff, *Quinone-induced enhancement of DNA cleavage by human topoisomerase II α : adduction of cysteine residues 392 and 405*. *Biochemistry*, 2007. **46**(10): p. 2856-64.
120. Baviskar, A.T., et al., *Switch in Site of Inhibition: A Strategy for Structure-Based Discovery of Human Topoisomerase II α Catalytic Inhibitors*. *ACS Medicinal Chemistry Letters*, 2015. **6**(4): p. 481-5.
121. Gibson, E.G., et al., *Two-Mechanism Model for the Interaction of Etoposide Quinone with Topoisomerase II α* . *Chemical Research in Toxicology*, 2016. **29**(9): p. 1541-1548.
122. Drwal, M.N., et al., *Novel DNA Topoisomerase II α Inhibitors from Combined Ligand- and Structure-Based Virtual Screening*. *PLOS ONE*, 2014. **9**(12): p. e114904.
123. Fortune, J.M. and N. Osheroff, *Merbarone inhibits the catalytic activity of human topoisomerase II α by blocking DNA cleavage*. *Journal of Biological Chemistry*, 1998. **273**(28): p. 17643-50.
124. Robinson, M.J., A.H. Corbett, and N. Osheroff, *Effects of topoisomerase II-targeted drugs on enzyme-mediated DNA cleavage and ATP hydrolysis: evidence for distinct drug interaction domains on topoisomerase II*. *Biochemistry*, 1993. **32**(14): p. 3638-43.
125. Burden, D.A. and N. Osheroff, *Mechanism of action of eukaryotic topoisomerase II and drugs targeted to the enzyme*. *Biochimica et Biophysica Acta*, 1998. **1400**(1-

- 3): p. 139-54.
126. Hu, C.X., et al., *Salvicine functions as novel topoisomerase II poison by binding to ATP pocket*. *Molecular Pharmacology*, 2006. **70**(5): p. 1593-601.
127. Tanabe, K., et al., *Inhibition of Topoisomerase II by Antitumor Agents Bis(2,6-dioxopiperazine) Derivatives*. *Cancer Research*, 1991. **51**(18): p. 4903-4908.
128. Singh, G., K.G. Jayanarayan, and C.S. Dey, *Novobiocin induces apoptosis-like cell death in topoisomerase II over-expressing arsenite resistant Leishmania donovani*. *Molecular and Biochemical Parasitology*, 2005. **141**(1): p. 57-69.
129. Tsukagoshi, S., *[A novel antitumor agent, sobuzoxane (MST-16)]*. *Gan To Kagaku Ryoho*, 1994. **21**(7): p. 1089-97.
130. Driscoll, J.S., *Quinone structure-antitumor activity relationships*. *Cancer Chemotherapy Reports. Part 2*, 1974. **4**(4): p. 3-4.
131. Doroshov, J.H., *Role of hydrogen peroxide and hydroxyl radical formation in the killing of Ehrlich tumor cells by anticancer quinones*. *Proceedings of the National Academy of Sciences*, 1986. **83**(12): p. 4514-4518.
132. Wang, Y., et al., *Hydrogen peroxide activated quinone methide precursors with enhanced DNA cross-linking capability and cytotoxicity towards cancer cells*. *European Journal of Medicinal Chemistry*, 2017. **133**: p. 197-207.
133. Sidlauskas, K., et al., *5-Hydroxy-1,4-naphthalenedione exerts anticancer effects on glioma cells through interaction with the mitochondrial electron transport chain*. *Neuroscience Letters*, 2017. **639**: p. 207-214.
134. Kadela-Tomanek, M., et al., *Alkynyloxy derivatives of 5,8-quinolinedione: Synthesis, in vitro cytotoxicity studies and computational molecular modeling with NAD(P)H:Quinone oxidoreductase 1*. *European Journal of Medicinal Chemistry*, 2017. **126**: p. 969-982.
135. Kumar, B.S., et al., *Synthesis of pharmacologically important naphthoquinones and anticancer activity of 2-benzylawsone through DNA topoisomerase-II inhibition*. *Bioorganic & Medicinal Chemistry*, 2017. **25**(4): p. 1364-1373.
136. Gurbani, D., et al., *Mechanism of inhibition of the ATPase domain of human*

- topoisomerase IIalpha* by 1,4-benzoquinone, 1,2-naphthoquinone, 1,4-naphthoquinone, and 9,10-phenanthroquinone. *Toxicological Sciences*, 2012. **126**(2): p. 372-90.
137. Baker, R.K., et al., *Benzene metabolites antagonize etoposide-stabilized cleavable complexes of DNA topoisomerase IIalpha*. *Blood*, 2001. **98**(3): p. 830-3.
138. Lindsey, R.H., Jr., et al., *1,4-Benzoquinone is a topoisomerase II poison*. *Biochemistry*, 2004. **43**(23): p. 7563-74.
139. Tiew, P., et al., *Antifungal, antioxidant and larvicidal activities of compounds isolated from the heartwood of *Mansonia gagei**. *Phytotherapy Research*, 2003. **17**(2): p. 190-3.
140. Dai, Y., et al., *Isolation and synthesis of two antiproliferative calamenene-type sesquiterpenoids from *Sterculia tavia* from the Madagascar rain forest*. *Bioorganic & Medicinal Chemistry*, 2012. **20**(24): p. 6940-4.
141. Pandey, A.K., et al., *In silico studies with human DNA topoisomerase-II alpha to unravel the mechanism of in vitro genotoxicity of benzene and its metabolites*. *Mutation Research*, 2009. **661**(1-2): p. 57-70.
142. Wu, W.B., et al., *Synthesis and evaluation of mansonone F derivatives as topoisomerase inhibitors*. *European Journal of Medicinal Chemistry*, 2011. **46**(8): p. 3339-47.
143. Wei, H., et al., *Nucleotide-dependent domain movement in the ATPase domain of a human type IIA DNA topoisomerase*. *Journal of Biological Chemistry*, 2005. **280**(44): p. 37041-7.
144. Wendorff, T.J., et al., *The structure of DNA-bound human topoisomerase II alpha: conformational mechanisms for coordinating inter-subunit interactions with DNA cleavage*. *Journal of Molecular Biology*, 2012. **424**(3-4): p. 109-24.
145. Irwin, J.J., et al., *ZINC: A Free Tool to Discover Chemistry for Biology*. *Journal of Chemical Information and Modeling*, 2012. **52**(7): p. 1757-1768.
146. Yang, L. and Y. Qin Gao, *A selective integrated tempering method*. *The Journal of Chemical Physics*, 2009. **131**(21): p. 214109.

147. Meeprasert, A., et al., *Binding pattern of the long acting neuraminidase inhibitor laninamivir towards influenza A subtypes H5N1 and pandemic H1N1*. Journal of Molecular Graphics and Modelling, 2012. **38**: p. 148-54.
148. Sangpheak, W., et al., *Enhanced stability of a naringenin/2,6-dimethyl beta-cyclodextrin inclusion complex: molecular dynamics and free energy calculations based on MM- and QM-PBSA/GBSA*. Journal of Molecular Graphics and Modelling, 2014. **50**: p. 10-5.
149. Nutho, B., et al., *Binding mode and free energy prediction of fisetin/ β -cyclodextrin inclusion complexes*. Beilstein Journal of Organic Chemistry, 2014. **10**: p. 2789-2799.
150. Liu, P., et al., *Replica exchange with solute tempering: A method for sampling biological systems in explicit water*. Proceedings of the National Academy of Sciences of the United States of America, 2005. **102**(39): p. 13749-13754.
151. Huang, X., et al., *Replica Exchange with Solute Tempering: Efficiency in Large Scale Systems*. The Journal of Physical Chemistry B, 2007. **111**(19): p. 5405-5410.
152. Gao, Y.Q., *An integrate-over-temperature approach for enhanced sampling*. The Journal of Chemical Physics, 2008. **128**(6): p. 064105.
153. Berendsen, H.J.C., et al., *Molecular dynamics with coupling to an external bath*. The Journal of Chemical Physics, 1984. **81**(8): p. 3684-3690.
154. Trott, O. and A.J. Olson, *AutoDock Vina: improving the speed and accuracy of docking with a new scoring function, efficient optimization and multithreading*. Journal of Computational Chemistry, 2010. **31**(2): p. 455-461.
155. Meeprasert, A., S. Hannongbua, and T. Rungrotmongkol, *Key binding and susceptibility of NS3/4A serine protease inhibitors against hepatitis C virus*. Journal of Chemical Information and Modeling, 2014. **54**(4): p. 1208-17.
156. Kaiyawet, N., T. Rungrotmongkol, and S. Hannongbua, *Effect of Halogen Substitutions on dUMP to Stability of Thymidylate Synthase/dUMP/mTHF Ternary Complex Using Molecular Dynamics Simulation*. Journal of Chemical Information and Modeling, 2013. **53**(6): p. 1315-1323.

157. Phanich, J., et al., *A 3D-RISM/RISM study of the oseltamivir binding efficiency with the wild-type and resistance-associated mutant forms of the viral influenza B neuraminidase*. *Protein Science*, 2016. **25**(1): p. 147-58.
158. Kollman, P.A., et al., *Calculating structures and free energies of complex molecules: combining molecular mechanics and continuum models*. *Accounts of Chemical Research*, 2000. **33**(12): p. 889-97.
159. Sitkoff, D., K.A. Sharp, and B. Honig, *Accurate Calculation of Hydration Free Energies Using Macroscopic Solvent Models*. *The Journal of Physical Chemistry*, 1994. **98**(7): p. 1978-1988.
160. Xu, B., et al., *Antiviral activity of (+)-rutamarin against Kaposi's sarcoma-associated herpesvirus by inhibition of the catalytic activity of human topoisomerase II*. *Antimicrob Agents Chemother*, 2014. **58**(1): p. 563-73.
161. Rastelli, G., et al., *Fast and accurate predictions of binding free energies using MM-PBSA and MM-GBSA*. *Journal of Computational Chemistry*, 2010. **31**(4): p. 797-810.
162. Lyne, P.D., M.L. Lamb, and J.C. Saeh, *Accurate prediction of the relative potencies of members of a series of kinase inhibitors using molecular docking and MM-GBSA scoring*. *Journal of Medicinal Chemistry*, 2006. **49**(16): p. 4805-8.
163. Guimaraes, C.R. and M. Cardozo, *MM-GB/SA rescoring of docking poses in structure-based lead optimization*. *Journal of Chemical Information and Modeling*, 2008. **48**(5): p. 958-70.
164. Incerti, M., et al., *Amino Acid Conjugates of Lithocholic Acid As Antagonists of the EphA2 Receptor*. *Journal of Medicinal Chemistry*, 2013. **56**(7): p. 2936-2947.
165. Baviskar, A.T., et al., *N-Fused Imidazoles As Novel Anticancer Agents That Inhibit Catalytic Activity of Topoisomerase II α and Induce Apoptosis in G1/S Phase*. *Journal of Medicinal Chemistry*, 2011. **54**(14): p. 5013-5030.
166. Humphrey, W., A. Dalke, and K. Schulten, *VMD: Visual molecular dynamics*. *Journal of Molecular Graphics*, 1996. **14**(1): p. 33-38.
167. David, C.C. and D.J. Jacobs, *Principal component analysis: a method for*

- determining the essential dynamics of proteins*. Methods in Molecular Biology, 2014. **1084**: p. 193-226.
168. Nagai, H. and Y.H. Kim, *Cancer prevention from the perspective of global cancer burden patterns*. Journal of Thoracic Disease, 2017. **9**(3): p. 448-451.
169. Pardee, A.B., Y.Z. Li, and C.J. Li, *Cancer therapy with beta-lapachone*. Current Cancer Drug Targets, 2002. **2**(3): p. 227-42.
170. Hou, Y., et al., *Shikonin induces apoptosis in the human gastric cancer cells HGC-27 through mitochondria-mediated pathway*. Pharmacognosy magazine, 2015. **11**(42): p. 250-256.
171. Wang, D., et al., *Cytotoxic effects of mansonone E and F isolated from Ulmus pumila*. Biological and Pharmaceutical Bulletin, 2004. **27**(7): p. 1025-30.
172. Liu, Z., et al., *Inhibition of thioredoxin reductase by mansonone F analogues: Implications for anticancer activity*. Chemico-Biological Interactions, 2009. **177**(1): p. 48-57.
173. Johnson, J., I. Gandhidasan, and R. Murugesan, *Cytotoxicity and superoxide anion generation by some naturally occurring quinones*. Free Radical Biology and Medicine, 1999. **26**(9): p. 1072-1078.
174. Wu, W.-B., et al., *Synthesis and evaluation of mansonone F derivatives as topoisomerase inhibitors*. European Journal of Medicinal Chemistry, 2011. **46**(8): p. 3339-3347.
175. Tanaka, N., M. Yasue, and H. Imamura, *The quinonoid pigments of mansonia altissima wood*. Tetrahedron Letters, 1966. **7**(24): p. 2767-2773.
176. Szejtli, J., *Introduction and General Overview of Cyclodextrin Chemistry*. Chemical Reviews, 1998. **98**(5): p. 1743-1754.
177. Carvalho, L.B.d., et al., *Complexes between methyltestosterone and β -cyclodextrin for application in aquaculture production*. Carbohydrate Polymers, 2018. **179**: p. 386-393.
178. Tommasini, S., et al., *Improvement in solubility and dissolution rate of flavonoids by complexation with β -cyclodextrin*. Journal of Pharmaceutical and Biomedical

- Analysis, 2004. **35**(2): p. 379-387.
179. Veiga, M.D., P.J. Díaz, and F. Ahsan, *Interactions of griseofulvin with cyclodextrins in solid binary systems*. Journal of Pharmaceutical Sciences, 1998. **87**(7): p. 891-900.
180. Vaidya, B., et al., *Nintedanib-cyclodextrin complex to improve bio-activity and intestinal permeability*. Carbohydrate Polymers, 2019. **204**: p. 68-77.
181. Loftsson, T. and M. Masson, *Cyclodextrins in topical drug formulations: theory and practice*. International Journal of Pharmaceutics, 2001. **225**(1-2): p. 15-30.
182. de Araujo, D.R., et al., *Development and pharmacological evaluation of ropivacaine-2-hydroxypropyl-beta-cyclodextrin inclusion complex*. European Journal of Pharmaceutical Sciences, 2008. **33**(1): p. 60-71.
183. Kai-Hang, L., et al., *[Preparation, characterization and antitumor of cyclodextrin inclusion of an anti-cancer drug regorafenib]*. Zhejiang Da Xue Xue Bao Yi Xue Ban, 2017. **46**(2): p. 151-159.
184. Kikuchi, M. and K. Uekama, *Effect of Dimethyl β -Cyclodextrin on Oral or Rectal Absorption of 1-Hexylcarbamoyl-5-fluorouracil (HCFU)*. YAKUGAKU ZASSHI, 1988. **108**(2): p. 156-163.
185. Kicuntod, J., et al., *Theoretical and Experimental Studies on Inclusion Complexes of Pinostrobin and beta-Cyclodextrins*. Scientia Pharmaceutica, 2018. **86**(1).
186. Frisch, M.J., et al., *Gaussian 09, Revision B.01*. 2009: Wallingford CT.
187. Hanpaibool, C., et al., *Theoretical analysis of orientations and tautomerization of genistein in β -cyclodextrin*. Journal of Molecular Liquids, 2018. **265**: p. 16-23.
188. Kirschner, K.N., et al., *GLYCAM06: a generalizable biomolecular force field. Carbohydrates*. Journal of Computational Chemistry, 2008. **29**(4): p. 622-55.
189. Luty, B.A. and W.F. van Gunsteren, *Calculating Electrostatic Interactions Using the Particle-Particle Particle-Mesh Method with Nonperiodic Long-Range Interactions*. The Journal of Physical Chemistry, 1996. **100**(7): p. 2581-2587.
190. Higuchi, T., *A phase solubility technique*. Advances in Analytical Chemistry and Instrumentation, 1965. **4**: p. 117-211.

191. Yang, L.J., et al., *Preparation and characterization of inclusion complexes of naringenin with beta-cyclodextrin or its derivative*. Carbohydrate Polymers, 2013. **98**(1): p. 861-9.
192. Kicuntod, J., et al., *Inclusion complexation of pinostrobin with various cyclodextrin derivatives*. Journal of Molecular Graphics and Modelling, 2016. **63**: p. 91-98.
193. Wongpituk, P., et al., *Structural dynamics and binding free energy of neral-cyclodextrins inclusion complexes: molecular dynamics simulation*. Molecular Simulation, 2017. **43**(13-16): p. 1356-1363.
194. Ren, B., et al., *In Silico understanding of the cyclodextrin-phenanthrene hybrid assemblies in both aqueous medium and bacterial membranes*. Journal of Hazardous Materials, 2015. **285**: p. 148-156.
195. Mongan, J., et al., *Generalized Born model with a simple, robust molecular volume correction*. Journal of Chemical Theory and Computation, 2007. **3**(1): p. 156-169.
196. Chen, W., C.-E. Chang, and M.K. Gilson, *Calculation of Cyclodextrin Binding Affinities: Energy, Entropy, and Implications for Drug Design*. Biophysical Journal, 2004. **87**(5): p. 3035-3049.
197. Fermeglia, M., et al., *Host-guest inclusion complexes between anticancer drugs and β -cyclodextrin: computational studies*. Carbohydrate Polymers, 2003. **53**(1): p. 15-44.
198. Liu, L. and Q.-X. Guo, *The Driving Forces in the Inclusion Complexation of Cyclodextrins*. Journal of Inclusion Phenomena and Macrocyclic Chemistry, 2002. **42**(1): p. 1-14.
199. Jullian, C., et al., *Spectroscopic characterization of the inclusion complexes of luteolin with native and derivatized β -cyclodextrin*. Bioorganic & Medicinal Chemistry, 2010. **18**(14): p. 5025-5031.
200. Wang, D.W., et al., *Inclusion of quinesrol and 2,6-di-O-methyl-beta-cyclodextrin: Preparation, characterization, and inclusion mode*. Carbohydrate Polymers, 2013. **93**(2): p. 753-60.

201. Jullian, C., et al., *Characterization, phase-solubility, and molecular modeling of inclusion complex of 5-nitroindazole derivative with cyclodextrins*. *Bioorganic & Medicinal Chemistry*, 2008. **16**(9): p. 5078-84.
202. Tang, P., et al., *Characterization and In Vitro Evaluation of the Complexes of Posaconazole with β - and 2,6-di-O-methyl- β -cyclodextrin*. *AAPS PharmSciTech*, 2017. **18**(1): p. 104-114.
203. Wang, L., et al., *Characterization and evaluation of synthetic riluzole with β -cyclodextrin and 2,6-di-O-methyl- β -cyclodextrin inclusion complexes*. *Carbohydrate Polymers*, 2015. **129**: p. 9-16.
204. Saleh, S.I., et al., *Effect of dimethyl-beta-cyclodextrin on nitrazepam stability*. *Journal de pharmacie de Belgique*, 1993. **48**(5): p. 383-8.
205. Sangpheak, W., et al., *Physical properties and biological activities of hesperetin and naringenin in complex with methylated beta-cyclodextrin*. *Beilstein Journal of Organic Chemistry*, 2015. **11**: p. 2763-73.
206. Hădărugă, N.G., et al., *Thermal stability of the linoleic acid/ α - and β -cyclodextrin complexes*. *Food Chemistry*, 2006. **99**(3): p. 500-508.
207. Abarca, R.L., et al., *Characterization of beta-cyclodextrin inclusion complexes containing an essential oil component*. *Food Chemistry*, 2016. **196**: p. 968-975.
208. Rajendiran, N. and S. Siva, *Inclusion complex of sulfadimethoxine with cyclodextrins: preparation and characterization*. *Carbohydrate Polymers*, 2014. **101**: p. 828-36.
209. Ventura, C.A., et al., *Preparation of celecoxib-dimethyl-beta-cyclodextrin inclusion complex: characterization and in vitro permeation study*. *European Journal of Medicinal Chemistry*, 2005. **40**(7): p. 624-31.
210. Rakmai, J., et al., *Antioxidant and antimicrobial properties of encapsulated guava leaf oil in hydroxypropyl-beta-cyclodextrin*. *Industrial Crops and Products*, 2018. **111**: p. 219-225.
211. Zarif, M.S., et al., *Physicochemical characterization of vancomycin and its complexes with β -cyclodextrin*. *Biomedical Research (India)*, 2012. **23**(4): p. 513-

- 520.
212. Yallapu, M.M., M. Jaggi, and S.C. Chauhan, *β -Cyclodextrin-curcumin self-assembly enhances curcumin delivery in prostate cancer cells*. Colloids and Surfaces B: Biointerfaces, 2010. **79**(1): p. 113-125.
213. Wang, F., et al., *Host-guest inclusion system of scutellarein with 2-hydroxypropyl-beta-cyclodextrin: preparation, characterization, and anticancer activity*. Journal of Biomaterials Science-Polymer Edition, 2014. **25**(6): p. 594-607.
214. Loftsson, T., *Drug permeation through biomembranes: cyclodextrins and the unstirred water layer*. Pharmazie, 2012. **67**(5): p. 363-70.
215. O'Brien, P.J., *Molecular mechanisms of quinone cytotoxicity*. Chemico-Biological Interactions, 1991. **80**(1): p. 1-41.
216. Rahmoun, N.M., et al., *Antimicrobial Activities of the Henna Extract and Some Synthetic Naphthoquinones Derivatives*. American Journal of Medical and Biological Research, 2013. **1**(1): p. 16-22.
217. Lu, J.J., et al., *Quinones derived from plant secondary metabolites as anti-cancer agents*. Anti-Cancer Agents in Medicinal Chemistry, 2013. **13**(3): p. 456-63.
218. Simoben, C.V., et al., *Exploring Cancer Therapeutics with Natural Products from African Medicinal Plants, Part I: Xanthones, Quinones, Steroids, Coumarins, Phenolics and other Classes of Compounds*. Anti-Cancer Agents in Medicinal Chemistry, 2015. **15**(9): p. 1092-111.
219. Tiew, P., et al., *Antifungal, antioxidant and larvicidal activities of compounds isolated from the heartwood of *Mansonia gagei**. Phytotherapy Research, 2003. **17**(2): p. 190-193.
220. Boonsri, S., et al., *Cytotoxic and antibacterial sesquiterpenes from *thespesia populnea**. Journal of Natural Products, 2008. **71**(7): p. 1173-1177.
221. Wang, D., et al., *Cytotoxic effects of mansonone E and F isolated from *Ulmus pumila**. Biological and Pharmaceutical Bulletin, 2004. **27**(7): p. 1025-1030.
222. Lee, K.H., C.H. Cho, and W.H. Yoon, *In vivo antitumor activity of mansonone E isolated from *Ulmus davidiana* var. *japonica* NAKAI*. Korean Journal of

- Pharmacognosy, 2004. **35**(3): p. 199-202.
223. Changwong, N., et al., *Acetyl- and Butyryl-cholinesterase Inhibitory Activities of Mansorins and Mansonones*. *Phytotherapy Research*, 2012. **26**(3): p. 392-396.
224. Huang, Z.H., et al., *Design, synthesis and biological evaluation of novel mansonone e derivatives prepared via CuAAC click chemistry as topoisomerase II inhibitors*. *European Journal of Medicinal Chemistry*, 2013. **68**: p. 58-71.
225. Paulino, M., et al., *Studies of trypanocidal (inhibitory) power of naphthoquinones: Evaluation of quantum chemical molecular descriptors for structure–activity relationships*. *European Journal of Medicinal Chemistry*, 2008. **43**(10): p. 2238-2246.
226. Villamil, S.F., et al., *Effects of mansonones on lipid peroxidation, P450 monooxygenase activity, and superoxide anion generation by rat liver microsomes*. *Biochemical Pharmacology*, 1990. **40**(10): p. 2343-2351.
227. Castro, F.A.V., et al., *Cytotoxicity Mechanism of Two Naphthoquinones (Menadione and Plumbagin) in Saccharomyces cerevisiae*. *PLoS ONE*, 2008. **3**(12): p. e3999.
228. Maier, N.M., P. Franco, and W. Lindner, *Separation of enantiomers: needs, challenges, perspectives*. *Journal of Chromatography A*, 2001. **906**(1-2): p. 3-33.
229. Kicuntod, J., et al., *Inclusion complexation of pinostrobin with various cyclodextrin derivatives*. *Journal of Molecular Graphics and Modelling*, 2016. **63**: p. 91-8.
230. Yuan, C., B. Liu, and H. Liu, *Characterization of hydroxypropyl- β -cyclodextrins with different substitution patterns via FTIR, GC-MS, and TG-DTA*. *Carbohydrate Polymers*, 2015. **118**: p. 36-40.
231. Wongpituk, P., et al., *Structural dynamics and binding free energy of neral-cyclodextrins inclusion complexes: molecular dynamics simulation*. *Molecular Simulation*, 2017: p. 1-8.
232. Walker, R.C., M.F. Crowley, and D.A. Case, *The implementation of a fast and accurate QM/MM potential method in Amber*. *Journal of Computational Chemistry*, 2008. **29**(7): p. 1019-31.

233. Kaiyawet, N., T. Rungrotmongkol, and S. Hannongbua, *Effect of halogen substitutions on dUMP to stability of thymidylate synthase/dUMP/mTHF ternary complex using molecular dynamics simulation*. Journal of Chemical Information and Modeling, 2013. **53**(6): p. 1315-23.
234. Khuntawee, W., T. Rungrotmongkol, and S. Hannongbua, *Molecular dynamic behavior and binding affinity of flavonoid analogues to the cyclin dependent kinase 6/cyclin D complex*. Journal of Chemical Information and Modeling, 2012. **52**(1): p. 76-83.
235. Meeprasert, A., et al., *In silico screening for potent inhibitors against the NS3/4A protease of hepatitis C virus*. Current Pharmaceutical Design, 2014. **20**(21): p. 3465-77.
236. Khuntawee, W., et al., *Comparison of Implicit and Explicit Solvation Models for Iota-Cyclodextrin Conformation Analysis from Replica Exchange Molecular Dynamics*. Journal of Chemical Information and Modeling, 2017. **57**(4): p. 778-786.
237. Khuntawee, W., et al., *Conformation study of varepsilon-cyclodextrin: Replica exchange molecular dynamics simulations*. Carbohydrate Polymers, 2016. **141**: p. 99-105.
238. Nutho, B., et al., *Binding mode and free energy prediction of fisetin/beta-cyclodextrin inclusion complexes*. Beilstein Journal of Organic Chemistry, 2014. **10**: p. 2789-99.
239. Tang, P., et al., *Inclusion complexes of chlorzoxazone with beta- and hydroxypropyl-beta-cyclodextrin: Characterization, dissolution, and cytotoxicity*. Carbohydrate Polymers, 2015. **131**: p. 297-305.
240. Fu, Q., et al., *Enhancement of enantioselectivity in chiral capillary electrophoresis using hydroxypropyl-beta-cyclodextrin as chiral selector under molecular crowding conditions induced by dextran or dextrin*. Electrophoresis, 2014. **35**(20): p. 2938-45.
241. Rekharsky, M. and Y. Inoue, *Chiral Recognition Thermodynamics of β -Cyclodextrin: The Thermodynamic Origin of Enantioselectivity and the Enthalpy-*

- Entropy Compensation Effect*. Journal of the American Chemical Society, 2000. 122(18): p. 4418-4435.
242. Kanagaraj, K., P. Suresh, and K. Pitchumani, *Per-6-amino- β -cyclodextrin as a Reusable Promoter and Chiral Host for Enantioselective Henry Reaction*. Organic Letters, 2010. 12(18): p. 4070-4073.



APPENDIX

Supplementary information

CHAPTER II

Butoxy mansonone G inhibits STAT3 and Akt signaling pathways in non-small cell lung cancers: Combined experimental and theoretical investigations

Panupong Mahalapbutr^a, Piyanuch Wonganan^{b,*}, Warinthorn Chavasiri^c and Thanyada Rungrotmongkol^{a,d,*}

This article has been published in *Cancers* (2019)

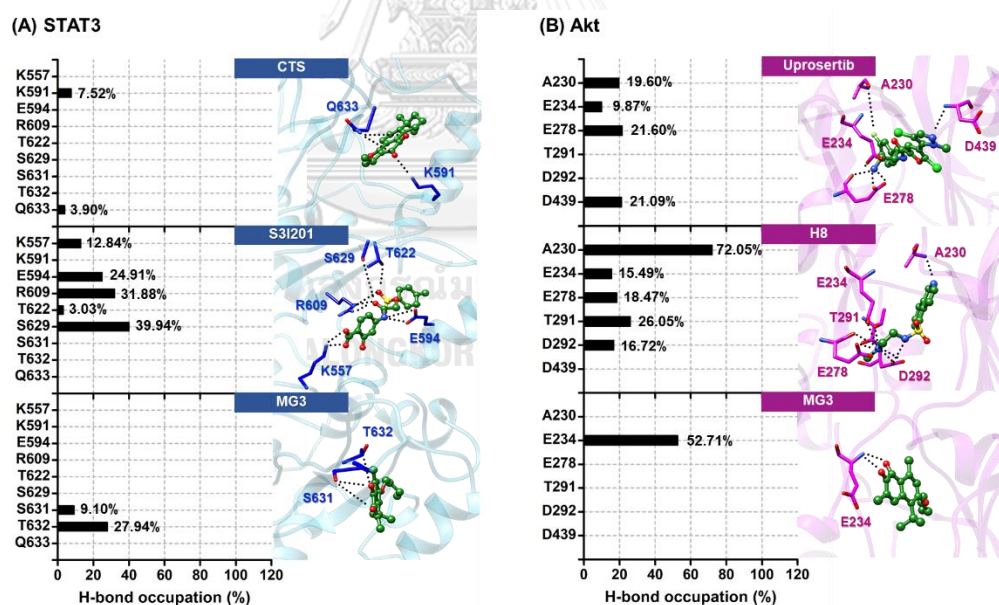


Figure S1 The percentage of H-bond occupation of the amino acid residues contributing to all ligands during the last 200-ns simulations within (A) SH2 domain of STAT3 and (B) ATP-binding pocket of Akt. Dotted lines depict the H-bond formation.

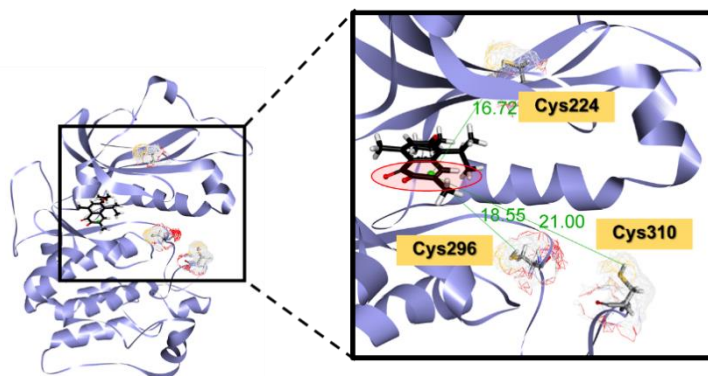


Figure S2 The binding orientation of MG3 against Akt signaling protein taken from the last snapshot of 500-ns MD simulation. The α,β -unsaturated carbonyl (α,β -UC) unit of MG3 is shown in red circle, where its center of mass (C_m) is represented in green ball. The obtained results revealed that α,β -UC part of MG3 positioned far away (>15 Å) from the cysteine residues in Akt's active site, suggesting that MG3 could not form the covalent adduct with Akt.

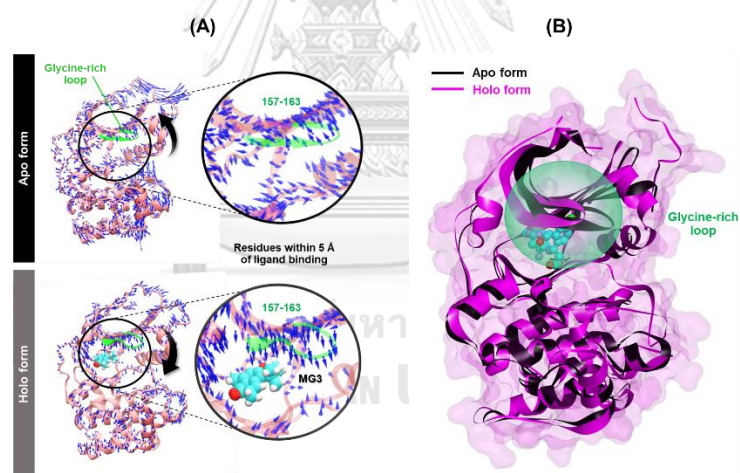


Figure S3 (A) The PCA result of Akt1 model. (B) the superimposed crystal structures between apo (PDB ID: 1GZN, black) and holo forms (PDB ID: 4GV1, pink) of Akt. Note that, due to the lack of crystal structure of Akt1 apo form in PDB data bank; thus, the apo form of Akt2 was chosen as a representative model. Our calculations agreed well with the crystal structures showing that the ligand binding induced glycine-rich loop to become significantly locate closer to stabilize ligand.

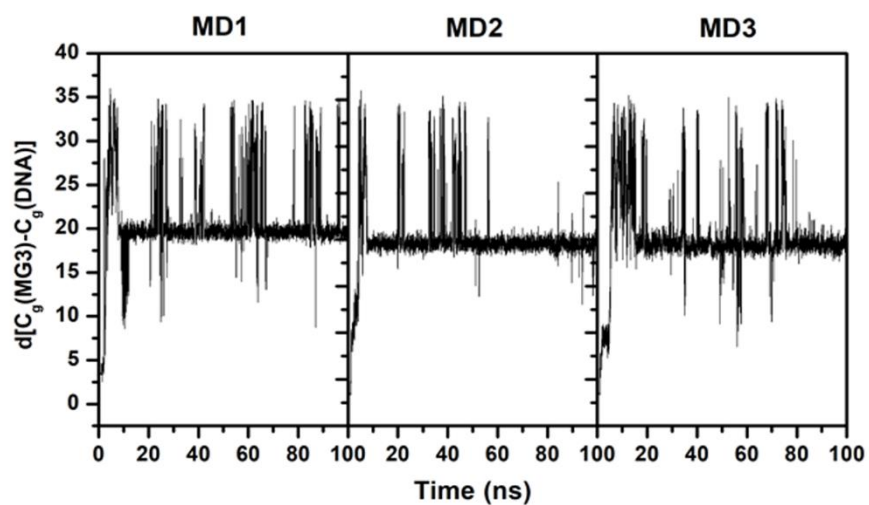
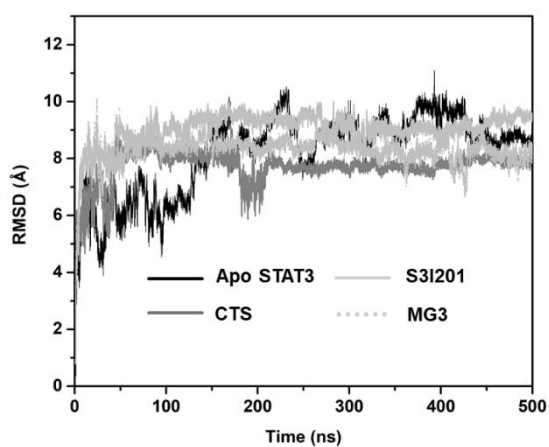


Figure S4 The distance between the C_m of MG3 and DNA ($d(C_m(\text{MG3})-C_m(\text{DNA}))$) of three independent simulations (MD1-3).

A) STAT3



B) Akt

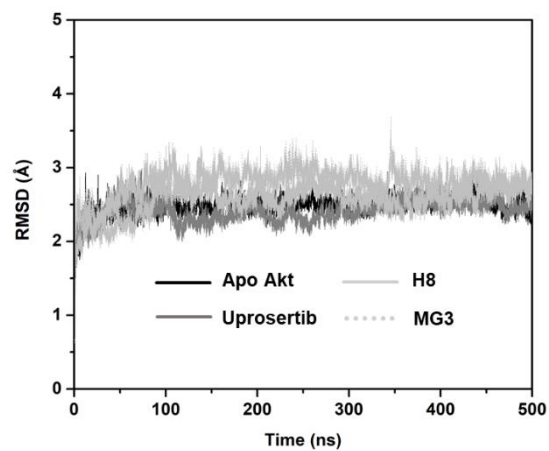


Figure S5 RMSD plots of (A) STAT3 and (B) Akt models.



Figure S6 Morphology of PCS201-010 cells after treatment with MG3 and CDDP for 24 h. It can be clearly seen that MG3 and CDDP induced cellular shrinking, a predominant characteristic of programmed cell death, indicating that MG3 and CDDP promoted cell death through apoptosis-inducing effect.

Table S1. The computational details of all initial structures used for MD simulations.

System	PDB ID of protein	Method for generating protein-ligand complex	Net charge of ligand	Amount of added water molecules
CTS/STAT3	1BG1	CDOCKER	0	19457
S31201/STAT3	1BG1	CDOCKER	-1	19339
MG3/STAT3	1BG1	CDOCKER	0	19398
Uprosertib/Akt	4GV1	CDOCKER	+1	12274
H8/Akt	4GV1	CDOCKER	+1	12276
MG3/Akt	4GV1	CDOCKER	0	12265
STAT3 (Apo form)	1BG1	-	-	19410
Akt (Apo form)	4GV1	-	-	12282
MG3/DNA	2NPW	CDOCKER	0	5657

CHAPTER III

Molecular Recognition of Naphthoquinone-containing Compounds against Human DNA

Topoisomerase II α ATPase domain: A Molecular Modeling Study

Panupong Mahalapbutr^a, Phakawat Chusuth^a, Nawe Kungwan^{b,c}, Warinthorn Chavasiri^d, Peter Wolschann^{a,e,f}, and Thanyada Rungrotmongkol^{a,g*}

This article has been published in Journal of Molecular Liquids (2017)

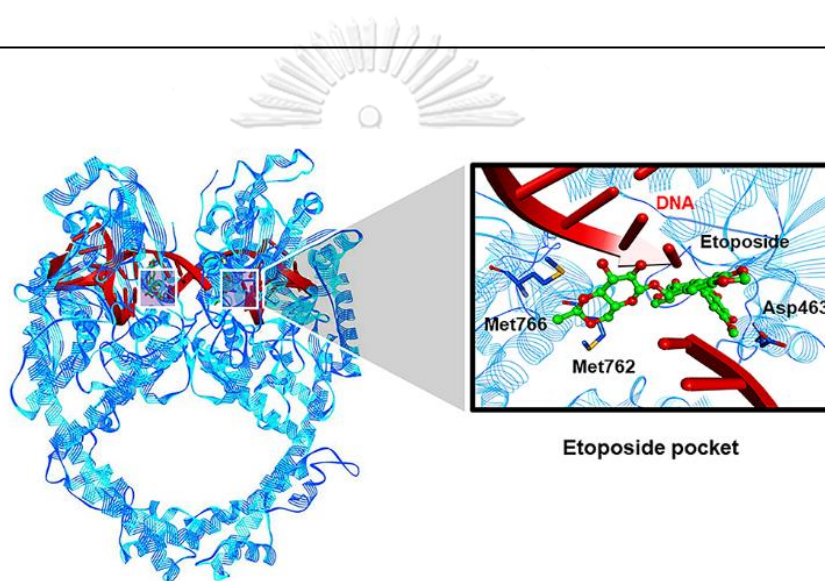


Figure S1 Superimposition of Topo II α homology model (dark blue) and etoposide-Topo II β crystal structure (light blue, PDB code: 3QX3). The amino acids of Topo II α homology model involved in the etoposide binding are indicated as dark blue sticks (Asp463, Met762, and Met766) [122].

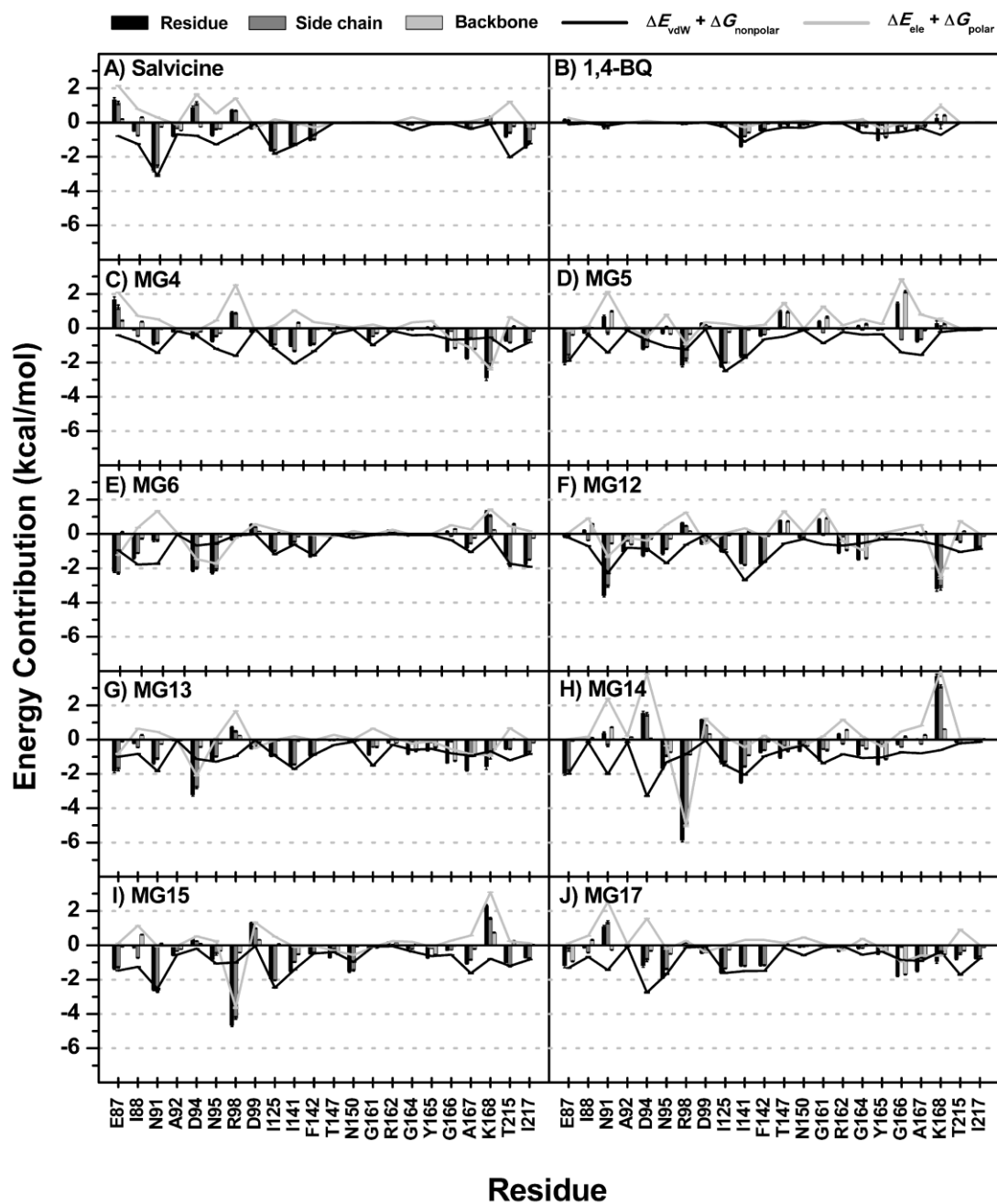


Figure S2 Energy contributions from the residue (black bar), side chain (grey bar), and backbone (light grey bar) of all protein-ligand complexes. The electrostatic ($\Delta E_{ele} + \Delta G_{polar}$) and vdW ($\Delta E_{vdW} + \Delta G_{nonpolar}$) energy contributions from each residue are presented by light grey and black lines, respectively.

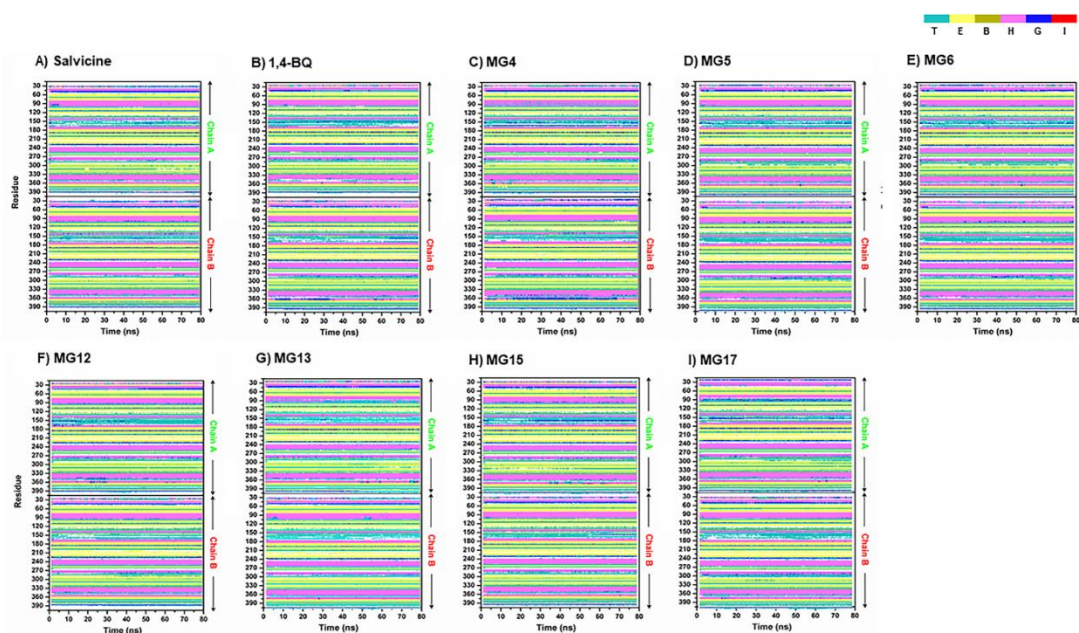


Figure S3 The timeline secondary structures of (A) salvicine, (B) 1,4-BQ, (C) MG4, (D) MG5, (E) MG6, (F) MG12, (G) MG13, (H) MG15, and (I) MG17. The color key for secondary structure plots was represented by six colors, in which turn, extended configuration, isolated bridge, alpha helix, 3-10 helix, and pi-helix are abbreviated by T, E, B, H, G, and I, respectively.

CHAPTER IV

Inclusion complexes of mansonone G with β -cyclodextrins: Molecular modeling, phase solubility, characterization, and cytotoxicity

Panupong Mahalapbutr^a, Piyanuch Wonganan^{b*}, Thanapon Charoenwongpaiboon^c,
Warinthorn Chavasiri^d, Manchumas Prousoontorn^c, Thanyada Rungrotmongkol^{a,e,f*}

This article is in preparation for publication (2019)

Table S1 Linear equation of MG/ β CDs inclusion complexes at different temperatures derived from Figure 2.

Temperature (°C)	Y= mX + c			r ²		
	MG/ β CD	MG/DM β CD	MG/HP β CD	MG/ β CD	MG/DM β CD	MG/HP β CD
30	Y=0.00403X+0.0072	Y=0.01797X+0.00815	Y=0.00629X+0.00925	0.996	0.993	0.993
37	Y=0.00409X+0.02491	Y=0.01639X+0.02591	Y=0.00651X+0.02677	0.995	0.995	0.999
45	Y=0.00497X+0.04590	Y=0.01888X+0.05374	Y=0.00875X+0.05099	0.997	0.988	0.981

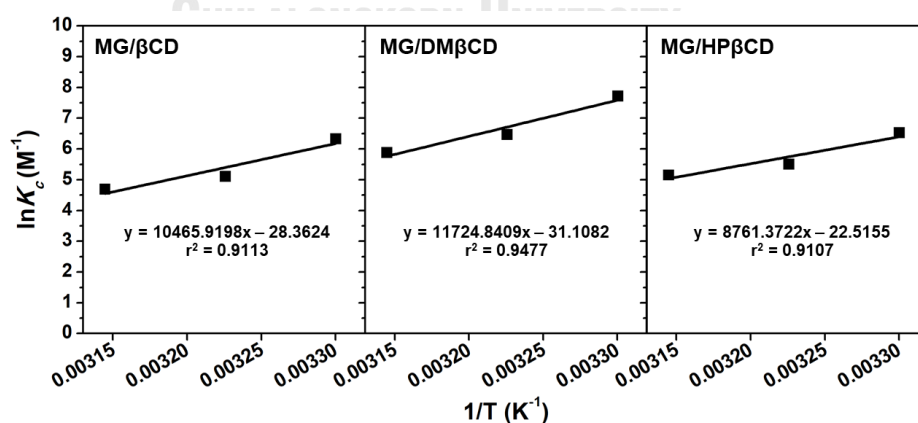


Figure S. Van't Hoff plots of MG/ β CDs inclusion complexes.

CHAPTER V

Molecular Insights into Inclusion Complexes of Mansonone E and H Enantiomers with various β -cyclodextrinsPanupong Mahalapbutr^a, Bodee Nutho^b, Peter Wolschann^{a,c,d}, Warinthorn Chavasiri^eNawee Kungwan^{f,g}, and Thanyada Rungrotmongkol^{a,h*}

This article has been published in Journal of Molecular Graphic and Modelling (2018)

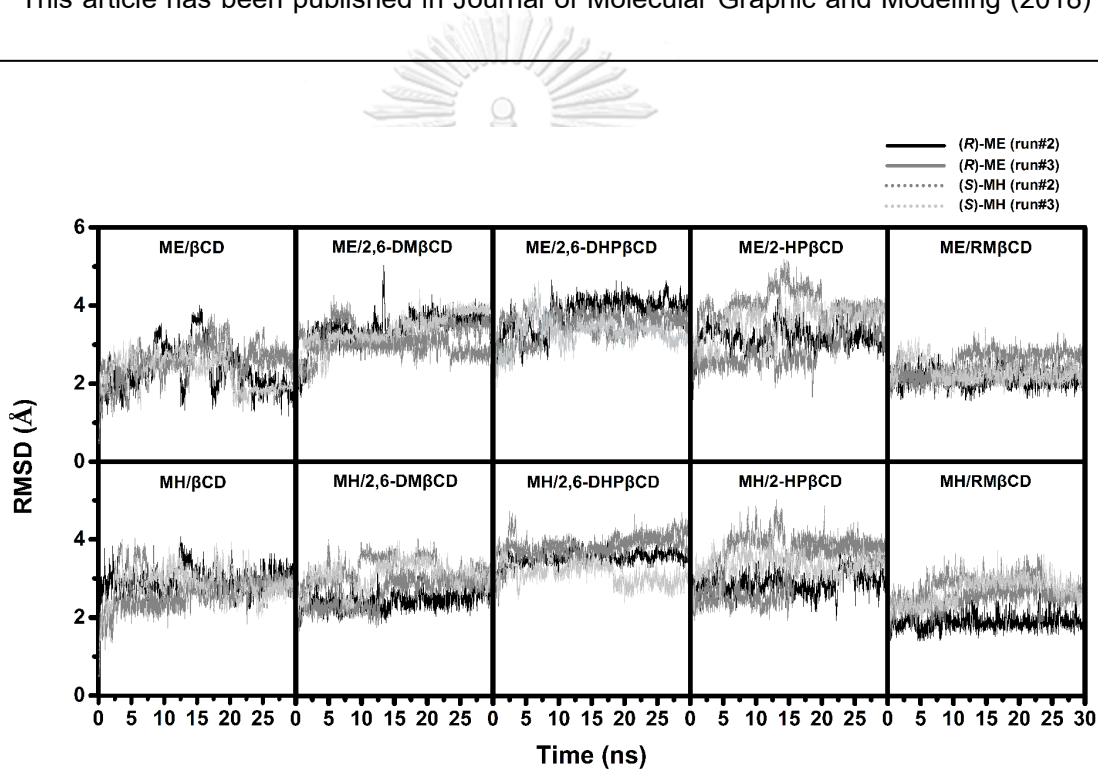


Figure S1 RMSD plots for all atoms of the two stereoisomers of ME and MH inclusion complexes.

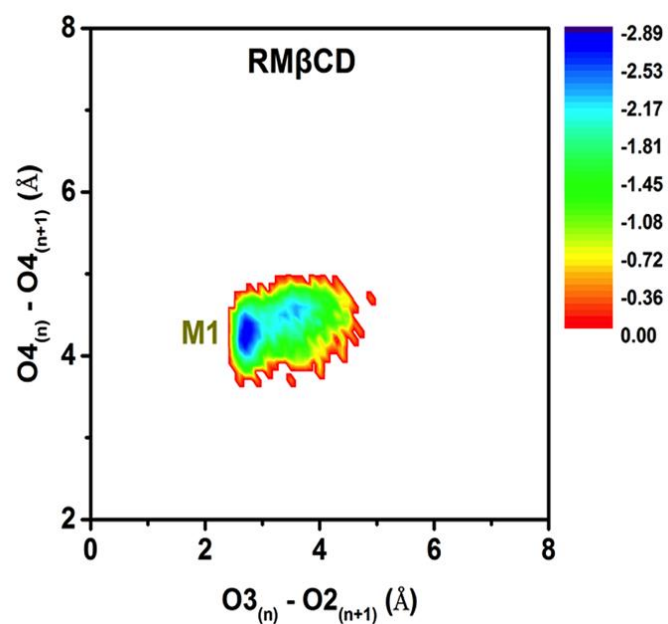


Figure S2 The potential energy surface (PES) of the free form of RMβCD.



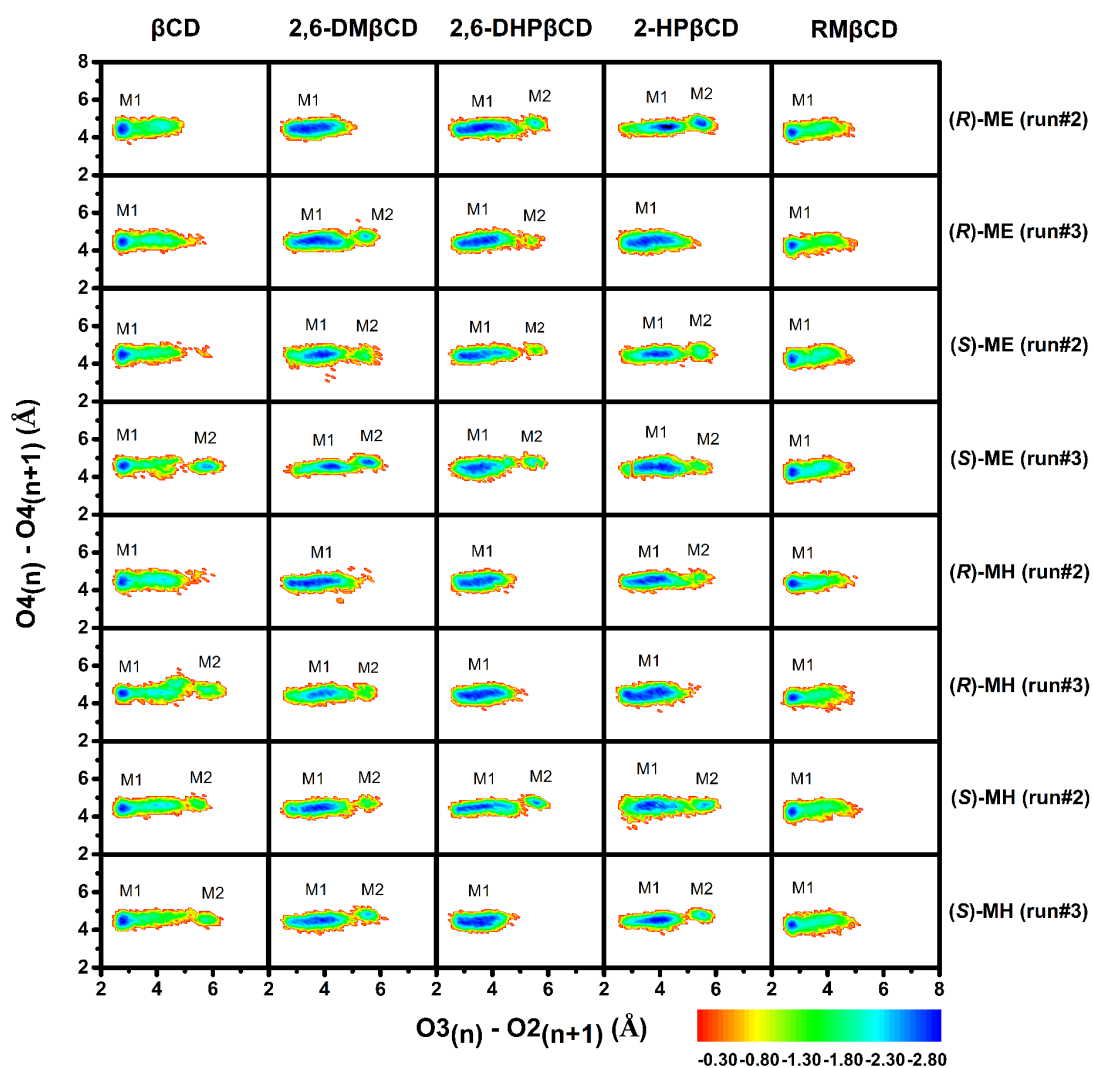


Figure S3 The potential energy surface (PES) of the distance between the adjacent glycosidic oxygens, $O4_{(n)} - O4_{(n+1)}$ and the distance of intramolecular H-bond, $O3_{(n)} - O2_{(n+1)}$.

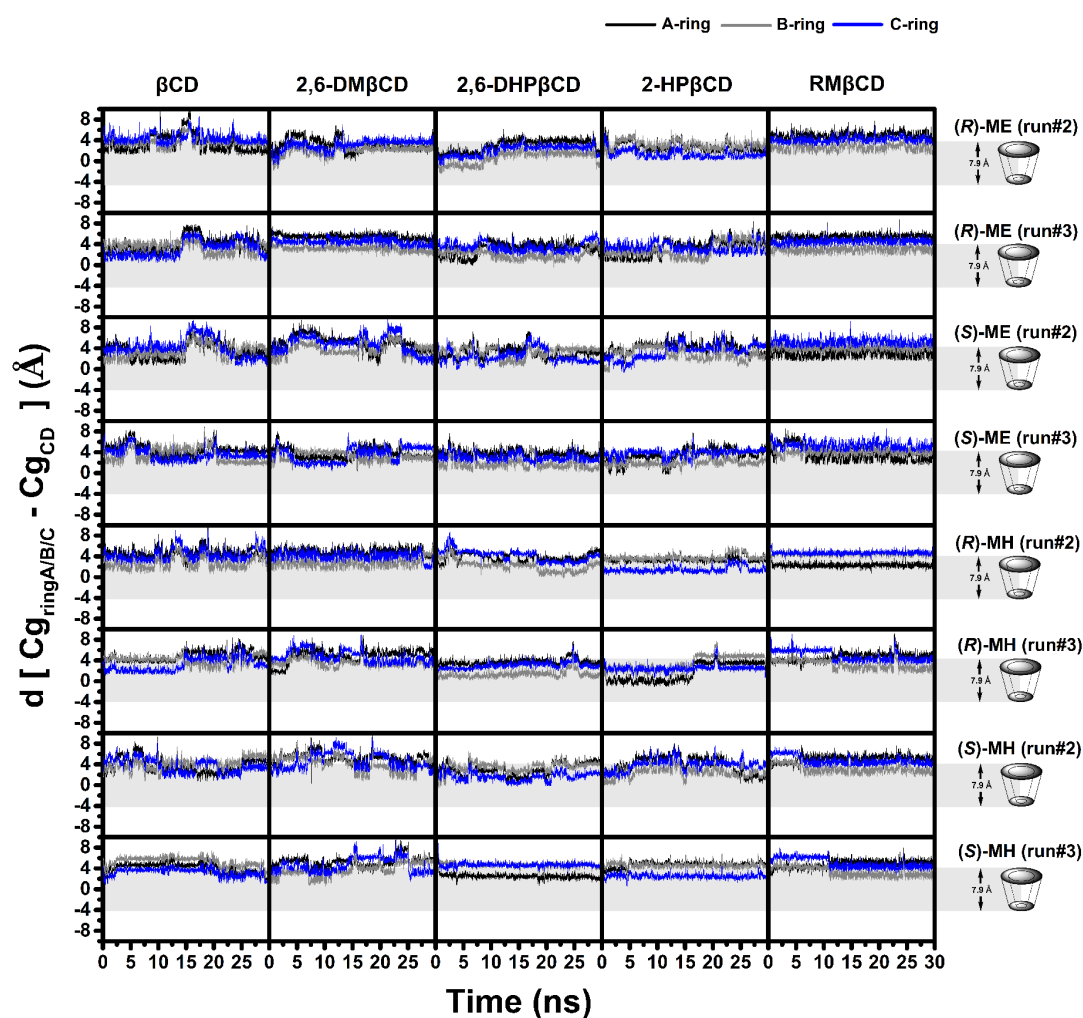


Figure S4 Distance between the center of gravity of each MSN(s) ring and CD(s). Light grey box represents the height of torus of β CD without the functional modification.

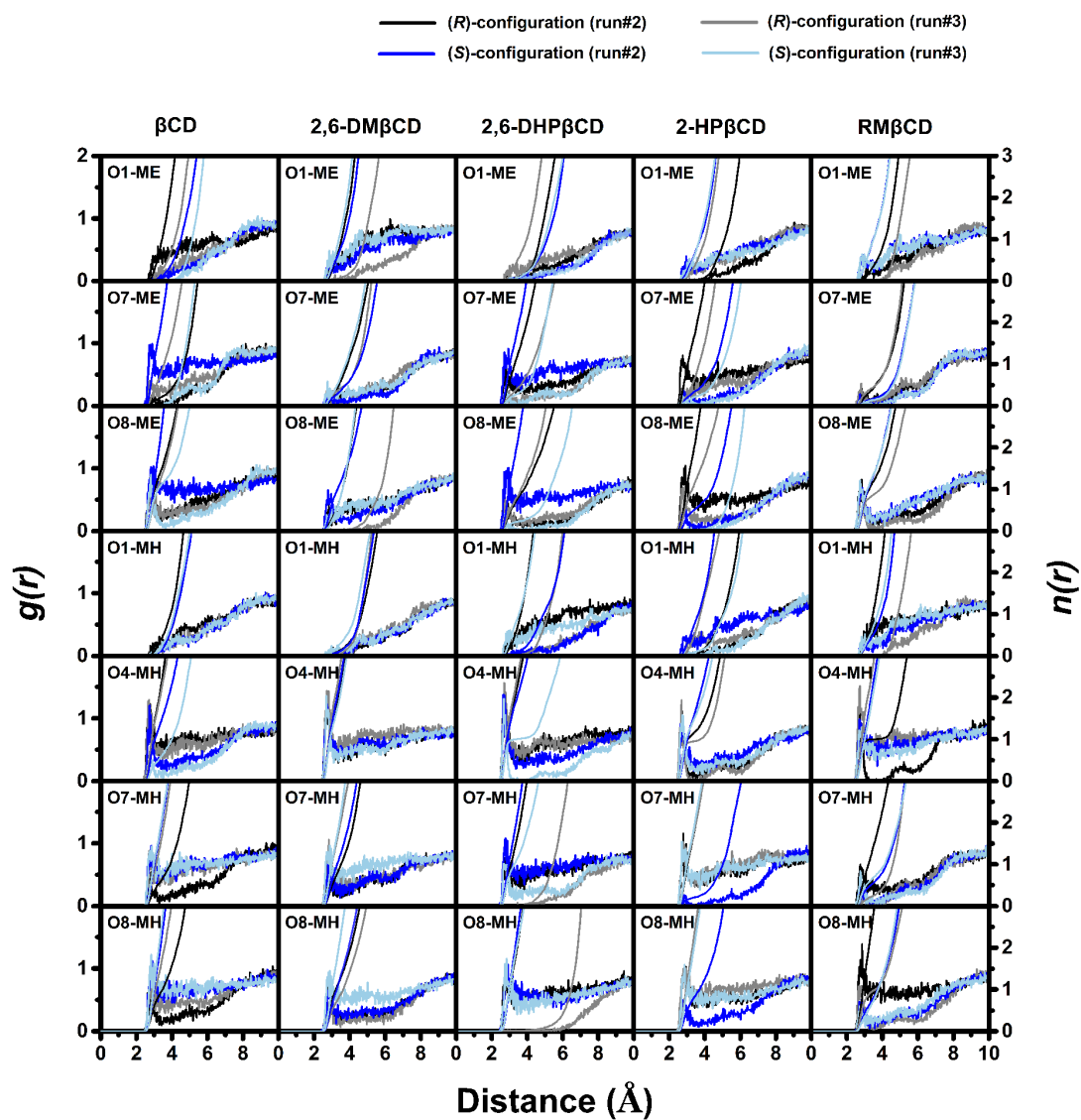


Figure S5 Radial distribution function (RDF) of water oxygen atoms around the heteroatoms of two MSNs.

VITA

NAME Panupong Mahalapbutr

DATE OF BIRTH 12 September 1991

INSTITUTIONS ATTENDED

2010-2014	B.Sc. in Chemistry (First Class Honors) Department of Chemistry, Faculty of Science, Srinakharinwirot University, Bangkok, Thailand
2014-2019	Ph.D. in Biochemistry and Molecular Biology Department of Biochemistry, Faculty of Science, Chulalongkorn University, Bangkok, Thailand

HOME ADDRESS 870/43 Happy Condo Ratchada18 Huikwang Samsennok Bangkok 10310

PUBLICATION

1. P. Mahalapbutr, P. Wonganan*, W. Chavasiri, N. Kungwan, T. Rungrotmongkol*, Butoxy mansonone G inhibits STAT3 and Akt signaling pathways in non-small cell lung cancers: Combined experimental and theoretical investigations, *Cancers*, 2019, 11, 437.
2. J. Kammarabutr, P. Mahalapbutr, B. Nutho, N. Kungwan, T. Rungrotmongkol, Low susceptibility of asunaprevir towards R155K and D168A point mutations in HCV NS3/4A protease: A molecular dynamics simulation, *Journal of Molecular Graphics and Modelling*, 2019, 89, 122-130.
3. P. Mahalapbutr, K. Thitinanthavet, T. kedkham, N. Huy, T. Le,S. Dokmaisrijan, L. Huynh, N. Kungwan, T. Rungrotmongkol*, A theoretical study on the molecular encapsulation of luteolin and pinocembrin with various derivatized beta-cyclodextrins, *Journal of Molecular Structure*, 2018, 1180, 480-490.
4. P. Mahalapbutr, B. Nutho, P. Wolschann, N. Kungwan, T. Rungrotmongkol*, Molecular Insights into Inclusion Complexes of Mansonone E and H Enantiomers with various β -cyclodextrins, *Journal of Molecular Graphics and Modeling*, 2018, 79, 72-80.
5. P. Mahalapbutr, P. Chusuth, N. Kungwan, W. Chavasiri, P. Wolschann, T. Rungrotmongkol*, Molecular Recognition of Naphthoquinone-containing Compounds against Human DNA Topoisomerase II α ATPase domain: A Molecular Modeling Study, *Journal of Molecular Liquids*, 2017, 247, 374-385.

AWARD RECEIVED Outstanding poster presentation award from the 2018 Chemistry Research Symposium, ChRS2018, Kasetsart University Kamphaeng Saen Campus, 2018